Title
Micropost Arrays to Advance Cell Handling

Author
Sochol, Ryan Daniel

Publication Date
2011

Peer reviewed|Thesis/dissertation

Micropost Arrays to Advance Cell Handling

By

Ryan Daniel Sochol

A thesis submitted in partial satisfaction of the

requirements for the degree of

Doctor of Philosophy

in

Mechanical Engineering

in the

Graduate Division

of the

University of California, Berkeley

Committee in charge:

Professor Liwei Lin, Chair

Professor Dorian Liepmann

Professor Song Li

Professor Luke P. Lee

Fall 2011

Abstract

Micropost Arrays to Advance Cell Handling

by

Ryan Daniel Sochol

Doctor of Philosophy in Mechanical Engineering

University of California, Berkeley

Professor Liwei Lin, Chair

Mechanical engineering methods and microfabrication techniques offer powerful means for meeting biological challenges. In particular, microfabrication processes enable researchers to develop technologies at scales that are biologically relevant and advantageous. In this work, microfabricated posts were employed to advance cell handling capabilities in both static and dynamic (*i.e.*, microfluidic) systems.

Static, substrate-based biophysical properties influence diverse cellular processes. Methods for engineering micropost arrays enable microscale control over the biophysical characteristics of discrete topographic features. Here, unidirectional micropost array gradients of variable micropost stiffness and variable interpost spacing were constructed to regulate cell motility using two distinct biophysical cues: (*i*) gradients in substrate rigidity (*i.e.*, *via* durotaxis – a subset of mechanotaxis), and (*ii*) variable spacing of substrate binding sites – *via* a phenomenon herein referred to as *spatiotaxis*. Micropost array stiffness gradients were designed with post-to-post differences in stiffness of 0.5 nN/μm, 2 nN/μm, 3 nN/μm, and 7.5 nN/μm. Bovine aortic endothelial cells (BAECs) seeded on micropost array gradients with variable micropost stiffness exhibited preferential cell migration in the direction of increasing micropost stiffness. Gradients of elliptical microposts further enhanced unidirectional guidance by limiting cellular movement perpendicular to the direction of increasing micropost stiffness. Micropost array spacing gradients were designed with average post-to-post differences in spacing of 10 nm, 20 nm, and 40 nm. Micropost array gradients with variable interpost spacing were found to promote BAEC migration in the direction of decreasing interpost spacing, which represents the first demonstration of unidirectional spatiotaxis. Higher gradient strengths were observed to enhance the aforementioned migratory behaviors for both biophysical cues. For substrates with simultaneous, anti-parallel stiffness and spatial stimuli, the spatial cues were found to dominate the migratory response. The micropost array gradient methodology offers a powerful technique for investigating the biophysical cellular response, while also providing the basis for new classes

of passive substrates capable of directing cell motility in biological fields, such as biomaterials, tissue engineering, and regenerative medicine.

In order to create high-speed lab-on-a-chip devices for quantitative cell biology, drug discovery, and molecular diagnostics, precision hydrodynamic controls of microparticles (*e.g.*, cells and microbeads) are in critical demand. The ability to achieve multi-stage fluidic reaction processes for microparticles is integral to diverse chemical and biological applications; however, microfluidic particulate-based systems remain limited due to particle handling issues. In contrast to suspended cells, which are experimentally complex, microbeads offer a simplified example for initial demonstrations of microfluidic particulate handling. Thus, the ability to manipulate microbeads in microfluidic systems represents a fundamental first step toward advancing microfluidic cell handling. In this dissertation, microposts ($15\times15\ \mu m^2$) were arrayed within microfluidic architectures ($18\ \mu m$ in height) to enhance microparticle handling and enable multi-stage fluidic reactions and analyses for suspended particles. The presented microfluidic systems were first characterized using suspended microbeads ($15\ \mu m$ in diameter); thereafter, the potential of employing the platforms for cell handling applications was also investigated using suspended BAECs. A resettable, hydrodynamic microparticle trapping system – termed micropost array trapping (μPAT) – was designed and demonstrated to accomplish controlled particulate arraying and microarray resettability by trapping-and-releasing both microbeads and cells. The μPAT technique was integrated into: (*i*) a dynamic microarray to detect multiple bio-molecules in parallel *via* molecular beacon probes conjugated to microbead substrates, and (*ii*) a "Microfluidic Ping Pong" (MPP) system to achieve multi-stage fluidic reactions under discontinuous flow conditions. As a demonstrative example, the MPP technique was employed to detect an inflammatory cytokine at 100 pM concentrations *via* an 11-stage aptamer beacon-based sandwich assay performed using microbeads. Additionally, a microfluidic micropost array railing (μPAR) system was developed to rapidly transport both microbeads and cells into adjacent flow streams under continuous flow conditions. To demonstrate the μPAR technique, a multiplexed layer-by-layer (LbL) molecular synthesis process (*i.e.*, consisting of up to 18 fluidic stages) was accomplished on microbead substrates. This work represents the first demonstration of a microfluidic platform capable of railing either microbeads or cells into adjacent flow streams. Through improved microparticle handling in microfluidic systems, the presented methodologies could further extend the efficacy of dynamic cell-based and bead-based microarrays for applications in diverse chemical and biological fields.

Dedication

This work is dedicated to my parents,

Lori and David Sochol,

whose uncompromising belief in me is the reason for my accomplishments.

Unconditional love is a powerful thing.
It instills a sense of self-worth, security, and optimism
that reframes life's challenges to appear far less daunting.

Acknowledgements

To say my experience at UC Berkeley has surpassed my expectations would be a considerable understatement. Coming to Berkeley without any prior research experience, in addition to not having taken courses in MEMS or Biology, was certainly a cause for anxiety when I began my graduate career. It did not help that I spent much of my first year of graduate school in a lab that was not a great fit, which only served to further exacerbate my concerns. Luckily, this trend reversed completely after I joined the Liwei Lin Lab. From that point on, my time at Berkeley has been characterized by tremendous growth not only intellectually, but in essentially every aspect of my life. It is without question that growth is primarily due to my interactions with the people who have been there for me during my graduate experience, all of whom I will try to acknowledge here.

First, I am truly grateful to my advisor, Prof. Liwei Lin, as well as my 'co-advisors,' Prof. Song Li and Prof. Luke Lee, for their incredible guidance and support during my graduate career. For those in the field, it is widely known how tremendous an opportunity it is to get to work with any one of these professors, but the fact that I've had access to such a brain trust of intellectual powerhouses throughout my time at Berkeley has been simply outstanding.

It should be noted that nothing here will really do justice to how extraordinary an advisor Prof. Liwei Lin has been; nonetheless, I will list some of my favorite aspects of working for him. On a purely academic level, I find it difficult to imagine that there are other professors in the world who work as hard as Prof. Lin does to cultivate creativity, independence, and intellectual growth in their students. This has been particularly true for me given that my biological research interests have never exactly been perfectly in line with the laboratory's research directions. Despite this fact, Prof. Lin has never wavered in his support of me. He has been a constant source of sound insight and feedback regarding every component of the academic process, with intellectual input that is consistently humbling. Additionally, I have genuinely never met anyone with more integrity than Prof. Lin. His commitment to honesty, fairness, and pragmatism is unsurpassed. I sincerely appreciate how fortunate I am to have had this experience.

As a mechanical engineer, the biological aspects of my projects have been particularly challenging. I cannot thank Prof. Song Li, Prof. Luke Lee, and Megan Dueck enough, not only for allowing me to work in their laboratories, but also for consistently providing me with invaluable help and advice throughout my graduate career. I recognize that Prof. Li, Prof. Lee, and Megan are quite busy with their own labs and research, so for them to have taken so much time over the years to meet with me, flesh out ideas, and edit manuscripts has meant a great deal. I especially want to express my gratitude for their encouragement of me as well as their continued support of my research projects.

I also want to thank Prof. Albert Pisano and Prof. Dorian Liepmann, whose counsel has been particularly helpful, especially during my time preparing for my qualifying examination.

I am truly thankful to Adrienne Higa, without whom it is doubtful that the micropost array gradient projects would have ever taken off. Her brilliance, insight, and work-ethic make her an

ideal research partner, but her understanding, thoughtfulness, and selflessness elevate her from just a partner to one of my very best friends.

I cannot imagine that graduate school would have been so enjoyable without such a wonderful environment for research. My mentor, Brian Sosnowchik, was critical in helping me develop my skills as a researcher. He certainly led by example, and was always willing to provide much-needed advice. I would like to thank Kosuke Iwai, Kedar Shah, Armon Mahajerin, Richard Winslow, and all of the members of the Liwei Lin Lab for their help and assistance. Working in outside laboratories can be difficult, but the laboratories of Prof. Song Li and Prof. Luke Lee as well as the Berkeley Nanotechnology Center (BNC) and the Berkeley Stem Cell Center have been incredibly welcoming and supportive. In particular, I greatly appreciate the help of Paul Lum, Mary West, Randall Janairo, Julia Chu, John Waldeisen, Hansang Cho, Terry Johnson, Jeffrey Henry, Timothy Downing, An-Chi Tsou, Kyle Kurpinski, Aijun Wang, and Erick Ulin-Avila. I also want to thank Joanne Lo for being there for me during my latter years, especially in terms of her help and input in the crucial hours right before abstract and manuscript deadlines.

Much of my work would not exist without the support and contributions of researchers who I have advised during my graduate career. I especially want to thank Barthélémy Lüthi, Benjamin Casavant, Eric Zhou, Liana Lo, Ryan Ruelos, Albert Lu, Valerie Chang, Dara Bahri, Jonathan Lei, Marc Russel, Chris Luong, Deepak Lingam, Anushweta Asthana, Sheng-Chih (Ken) Chang, Parminder Singh, Annie Chou, and Nina Khoshnevisrad.

Being a part of the Berkeley Sensor and Actuator Center (BSAC) has been fantastic, and a large part of that is due to my interactions with Helen Kim, John Huggins, Richard Lossing, Kim Ly, Yulia Golubovskaya, and Alain Kesseru. I also want to thank the mechanical engineering department's staff, including Donna Craig, Patricia Giddings, and Yawo Akpawu.

Outside of school, having family and friends that I can rely on has meant a lot to me. Having intellectual discussions and debates with my brother and sister, Jason and Jessica, has supported my ability to construct cogent arguments and think more critically. My uncle, Jeremy Sochol, always keeps me on my toes, especially with his 'sat question of the day' emails. It's always enjoyable receiving funny cards from my grandma, Sonia Feinberg, as well as discussing life during phone calls and visits. Spending downtime with my family has made work far less stressful, especially when Stacey, Mike, Blake, Lucie, and Payton join. It has really been amazing getting to be so close to my 'California cousins,' Sharon, Laura, Robert, Yo, Samantha, Zoe, Alex, and Cole, who have made living in the bay area such a great experience. I realize that graduate school is not supposed to be so much fun, but spending time with my friends has made these past few years some of the best of my life. Kevin Salimian, Daniel Peters, Chris Zeuger, Doron Klepach, George Mseis, Andrew Stevens, Deborah Sunter, Diana Lin, Maral Gharib, Kimberly Ann Krauze, Clare Gollnick, Grace Yoon, Ali Streimer, Jonathan Roth, Joshua Schmerling, Joanna Millman, Joshua Gerstenblith, Casey Spigel, Ann Evans, Anders Solem, Rocky Jones, Anthony Giangiorgi, and Daniel Alarcon – it's been a pleasure.

Lastly, I want to thank Eddie Murphy, Rick James, and Sharam for their renditions of P.A.T.T., which have provided me with much needed inspiration during multiple all-nighters in lab.

Table of Contents

Chapter 3: Arrayed Microposts for Microparticle Handling in Microfluidic Systems

Chapter 4: Conclusions

List of Figures

Chapter 1

Chapter 2

Chapter 3

List of Tables

Chapter 3

List of Acronyms

BAEC	Bovine Aortic Endothelial Cell
BHQ	Black Hole Quencher
BSA	Bovine Serum Albumin
C	Negative Control Substrate with Identical Interpost Spacing and Identical Circular Microposts for Spatiotaxis Experiments
C_C	Negative Control Substrate with Identical Circular Microposts for Dual-Axis Durotaxis Experiments
CCD	Charge-Coupled Device
C_E	Bidirectional Control Substrate with Identical Elliptical Microposts for Dual-Axis Durotaxis Experiments
DI	Deionized
DMEM	Dulbecco's Modified Eagle Medium
DNA	Deoxyribonucleic Acid
ECM	Extracellular Matrix
FA	Fluorescent Aptamer
FAM	Fluorescein
FBS	Fetal Bovine Serum
FRET	Förster Resonance Energy Transfer
HCV	Hepatitis C Virus
IFN-γ	Interferon-Gamma
k_{major}	Major Axes Linear Stiffness of Elliptical Microposts
k_{minor}	Minor Axes Linear Stiffness of Elliptical Microposts
LbL	Layer-by-Layer
LE	Loading Efficiency
MB	Molecular Beacon Probe
MM	Mismatch
MPP	Microfluidic Ping Pong
PBS	Phosphate-Buffered Saline
PDMS	Poly(dimethylsiloxane)
PM	Perfect Match

Q	Quencher
RE	Resetting Efficiency
RFI	Relative Fluorescent Intensity
RFR	Railing Failure Rate
S.E.M.	Standard Error of the Mean
SEM	Scanning Electron Microscope
SNP	Single Nucleotide Polymorphism (One Mismatch)
ssDNA	Single-Stranded Deoxyribonucleic Acid
TE	Trapping Efficiency
W_R	Resetting Width for Micropost Array Trapping
W_T	Trapping Width for Micropost Array Trapping
μDDG_H	Microtopographic Dual-Axis Durotaxis Gradient with High Gradient Strength
μDDG_L	Microtopographic Dual-Axis Durotaxis Gradient with Low Gradient Strength
μDG_H	Microtopographic Durotaxis Gradient with High Gradient Strength
μDG_L	Microtopographic Durotaxis Gradient with Low Gradient Strength
μDSG	Microtopographic Durotaxis *versus* Spatiotaxis Gradient
*μ*PAR	Micropost Array Railing
*μ*PAT	Micropost Array Trapping
μSG_H	Microtopographic Spatiotaxis Gradient with High Gradient Strength
μSG_L	Microtopographic Spatiotaxis Gradient with Low Gradient Strength
%ECM	Percentage of Extracellular Matrix Coverage

Chapter 1: Introduction

1.1 Dissertation Introduction

The advancement of cell handling capabilities in static and dynamic (*i.e.*, microfluidic) environments directly impacts fields including tissue engineering, biomaterials, regenerative medicine, quantitative cell biology, and medical diagnostics.[1-3] Ideally, techniques for cell handling under static conditions (*i.e.*, in the absence of external regulation or power) would enable high control of cell motility *via* simple, accurate, and repeatable fabrication processes. Unfortunately, simultaneously achieving these goals has remained a significant challenge.[4-11] Previously, a broad range of microenvironmental stimuli have been employed to regulate cellular behavior, including motility.[12-24] Passive, substrate-based biophysical stimuli could offer powerful means for cell handling *in vitro*; however, current methods suffer from drawbacks ranging from poor control of cell motility to limited fabrication processes.[4-11, 25-29] For cell handling in microfluidic systems (*e.g.*, dynamic microarrays), researchers have developed a variety of methods for: (*i*) immobilizing cells in designated array positions, (*ii*) mixing cells with multiple fluidic reagents, and (*iii*) releasing cells from microfluidic arrays.[30-43] The efficacy of techniques for trapping-and-releasing cells could be further extended by increasing trapping efficiencies and densities, simplifying processes associated with device fabrication and operation, and improving resetting efficiencies. Additionally, limitations associated with accomplishing multi-stage fluidic reactions in such systems have hindered the applicability of dynamic cell-based microarrays.

This dissertation reports efforts to develop new methodologies for advancing cell handling in both static and dynamic environments *via* the use of arrayed microposts. The technique of using micropost array gradients to apply biophysical stimuli to seeded cells is presented for enabling cell handling under static conditions (**Fig. 1.1a**). By altering the geometric characteristics of micropost arrays, such as micropost radii (**Fig. 1.1a –** *left*, '*r*') and interpost spacing (**Fig. 1.1a –** *left*, '*l*'), the biophysical properties of discrete, microscale substrate features can be tuned *via* simple, accurate, and repeatable fabrication processes. Micropost array gradients were designed, fabricated, and experimentally demonstrated to accomplish unidirectional cellular guidance using microtopographic mechanical (*i.e.*, durotaxis) and spatial (*i.e.*, spatiotaxis) stimuli. Experiments were performed with living cells seeded on several classes of micropost array gradients (**Fig. 1.1a –** *right*). The motility of bovine aortic endothelial cells (BAECs) was quantified by tracking the movement of single cells over the course of 18-hour time-lapse studies. The experimental results represent the first demonstration of unidirectional cellular durotaxis induced *via* microtopographic stiffness cues. Additionally, the ability to achieve unidirectional cellular guidance by varying the spacing of substrate binding sites (*i.e.*, spatiotaxis) has been demonstrated for the first time.

To advance cell handling in microfluidic systems, several microfluidic platforms integrating arrayed microposts are presented. Compared to microbeads, living cells are characterized by a significantly higher degree of complexity. Thus, successfully manipulating microbeads in microfluidic systems is a critical first step toward robust microfluidic cell handling. Consequently, this dissertation focuses primarily on the development of microfluidic

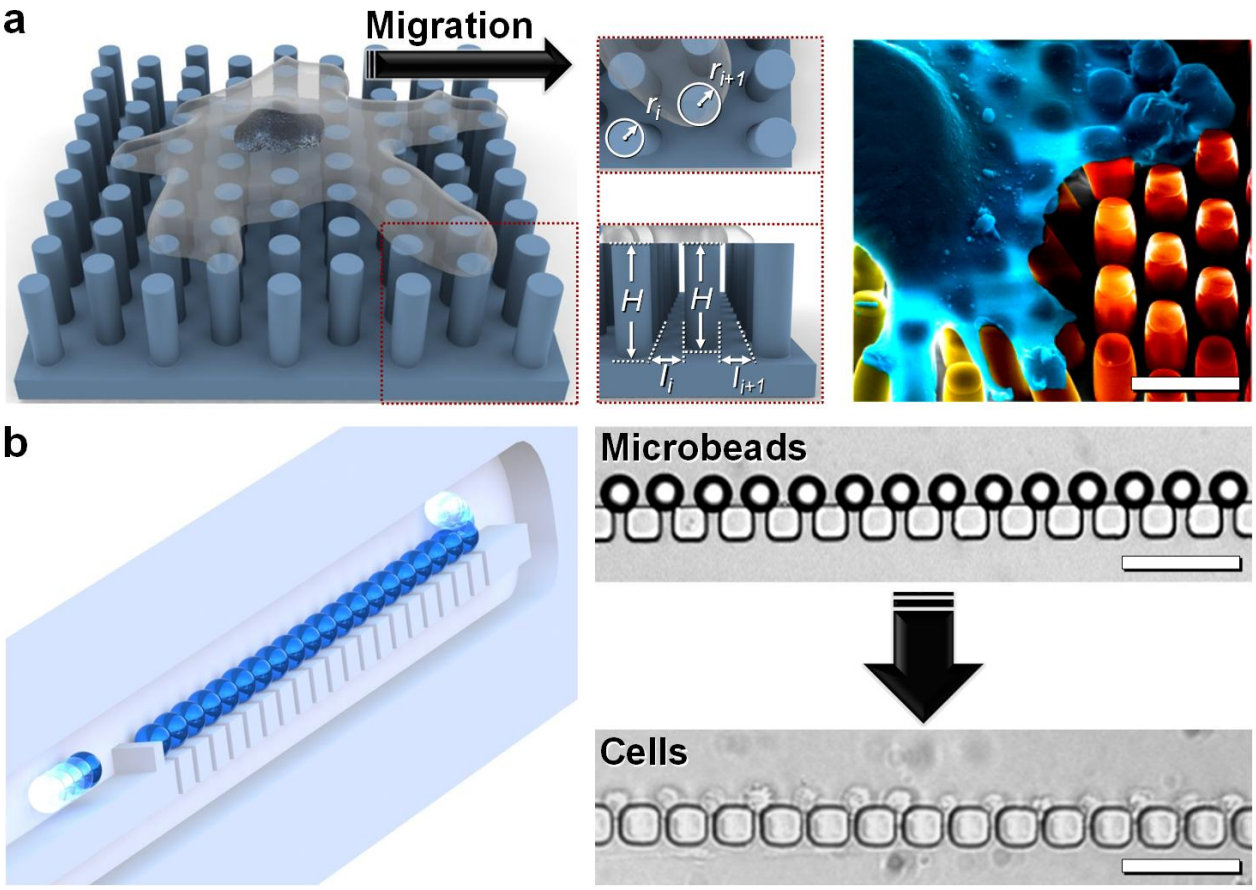

Figure 1.1 Arrayed microposts for advancing cell handling in: **(a)** static, and **(b)** dynamic (*i.e.*, microfluidic) systems. **(a)** Conceptual illustration (*left*) and false-colored SEM micrograph (*right*) of a cell seeded on a micropost array gradient. (*Left*) The biophysical properties of the micropost array can be tuned by adjusting either micropost radii (r) or interpost spacing (l) to induce unidirectional cellular migration. (*Right*) A bovine aortic endothelial cell (BAEC) (*blue*) seeded on a micropost array stiffness gradient with microposts increasing in stiffness (*yellow to red*). Scale Bar = 10 μm. **(b)** Conceptual illustration (*left*) and micrographs (*right*) of using arrayed microposts for handling microparticles (*e.g.*, microbeads and cells) in microfluidic systems. (*Left*) Initially, microfluidic systems are employed for handling suspended microbeads, which are less experimentally complex than suspended cells. (*Right*) Following experimental characterization with microbeads, the microfluidic systems are used for handling suspended cells. Scale Bars = 50 μm

platforms for improving microbead handling, with cellular testing subsequent to bead-based experimental characterization (**Fig. 1.1b**). A resettable, hydrodynamic microparticle arraying system – termed micropost array trapping (μPAT) – was developed to trap-and-release suspended microbeads and cells. To demonstrate the functionality of the μPAT technique, μPAT arrays were integrated into novel dynamic bead-based microarrays including: (*i*) a microfluidic system to facilitate the detection of multiple bio-molecules in parallel, and (*ii*) a "Microfluidic Ping Pong" (MPP) system to enable multi-stage fluidic reactions and analyses under discontinuous flow conditions. To accomplish multi-stage fluidic processess

under continuous flow conditions, a micropost array railing (μPAR) system was developed for rapidly transporting both microbeads and cells into adjacent flow streams. A multiplexed layer-by-layer (LbL) molecular synthesis process was demonstrated on microbead substrates to illustrate the robustness of the μPAR technique.

1.2 Dissertation Outline

In **Chapter 2**, the methodology of engineering micropost array gradients to induce unidirectional cellular migration *via* substrate-based biophysical stimuli is presented. An overview of prior efforts for investigating and regulating cellular processes using microenvironmental stimuli is offered, as well as prior uses of micropost arrays for cellular applications. The design and fabrication of four different classes of micropost array gradients are discussed, corresponding to: (*i*) Microtopographic Durotaxis Gradients (μ*DG*s), (*ii*) Microtopographic Dual-Axis Durotaxis Gradients (μ*DDG*s), (*iii*) Microtopographic Spatiotaxis Gradients (μ*SG*s), and (*iv*) a Microtopographic Durotaxis *versus* Spatiotaxis Gradient (μ*DSG*). The experimental methods for observing and quantifying cell movement on each of the substrates are detailed. Results for cell motility are presented and discussed. In particular, the experimental results revealed that: (*i*) μ*DG*s promoted cell migration in the direction of increasing micropost stiffness, (*ii*) μ*DDG*s promoted migration in the direction of increasing micropost stiffness, while also limiting movement perpendicular to that direction, (*iii*) μ*SG*s promoted migration in the direction of decreasing interpost spacing, and (*iv*) the spatial cues of the μ*DSG* dominated the mechanical stimuli.

In **Chapter 3**, several techniques that incorporate arrayed microposts into microfluidic systems to improve microparticle handling are presented. An overview of prior efforts for handling cells and microbeads in microfluidic systems is offered. The design and fabrication of two novel microfluidic particulate-based platforms – the resettable micropost array trapping (μPAT) system and the micropost array railing (μPAR) system – are discussed. Examples of two additional bead-based systems incorporating the μPAT technique are presented. The methods associated with the experimental procedures, data acquisition, and quantitative analyses are detailed. Results for microparticle handling are presented and discussed for each platform, with a primary focus on bead-based experiments preceding cell-based experiments.

Conclusions for the dissertation are discussed in **Chapter 4**. The efficacy of the presented micropost array-based methodologies for advancing cell handling in static and dynamic environments is summarized. Future directions and applications for the presented technologies are discussed.

Chapter 2: Micropost Array Gradients for Cell Handling

2.1 Introduction

2.1.1 Microenvironmental Cellular Stimuli

A wide range of biological processes, such as angiogenesis, immune response, and wound repair, rely strongly on environmental stimuli.[2] Elucidating the cellular response to various external cues enables researchers to better predict and control cellular behavior – a necessity for biological applications including tissue engineering, biomaterials, and regenerative medicine.[3] Cellular locomotion consists of three fundamental steps: (*i*) the cell initiates protrusive activity, (*ii*) a singular, dominant protrusion is established *via* adhesive contacts to the substratum, and (*iii*) the rear of the cell detaches from the substratum, facilitating cellular contraction.[23, 44, 45] The cellular processes involved in locomotion are influenced by a wide range of environmental cues, such as chemical,[21-24] electrical,[13, 15, 20] mechanical,[12, 14, 18] and spatial[16, 17, 46, 47] signals. Thus, diverse modalities exist for both investigating and directing cellular motility.[19]

In vivo, chemical factors (*e.g.*, chemoattractants) represent the primary environmental stimuli through which cell motility is regulated, as cells constantly interact with numerous chemical cues.[48] For cellular guidance applications both *in vivo* and *in vitro*, the use of chemical-based techniques to induce migration (*i.e.*, *via* chemotaxis or haptotaxis) can be impractical in many situations.[21-24] For example, in cases where cells are exposed to high numbers of chemical factors, it remains unclear how cells prioritize and decipher the various (and potentially conflicting) chemical stimuli.[48] Additionally, maintaining highly controlled, non-transient directional gradients of chemical factors – a necessity for guiding cellular migration – remains a considerable challenge, particularly for complex environments (*e.g.*, *in vivo*).[49, 50] Recently, researchers have revealed significant roles of biophysical cues for living cells, which could provide a promising alternative to techniques based on chemical stimuli.

2.1.2 Biophysical Cellular Stimuli

Biophysical cues, such as mechanical and spatial stimuli, have been shown to affect a variety of cellular functions. For example, researchers have observed that mechanical signals influence cellular processes including integrin reinforcement,[14, 51] cytoskeletal reorganization,[52, 53] adhesive traction,[54-56] and focal adhesion dynamics.[57, 58] For directing motility, directional migration can be regulated *via* mechanical cues – a phenomenon known as mechanotaxis. When subjected to shear stress *via* fluid flow, certain cell types migrate in the direction of the shear stress.[59-61] Similarly, when cells are inflicted with principal stress (*e.g.*, due to mechanical stimulation), subsequent migration in the direction of the mechanical force has been observed.[62] Compared to the aforementioned *active* biophysical cues, *passive* substrate-based biophysical methods offer distinct benefits for cellular guidance applications. In particular, the ability to apply non-transient biophysical stimuli to living cells without external regulation or power is advantageous for investigating and controlling motile processes.

2.1.3 Substrate-Based Mechanical Stimuli

In prior reports, researchers have shown that substrate-based mechanical stimuli influence diverse cellular processes, such as focal adhesion development[63] and stem cell lineage specification.[64, 65] Cellular migration guided by the rigidity of the substrate – a phenomenon known as durotaxis[49] – has been observed on a variety of substrates with stiffness gradients.[4, 6, 11] In order to study the cellular response to substrates of varying rigidity, researchers have employed hydrogel photopolymerization-based methods to fabricate substrates with either a low number[4-6] or high number[7-11] of substrate stiffnesses. Substrates with a low number of substrate stiffnesses are intrinsically limited because the stiffness steps are much larger than the size of a single cell and often include only two prominent stiffnesses.[4-6] In contrast, continuous rigidity gradients with high numbers of substrate stiffnesses offer superior control for directing cellular movement; however, the current methods used to fabricate continuous rigidity gradients suffer from a wide range of disadvantages, including complicated microfabrication processes, poor control over the placement and magnitude of substrate stiffness, and low repeatability.[7-11]

2.1.4 Substrate-Based Microtopographic Stimuli

Methods for engineering substrates with microtopography (*e.g.*, microgrooves or microposts) facilitate simple microfabrication, accurate feature definition, and high repeatability.[66-69] Previously, researchers have investigated the effects of microtopography on cellular migration.[25-29] On substrates with microgrooves (alternatively referred to as microridges), cells have been observed to migrate bidirectionally, parallel to the microgrooves.[27, 69] Unfortunately, the ability to induce unidirectional migration on microtopographic substrates has previously required varying the surface density of topographic features coated with extracellular matrix (ECM) proteins.[70, 71] Thus, achieving unidirectional cellular guidance using microtopographic substrates (*i.e.*, independent of collaborative chemical stimuli) has remained a significant challenge.

2.1.5 Micropost Arrays for Cellular Applications

Micropost arrays present a powerful topographic technology for cellular applications by enabling researchers to achieve high control over micropost positioning and geometry *via* simple, accurate, and repeatable microfabrication processes. Historically, researchers have exploited these advantages primarily for the application of quantifying cellular traction forces on the substrate.[68, 72-74] Specifically, when cells are seeded onto arrays of identical circular microposts, they spread over multiple posts (**Fig. 2.1a**) and physically pull at the tops of the posts, resulting in visible displacements (**Fig. 2.1b**). By modeling each micropost as a mechanical cantilever, the linear stiffness at the top of the micropost can be approximated based on its geometric and material properties (**Fig. 2.1c**).[67, 68] Thus, by using both the estimated micropost stiffness and the observed displacements at the top of the posts, the cellular traction forces on the substrate can be calculated.[68, 72-74]

In addition to quantifying cellular traction forces, researchers have recently employed micropost arrays as a means to apply biophysical stimuli to seeded cells. For example, prior reports have demonstrated the use of identical elliptical microposts for applying bidirectional

substrate stiffness cues to cells, because the micropost stiffness parallel to the major axes is inherently larger than the stiffness parallel to the minor axes.[66, 75] Experimental results revealed bidirectional migration along the stiffer axis, consistent with *a priori* durotaxis predictions. However, it should be noted that the arrays were designed with closer spacing between microposts along the major axes (relative to the perpendicular spacing between posts along the minor axes), and thus, it is possible that this variable spacing may have contributed to the observed migratory behavior.[66, 75] Using micropost arrays with different heights (and therefore, different micropost stiffnesses), researchers have also shown that micropost stiffness can be a determinant factor for stem cell fate decisions.[65]

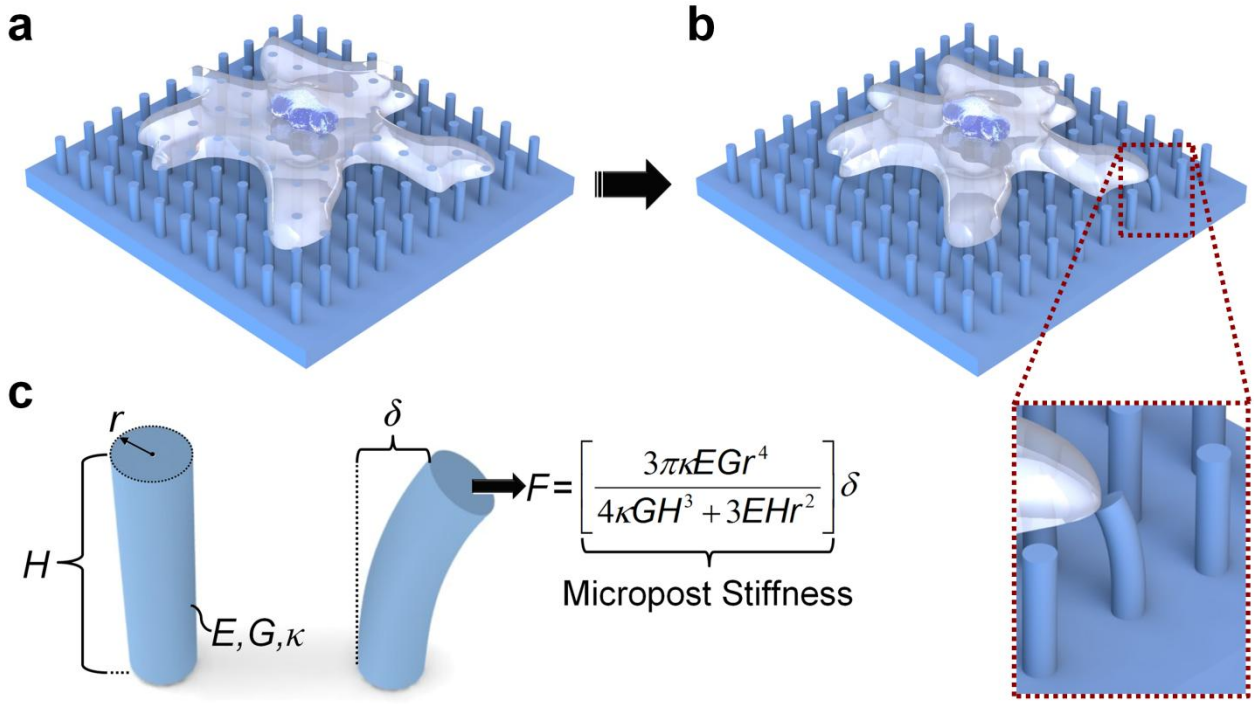

Figure 2.1 Conceptual illustrations of micropost arrays employed for the application of quantifying cellular traction forces on the substrate. **(a)** A cell spreads over multiple, identical circular microposts, attaching to the top surface of the posts. **(b)** The cell then physically pulls at the tops of the microposts, resulting in visible displacements (as shown in the expanded view). **(c)** By modeling the micropost as a mechanical cantilever, the linear stiffness at the top of the micropost is derived from its geometric and material properties, including the Young's Modulus (E), shear modulus (G), shear coefficient (κ), micropost height (H), and micropost radius (r). A force applied at the top of the micropost (F), parallel to the substrate, results in a displacement at the top of the micropost (δ).

2.2 Design of Micropost Array Gradients for Cell Handling

Micropost arrays present a unique and powerful tool for independently engineering the stiffness of the substrate and the spacing of substrate binding sites – two physical cues that influence cellular attachment and membrane extension, respectively. Here, the technique of using micromachining processes to fabricate micropost array gradients is proposed to apply these substrate-based biophysical stimuli to seeded cells. Micropost array gradients with varying stiffness and interpost spacing were designed to achieve unidirectional cellular guidance *via* micropost stiffness cues (*i.e.*, durotaxis) and microtopographic spatial cues (a phenomenon herein referred to as *spatiotaxis*), respectively. Four classes of micropost array gradients were designed: (*i*) Microtopographic Durotaxis Gradients (*μDG*s), (*ii*) Microtopographic Dual-Axis Durotaxis Gradients (*μDDG*s), (*iii*) Microtopographic Spatiotaxis Gradients (*μSG*s), and (*iv*) a Microtopographic Durotaxis *versus* Spatiotaxis Gradient (*μDSG*).

2.2.1 Microtopographic Durotaxis Gradients (*μDG*s)

Figure 2.2a illustrates the *μDG* concept. In contrast to prior reports of microposts with uniform radii[67, 68] or identical shapes,[66, 75] here, the radii of arrayed microposts (**Fig. 2.2a** – '*r*') were increased in a single, designed direction. A constant interpost spacing (**Fig. 2.2a** – '*l*') of 2 *μ*m was designed along the axis of increasing micropost radii. The stiffness of a micropost can be geometrically tuned by adjusting either the height or radius of the micropost.[68, 72-74] For fabricating gradients of micropost stiffness, modulating micropost radii while maintaining a uniform structural height over the length of the substrate facilitates simple fabrication *via* one-

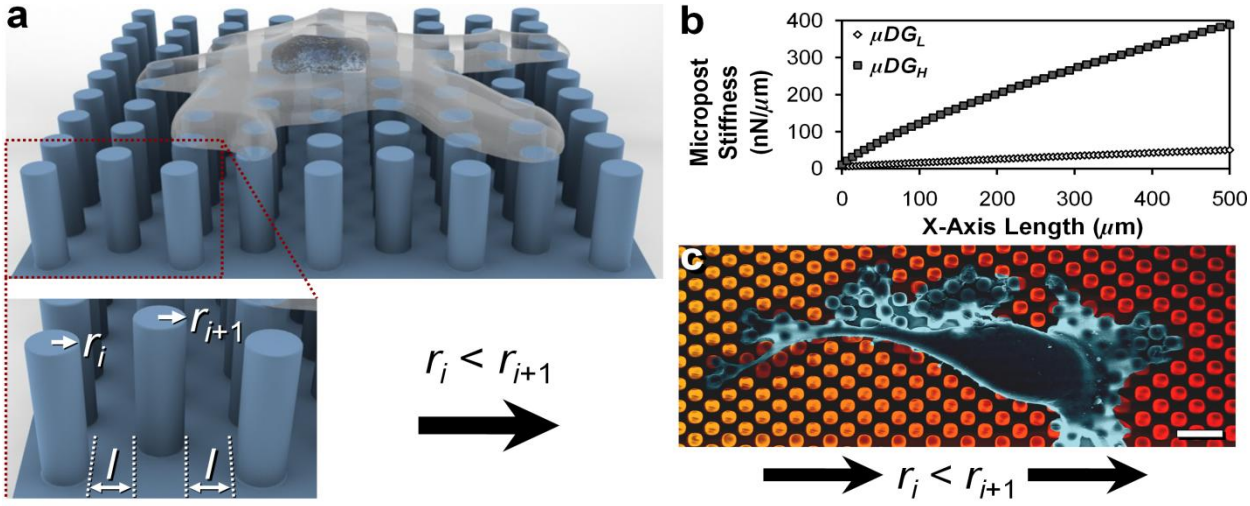

Figure 2.2 Microtopographic Durotaxis Gradient (*μDG*) design. **(a)** Conceptual illustration of a cell seeded on a microtopographic stiffness gradient with an enlarged view of individual microposts with increasing radii (*r*) and equivalent interpost spacing (*l*). **(b)** Micropost stiffness over the length of the micropost array durotaxis gradient with low gradient strength (μDG_L; *white diamonds*) and high gradient strength (μDG_H; *dark grey squares*). **(c)** False-colored SEM micrograph of a bovine aortic endothelial cell (BAEC) (*blue*) seeded on a micropost array stiffness gradient with microposts increasing in stiffness (*yellow to red*). Scale Bar = 10 *μ*m

mask soft lithography processes. Thus, the heights of the microposts were kept constant at 7 μm while the radii of the microposts were increased over the length of the substrates.

Two types of μDGs were designed corresponding to: (*i*) low gradient strength (μDG_L), and (*ii*) high gradient strength (μDG_H). Both substrate areas were approximately 500×500 μm^2, consisting of thousands of microposts. Micropost radii were increased continuously over the lengths of the substrates, corresponding to post-to-post stiffness increments of 0.5 nN/μm and 7.5 nN/μm for the μDG_L and the μDG_H, respectively (**Fig. 2.2b**). The μDG_L included radii ranging from 1 to 2 μm, corresponding to physiologically relevant stiffnesses of 5 to 50 nN/μm.[68] The μDG_H included radii ranging from 1 to 3 μm, corresponding to micropost stiffnesses of approximately 5 to 390 nN/μm. When seeded cells spread on the micropost array gradients, they interact with microposts that increase in stiffness in a single, designed direction. For example, **Figure 2.2c** shows a false-colored SEM image of a bovine aortic endothelial cell (BAEC) spread over microposts that include 28 distinct stiffness values, with micropost stiffness increasing from post-to-post rightward (*yellow to red*).

To preclude the potential effects of substrate-immobilized chemical gradients[60] and variable surface densities of topography,[70, 71] the area surrounding individual microposts was modulated to maintain a consistent percentage of extracellular matrix protein coverage (*%ECM*) and topographic surface area for regimes of different micropost radii. Specifically, while the interpost spacing along the axis of increasing stiffness was held constant at 2 μm, the interpost spacing perpendicular to the axis of increasing stiffness was adjusted to compensate for changes in micropost radii such that:

$$\%ECM = \frac{\pi r^2}{(2r+s)(2r+l)} = \text{Constant} \qquad \textbf{Equation 2.1}$$

where r is the micropost radius, s is the spacing between microposts perpendicular to the axis of increasing stiffness, and l is the interpost spacing parallel to the axis of increasing stiffness. To maintain consistency between the two gradients, both the μDG_L and the μDG_H included equivalent *%ECM* and topographic surface densities of 20%.

2.2.2 Microtopographic Dual-Axis Durotaxis Gradients (*μDDG*s)

A second class of micropost array durotaxis gradients was designed to offer two improvements over the μDGs. First, the use of circular microposts is inherently limiting because the micropost stiffness remains consistent 360º around the post. In contrast, the anisotropic structure of elliptical microposts, which results in a higher micropost stiffness along the major axes relative to the stiffness along the minor axes,[66, 75] could further extend the efficacy of the μDG methodology. Secondly, because the radii of arrayed circular microposts were increased over the length of the μDGs, the micropost-specific top surface area increased as well. Currently, it remains unclear how increasing the micropost-specific top surface area in the absence of gradients in *%ECM* or topographic density might affect cell motility. To bypass such concerns, the μDDGs were designed with a consistent micropost-specific top surface area over the length of the substrates.

Figure 2.3a illustrates the *μDDG* concept. To enhance unidirectional control of cell migration *via* mechanical stimuli, the *μDDG*s were designed with dual-axis stiffness cues: (*i*) the semi-major axes of elliptical microposts (**Fig. 2.3a** – '*a*') increase in a single direction (*i.e.*, while the semi-minor axes (**Fig. 2.3a** – '*b*') are decreased) to promote migration in the direction of increasing stiffness, and (*ii*) the stiffness along the major axes is comparatively higher to limit movement perpendicular to the axis of increasing stiffness. The semi-minor axes (**Fig. 2.3a** – '*b*') were decreased over the length of the arrays to ensure that all of the microposts included identical micropost-specific top surface areas (*i.e.*, $\pi \times a \times b$) of 16 μm^2. A constant interpost spacing (**Fig. 2.3a** – '*l*') of 2 μm was designed along the axis of increasing stiffness. All of the microposts included a constant height of 7 μm.

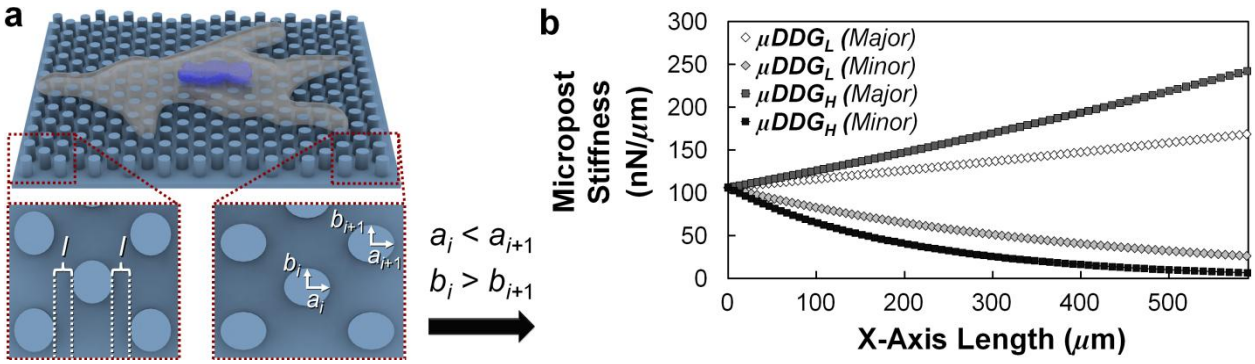

Figure 2.3 Microtopographic Dual-Axis Durotaxis Gradient (*μDDG*) design. **(a)** Conceptual illustration of a cell seeded on a *μDDG* with enlarged views of individual microposts with increasing semi-major axes (*a*), decreasing semi-minor axes (*b*), and equivalent interpost spacing (*l*). **(b)** Micropost major axes stiffness and minor axes stiffness over the length of the micropost array dual-axis durotaxis gradients with low gradient strength (*μDDG$_L$*; *diamonds*) and high gradient strength (*μDDG$_H$*; *squares*).

In contrast to circular microposts, the stiffness of elliptical microposts varies with respect to the angle of interest.[66, 75] Specifically, the linear stiffness of an elliptical micropost can be approximated as:

$$k(\theta) = \frac{3\pi\kappa EGab(a^2\cos^2\theta + b^2\sin^2\theta)}{4\kappa GH^3 + 3EH(a^2\cos^2\theta + b^2\sin^2\theta)} \qquad \textbf{Equation 2.2}$$

where E is the Young's Modulus, G is the shear modulus, κ is the shear coefficient, H is the micropost height, a is the micropost semi-major axis, b is the micropost semi-minor axis, and θ is the angle of interest with respect to the major axis. Solving for $\theta = 0^o$ (*i.e.*, for the major axis) and for $\theta = 90^o$ (*i.e.*, for the minor axis) leads to the two fundamental linear stiffnesses:

$$k_{major} = k(0°) = \frac{3\pi\kappa EGa^3 b}{4\kappa GH^3 + 3EHa^2} \qquad \textbf{Equation 2.3}$$

and

$$k_{minor} = k(90°) = \frac{3\pi\kappa EGab^3}{4\kappa GH^3 + 3EHb^2} \qquad \textbf{Equation 2.4}$$

where k_{major} is the major axis stiffness, and k_{minor} is the minor axis stiffness.

Two types of *μDDG*s were designed corresponding to: (*i*) low gradient strength (μDDG_L), and (*ii*) high gradient strength (μDDG_H). The μDDG_L included semi-major axes increasing from 2.25 to 3 μm while the semi-minor axes were simultaneously decreased from 2.25 to 1.7 μm, corresponding to changes in k_{major} and k_{minor} from approximately 100 to 170 nN/μm and 100 to 25 nN/μm, respectively (**Fig. 2.3b** – *diamonds*). For the μDDG_L, k_{major} was increased by increments of approximately 1 nN/μm from post-to-post. The μDDG_H included semi-major axes increasing from 2.25 to 4.1 μm while the semi-minor axes were simultaneously decreased from 2.25 to 1.25 μm, corresponding to changes in k_{major} and k_{minor} from approximately 100 to 240 nN/μm and 100 to 10 nN/μm, respectively (**Fig. 2.3b** – *squares*). For the μDDG_H, k_{major} was increased by increments of approximately 2 nN/μm from post-to-post.

In addition to the microtopographic gradients, two control substrates were also designed: (*i*) a negative control with identical circular posts of 2.25 μm in radius (C_C), and (*ii*) a bidirectional control of identical elliptical microposts of 3 μm in semi-major axes, and 1.7 μm in semi-minor axes (C_E). For the C_C, all of the microposts included stiffnesses of approximately 100 nN/μm 360º around the post. For the C_E, all of the microposts included a k_{major} of 170 nN/μm and a k_{minor} of 25 nN/μm. Both control substrates included micropost-specific top surface areas equivalent to that of the *μDDG*s.

To preclude the potential of substrate-immobilized chemical gradients and variable surface densities of topography from affecting the migratory results, the interpost spacing perpendicular to the axis of increasing stiffness was adjusted to compensate for changes in micropost geometry such that:

$$\%ECM = \frac{\pi ab}{(2b+s)(2a+l)} = \text{Constant} \qquad \textbf{Equation 2.5}$$

where *s* is the spacing between microposts perpendicular to the axis of increasing stiffness and *l* is the interpost spacing parallel to the axis of increasing stiffness (which was held constant at 2 μm over the length of the arrays). To maintain consistency between the two gradients as well as the control arrays, all of the substrates included equivalent *%ECM* and topographic surface densities of 25%. Additionally, all of the substrate areas were approximately 600×600 μm^2.

2.2.3 Microtopographic Spatiotaxis Gradients (*μSG*s)

Due to the high user control over micropost positioning afforded by micropost array fabrication processes, the spacing between microposts (*i.e.*, the spacing between substrate attachment sites) can be adjusted to apply biophysical spatial cues to seeded cells. To promote migration *via* the variable spacing of substrate binding sites (*i.e.*, induce spatiotaxis), *μSG*s were designed as shown in **Figure 2.4**. Over the length of the substrate, the interpost spacing (**Fig. 2.4a** – '*l*') was decreased from post-to-post in a single direction. All of the microposts

included uniform structural heights of 7 μm. To preclude the effects of variable mechanical cues, the μSGs included identical circular microposts with equivalent radii of 1.5 μm.

Two types of μSGs were designed corresponding to: (*i*) low gradient strength (μSG_L), and (*ii*) high gradient strength (μSG_H). For the μSG_L, the interpost spacing was decreased from approximately 3.9 to 3 μm over the length of the array, which corresponds to an average spacing decrease of 10 nm from post-to-post (**Fig. 2.4b** – *white diamonds*). For the μSG_H, the interpost spacing was decreased from approximately 4.6 to 2 μm over the length of the array, which corresponds to an average spacing decrease of 30 nm from post-to-post (**Fig. 2.4b** – *dark grey squares*).

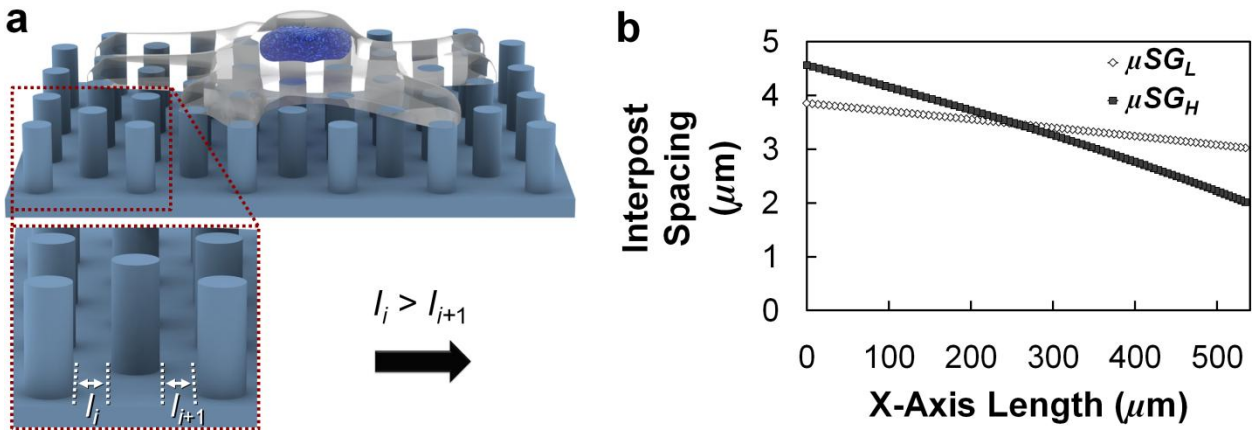

Figure 2.4 Microtopographic Spatiotaxis Gradient (μSG) design. **(a)** Conceptual illustration of a cell seeded on a μSG with an enlarged view of individual microposts with decreasing interpost spacing (*I*). **(b)** Interpost spacing over the length of the micropost array spatiotaxis gradients with low gradient strength (μSG_L; *white diamonds*) and high gradient strength (μSG_H; *dark grey squares*).

To preclude the effects of substrate-immobilized chemical gradients and variable topographic densities, the interpost spacing perpendicular to the axis of decreasing spacing was adjusted to compensate for changes in interpost spacing along the axis of decreasing spacing such that:

$$\%ECM = \frac{\pi r^2}{(2r+s)(2r+I)} = \text{Constant} \qquad \textbf{Equation 2.6}$$

where *s* is the spacing between microposts perpendicular to the axis of decreasing spacing, *I* is the interpost spacing parallel to the axis of decreasing spacing, and *r* is the micropost radius (which was held constant at 1.5 μm). In addition to the μSGs, a negative control substrate (*C*) was designed with equivalent spacing in each direction (*i.e.*, $s = I = 3$ μm). To maintain consistency between the two μSGs as well as the negative control array, all of the substrates included equivalent *%ECM* and topographic surface densities of 15%. Additionally, all of the substrate areas were approximately 550×550 μm^2.

2.2.4 Microtopographic Durotaxis *versus* Spatiotaxis Gradients (*μDSG*s)

Despite the significant development of micro- and nanotopographic substrates for mechanobiological applications, little is known regarding the impact of micropost spacing on the mechanical response of living cells. To elucidate the effects of simultaneous microtopographic mechanical and spatial cues on cell motility, a micropost array with variable micropost stiffness and interpost spacing was constructed. **Figure 2.5** illustrates the design of the *μDSG*. Over the length of the substrate, both the interpost spacing (**Fig. 2.5** – '*l*') and the radii of arrayed circular microposts (**Fig. 2.5** – '*r*') were decreased from post-to-post in a single direction. All of the microposts were maintained at a uniform structural height of 7 μm. As shown in **Figure 2.5b**, the interpost spacing was decreased from approximately 6 *μ*m to 2 *μ*m over the length of the array, which corresponds to an average spacing decrease of 40 nm from post-to-post. Simultaneously, micropost radii were decreased from 2 *μ*m to 1 *μ*m, with micropost geometries and post-to-post stiffness increments identical to the μDG_L design (*i.e.*, for comparison purposes). Thus, the *μDSG* included mechanical migratory stimuli in the direction of increasing micropost stiffness, opposite the direction of decreasing interpost spacing. To maintain a consistent *%ECM* over the length of the array, the interpost spacing perpendicular to the direction of decreasing interpost spacing was adjusted as described in **Equation 2.1**, with the caveat that *s* was always equivalent to *I*. The *%ECM* and topographic surface density for the *μDSG* were held constant at 20%, which is consistent with the μDG_L design.

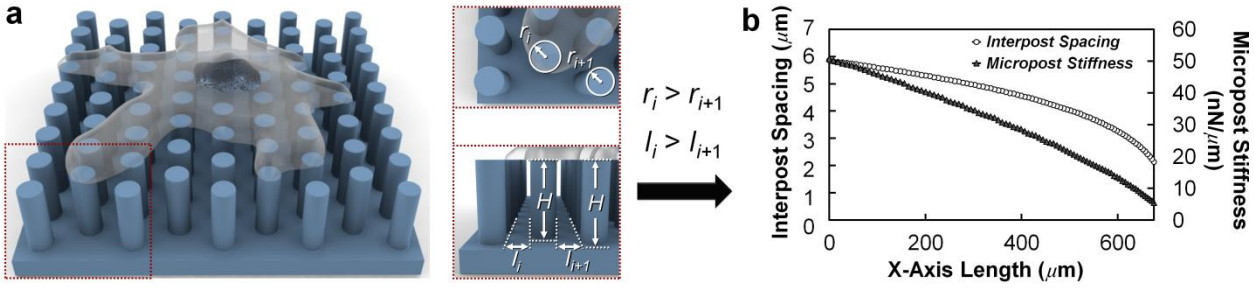

Figure 2.5 Microtopographic Durotaxis *versus* Spatiotaxis Gradient (*μDSG*) design. **(a)** Conceptual illustration of a cell seeded on a *μDSG* with an enlarged view of individual microposts with decreasing radii (*r*), decreasing interpost spacing (*l*), and constant height (*H*). **(b)** Interpost spacing (*white circles*) and micropost stiffness (*dark grey triangles*) over the length of the *μDSG*.

2.3 Materials and Methods

2.3.1 Micropost Array Gradient Fabrication and Preparation

The micropost arrays were fabricated *via* standard soft lithography processes. Chrome photomasks (*Fineline Imaging*) were designed with micropost geometry and placement customized as described in **Section 2.2**. To fabricate the negative master, Si wafers were piranha cleaned (**Fig. 2.6a**). The positive photoresist, SPR-220 (*Rohm and Haas Electronic Materials*), was spin-coated onto the clean Silicon wafers at 50 rpm for 30 seconds, and then 3500 rpm for 45 seconds, resulting in a thickness of approximately 7 μm. Thereafter, a softbake was performed on a hotplate at 115 °C for 5 minutes, and the wafers were cooled at room temperature (20-25 °C) to avoid thermal shock. The microfeatures were defined using projection photolithography with a 10× reduction step and repeat camera (*GCA-6200 Wafer Stepper, General Signal Corporation*). After a wait time of at least 30 minutes, a post exposure bake was performed at 115 °C for 6.5 minutes. The wafer was developed in a beaker of MF-26A developer for 15 minutes, and then rinsed thoroughly with deionized (DI) water and dried with N_2. A hardbake was performed on a hotplate at 80 °C for 5 minutes to finish the negative master fabrication process (**Fig. 2.6b**).

Using the developed photoresist as a negative master, the silicone elastomer, poly(dimethylsiloxane) (PDMS) (*Sylgard 184, Dow Corning*), was poured onto the wafer at a 10:1 (base : curing agent) ratio and cured at room temperature (20-25 °C) in a vacuum chamber for approximately two days (**Fig. 2.6c**). The fabricated microtopographic substrates were removed from the negative master (**Fig. 2.6d**). Solvents were not used during the removal process. To remove residual photoresist, the substrates were submerged in 100% ethanol and sonicated for 10 minutes. In a clean hood, the 100% ethanol was aspirated from the substrates until the substrates were dry. To improve cellular attachment to the top surfaces of the microposts, the substrate was selectively microcontact-printed with the ECM protein, fibronectin, *via* previously described processes.[67] Briefly, the microtopographic substrates were treated with O_2 plasma (*RTE73 AMNS-500- E, Plasma Therm*) for 5 minutes to render the surfaces hydrophilic. The surface of PDMS stamps were incubated with fibronectin (25 μg/ml in DI water; *Sigma-Aldrich*) for one hour to allow for protein adsorption (**Fig. 2.6e** - *inset*). Fibronectin-coated stamps were brought into contact with the microtopographic substrates for 15 minutes to facilitate the adsorption of fibronectin at the tops of the microposts (**Fig. 2.6e**). After the stamps were removed, the microtopographic substrates were sterilized in successive dishes of 100% ethanol and 70% ethanol for one minute each. The micropost array substrates were then submerged in two successive dishes of DI water for one minute each to remove excess 70% ethanol. The micropost array gradients were submerged in 0.2% Pluronics F127 (*Sigma Aldrich*) for 30 minutes to limit cell attachment and protein adsorption at locations other than the top surfaces of the microposts (**Fig. 2.6f**). Lastly, the substrates were submerged in two successive dishes of phosphate buffered saline (PBS) (*Sigma Aldrich*) for one minute each (*i.e.*, to remove excess Pluronics F127), and then stored in sterile PBS in an incubator at 37 °C until use.

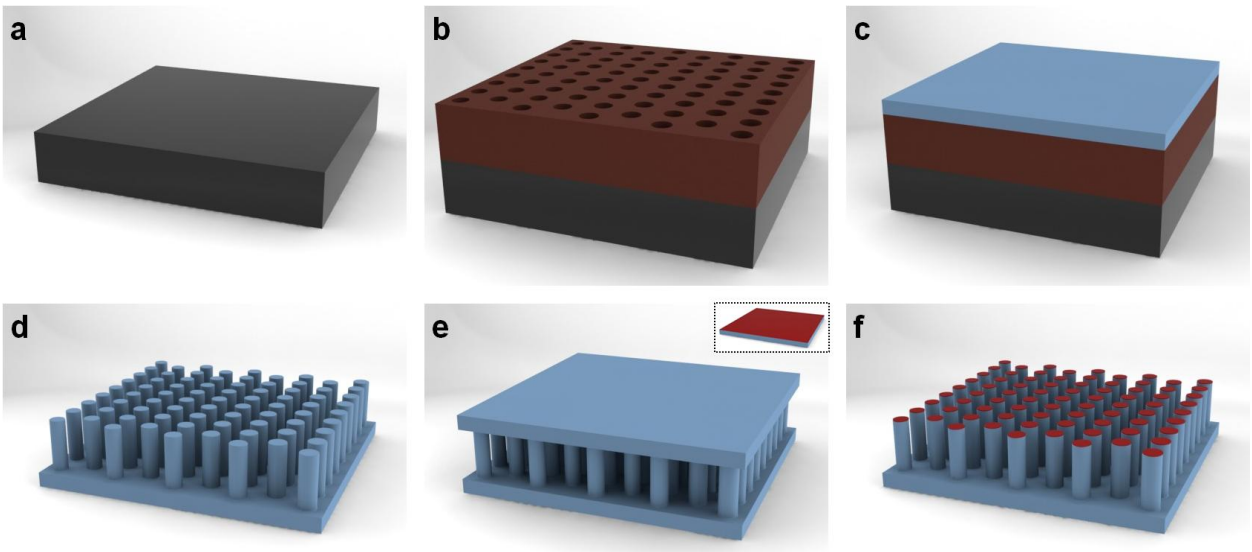

Figure 2.6 Conceptual illustrations of the micropost array gradient fabrication process. **(a)** Silicon wafers were piranha cleaned. **(b)** Microfeatures were photolithographically defined using projection photolithography. The developed wafer was used as a negative master. **(c)** The silicone elastomer, poly(dimethylsiloxane) (PDMS), was poured onto the negative master. **(d)** After curing, the PDMS was removed from the negative master. **(e)** Flat PDMS stamps coated with extracellular matrix (ECM) protein (*inset*) were used to micro-contact print ECM protein onto the top surfaces of the microposts. **(f)** The PDMS stamps were removed, resulting in micropost array gradients with ECM protein coated onto the top surfaces of the microposts.

2.3.2 Bovine Aortic Endothelial Cell (BAEC) Passaging for Migration Studies

First, sterile 0.5X trypsin, Dulbecco's Modified Eagle Medium (DMEM) media (supplemented with 10% fetal bovine serum (FBS) and 1% penicillin-streptomycin; all obtained from *Gibco, Invitrogen*), PBS, and DI water were placed in a temperature-controlled water bath (approximately 37 °C) for 20-30 minutes. BAEC cultures were removed from the incubator and inspected under the microscope to ensure a lack of contamination. The media was aspirated and 5-6 ml of PBS was added to wash the cells. The PBS was aspirated and 2.5 ml of 0.5X trypsin was added to the tissue culture dish. The dish was placed in the incubator for at least 5 minutes until the cell monolayer detached from the surface (with most of the cell clusters broken down). Then, 6 ml of DMEM media was added to the dish to deactivate the trypsin. Using a pipette, the remaining clusters were broken apart in the tissue culture dish and subsequently transferred to a 15 ml centrifuge tube. After centrifuging at 1000 RPM for 4 minutes, the media was aspirated from the centrifuge tube (leaving the bead pellet) and replaced with 5 ml of new media. Meanwhile, 7.5 ml of media was added to each new tissue culture dish. After re-suspending the cells by thoroughly mixing the new cell-media suspension, 0.5 ml of the suspension was added to the aforementioned new culture dish (8 ml total) and stored in an incubator for future studies. The remaining cell suspension was used for the migration studies.

2.3.3 Methods for Observing Cell Migration on μDG and μDSG Substrates

Initially, CO_2 independent media (*Invitrogen*) was placed in the temperature-controlled water bath (approximately 37 °C) for 20-30 minutes. The microcontact-printed micropost arrays from **Section 2.3.1** were removed from the incubator. The PBS was aspirated from the dish (without touching the micropost arrays). Using tweezers, the microtopographic substrates were lifted from the dish, and the PBS was aspirated from the bottom of the substrates. The substrates were placed onto an autoclaved microscope slide and gently pressed to improve contact. After thoroughly mixing the remaining cell suspension from **Section 2.3.2** to ensure even cell distributions prior to cell seeding, 10 μl of the suspension was used to seed each micropost array pattern. Next, the micropost array substrates were placed in a non-tissue culture petri dish, with one ml of DMEM media added to the dish. The dish was placed in the incubator for up to one hour to promote cell attachment to the microposts.

A Griffin beaker with 700 ml of DI water was placed inside the microscope incubator and the temperature was set to 37 °C. Double sided tape was soaked in 70% ethanol for 30 minutes and placed in the tissue culture hood. Both sides were sterilized *via* UV treatment for 30 minutes. The 70% ethanol was aspirated and the tape was rinsed with DI water for 2 minutes. The water was aspirated until the tape dried completely. A kimwipe was soaked in 70% ethanol, placed flat inside the hood and UV treated for 20 minutes. An autoclaved microscope slide was placed onto the dry kimwipe. Using the glass cutter, the slide was scored at its midpoint. The kimwipe is folded over the slide, which was then manually broken into two equal pieces. The slide pieces were placed into a non-tissue culture treated petri dish and rinsed with 13 ml of DI water. The DI water and any rogue glass particulates were aspirated. Using tweezers and the aspirator, the slide pieces were dried completely. Using a razor or scalpel, the sterile double sided tape was cut to the length of the slide pieces. The tape was placed on the base of the petri dish, parallel to each other and less than 2 cm apart. The slide pieces were placed on top of the tape, parallel to each other and approximately 1 cm apart (**Fig. 2.7a**).

The slide with the seeded micropost array substrates was removed from the incubator. The remaining media was aspirated until the slide dried. Meanwhile, 9-10 ml of CO_2 independent media was added to the dish with the tape and slide pieces, covering the base. Any bubbles generated were manually aspirated. The slide with the micropost arrays was inverted (*i.e.*, the patterns faced downward) and carefully placed in between the slide pieces to avoid bubbles (**Fig. 2.7b**). Any bubbles generated were aspirated. To submerge all of the slides, 10-15 ml of CO_2 independent media was added to the dish. Lastly, the dish was covered and transferred to the temperature and humidity controlled chamber of the microscope (*i.e.*, maintained at 37 °C). Time-lapse videos of cell movement on the micropost array gradients were generated in parallel from phase contrast microscopic images taken every 20 minutes over the course of 18-hour studies using an Eclipse TE300 inverted microscope (*Nikon*) with Simple PCI software (*Compix, Inc.*).

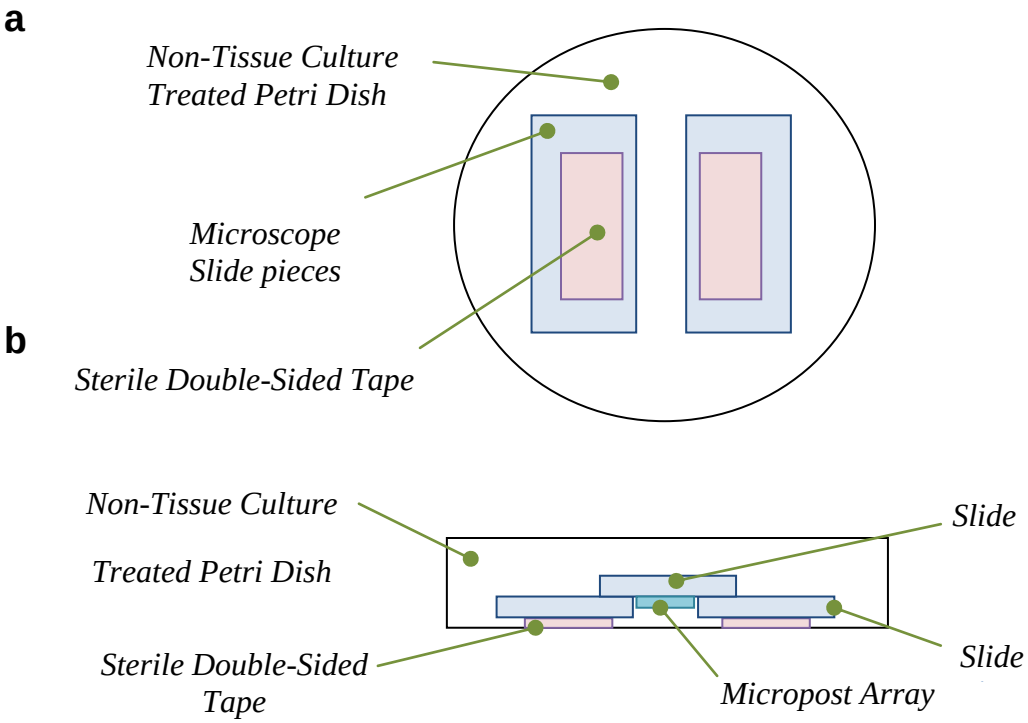

Figure 2.7 Conceptual illustrations of the setup assembly for time-lapse microscopy for μDG and μDSG cell studies. **(a)** Bottom view before placement of the slide with the inverted micropost arrays. **(b)** Side view after placement of the slide with the inverted micropost arrays.

2.3.4 Methods for Observing Cell Migration on μDDG and μSG Substrates

For observing cell movement *μDDG* and *μSG* substrates, first, CO_2 independent media (*Invitrogen*) was placed in the water bath for 20-30 minutes. Microcontact-printed micropost array gradients were removed from the incubator. Using tweezers, the micropost arrays were lifted from the dish, and the PBS was aspirated from the bottom of the substrates. The substrates were placed in the wells of a sterile Costar® 6-well tissue culture-treated plate (*#3516, Corning Inc.*) and gently pressed to improve contact. Thereafter, 2.5 ml of cell media was added to each of the wells with substrates. After thoroughly mixing the remaining cell suspension (described in **Section 2.3.2**) to ensure even cell distributions prior to cell seeding, 0.25 ml of the suspension was loaded into each of the wells with substrates. The 6-well plate was then placed in the incubator for 30 minutes to promote cell attachment to the microposts.

The remaining media was aspirated from each of the wells with substrates and replaced with 4 ml of CO_2 independent media. Any bubbles generated were manually aspirated. The 6-well plate was transferred to a temperature and humidity controlled chamber of the microscope (*i.e.*, maintained at 37 °C). Time-lapse videos of cell movement on all of the array designs were generated in parallel from phase contrast microscopic images taken every 20 minutes over the course of 18-hour studies using an ImageXpress® Micro System (*Molecular Devices*) with a Photometrics CoolSNAP$_{HQ}$ digital charge-coupled device (CCD) camera and MetaXpress software (*v. 3.1.0.89, Molecular Devices*).

2.3.5 Data Acquisition and Analysis for Cell Migration Studies

Because cell-cell interactions can affect directional migration,[76] data was collected from single cells with only substrate contact (*i.e.*, no cell-cell interactions). The time-lapse videos were analyzed using an independently designed cell tracking program in conjunction with the software ImageJ (*National Institute of Health* (*NIH*), *USA*) to manually track cell area centroids with time to determine net cell displacements and velocities. Experimental results are presented as mean ± standard error of the mean (s.e.m.). The *p* values for this study were calculated *via* unpaired *Student's t tests*. Briefly, the sample means and standard deviations were calculated directly from the migratory data. The s.e.m. was calculated by dividing the standard deviation by the square root of the sample size (*n*). The *t* value was calculated by dividing the difference between two means by the corresponding standard error of the difference between two means. With the number of degrees of freedom (the total *n* minus 2) and the *t* value, the corresponding two-tailed *p* values were determined to assess statistical significance. Differences with a *p* value less than 0.05 were considered statistically significant.

2.4 Results and Discussion

2.4.1 Cell Motility on *μDG*s

Experimental observations revealed that both *μDG*s influenced directional motility, as seeded BAECs migrated preferentially in the direction of increasing micropost stiffness. **Figure 2.8a** shows sequential time-lapse images of a BAEC (*white arrows*) migrating in the direction of increasing micropost stiffness (*black arrow*) on the μDG_L. The two-dimensional averaged 18-hour cell paths for migration on the μDG_L and μDG_H are shown in **Figure 2.8b** and **Figure 2.8c**, respectively. On the μDG_L, seeded BAECs were found to displace an average of 26.5±8.7 μm (n = 23 cells) in the direction of increasing micropost stiffness by the end of the 18-hour studies (**Fig. 2.8d**). The maximum observed displacements during the studies were 141 μm for cell movement in the direction of increasing micropost stiffness and 45 μm for displacement opposite that direction. At the end of the studies, 70% (16 from a total of 23) of BAECs exhibited displacement in the direction of increasing stiffness relative to their initial positions at the start of the studies.

Higher gradient strength was found to enhance the directional response. By the end of the studies, cells on the μDG_H displaced an average of 41.9±14.7 μm in the direction of increasing micropost stiffness (**Fig. 2.8e**), with maximum observed displacements of 145 μm for movement in the direction of increasing stiffness and 24 μm for displacement opposite that direction. By the end of the 18-hour studies, the percentage of cells that exhibited displacement in the direction of increasing micropost stiffness increased to 77% (10 from a total of 13 cells). These results are consistent with past studies of the cellular response to substrate stiffness cues.[9, 10, 49] Similar to prior work, increased gradient strength was found to enhance cell migration in the direction of increasing substrate stiffness.[9]

The speed of cell movement was also found to be affected by the micropost array gradients during the 18-hour studies. Specifically, cell speeds were observed to vary with respect to the direction of the mechanical stimuli. For migration in the direction of increasing micropost stiffness, BAECs on the μDG_L and μDG_H exhibited average speeds of 7.5±0.5 μm/hr and 7.0±0.7 μm/hr, respectively (**Fig. 2.9**). For movement opposite the direction of increasing stiffness, the average speed of BAEC migration on the μDG_L decreased to 6.6±0.5 μm/hr; however, this difference was not statistically significant (p = 0.24). In contrast, the average speed of BAEC migration on the μDG_H decreased significantly to 4.8±0.6 μm/hr for movement opposite the direction of increasing stiffness ($p < 0.05$). Additionally, although the average cell speed did not differ significantly between substrates for movement in the direction of increasing micropost stiffness (p = 0.61), higher gradient strength was found to significantly reduce the average cell speed for migration opposite that direction ($p < 0.05$) (**Fig. 2.9**).

Although the cellular response to the microtopographic mechanical stimuli was found to be consistent with durotaxis predictions and prior work, the experimental results for the *μDG*s cannot be attributed exclusively to cellular durotaxis. For the *μDG*s, the spacing surrounding individual microposts was modulated to ensure that the overall *%ECM* and topographic surface area remained constant over both microtopographic substrates (**Eq. 2.1**); however, it remains unclear how increasing the micropost-specific top surface area in the absence of gradients in

%ECM or topographic density might affect cell motility. Thus, it is possible that the increasing micropost-specific top surface area may have contributed to the observed durotaxis results.

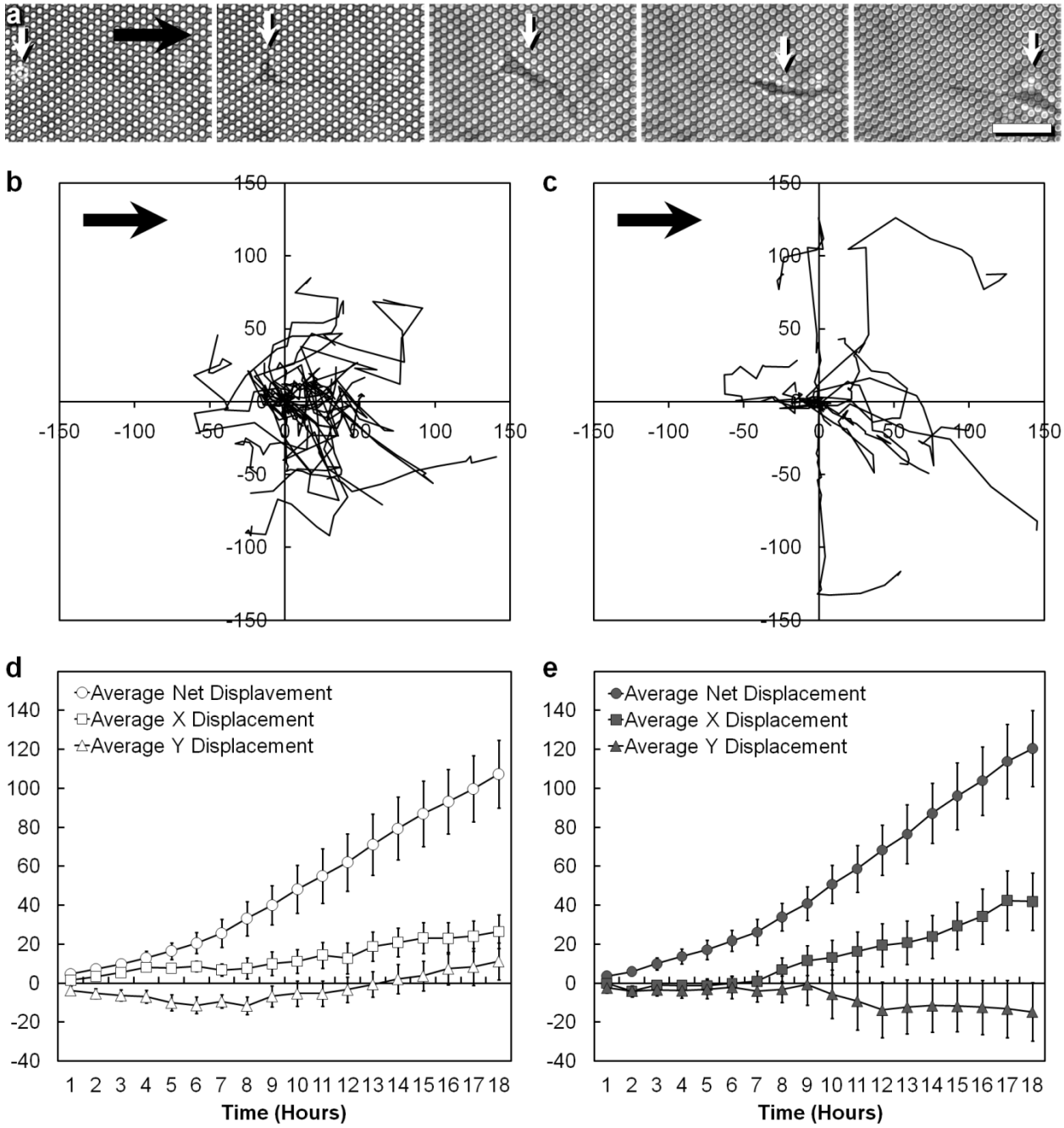

Figure 2.8 Experimental results for BAEC migration on the *μDG*s over the course of 18-hour studies. **(a)** Sequential time-lapse images of a BAEC (*white arrows*) migrating in the direction of increasing micropost stiffness (*black arrow*) on the μDG_L. Scale Bar = 50 μm. **(b-c)** Cell paths for: **(b)** 23 cells seeded on the μDG_L, and **(c)** 13 cells seeded on the μDG_H. Axis units = μm. Black arrows denote the direction of increasing micropost stiffness. **(c-d)** Averaged cell displacements *versus* time for BAECs seeded on the: **(d)** μDG_L (*white*), and **(e)** μDG_H (*dark grey*). Y-Axis units = μm; Error bars denote s.e.m.

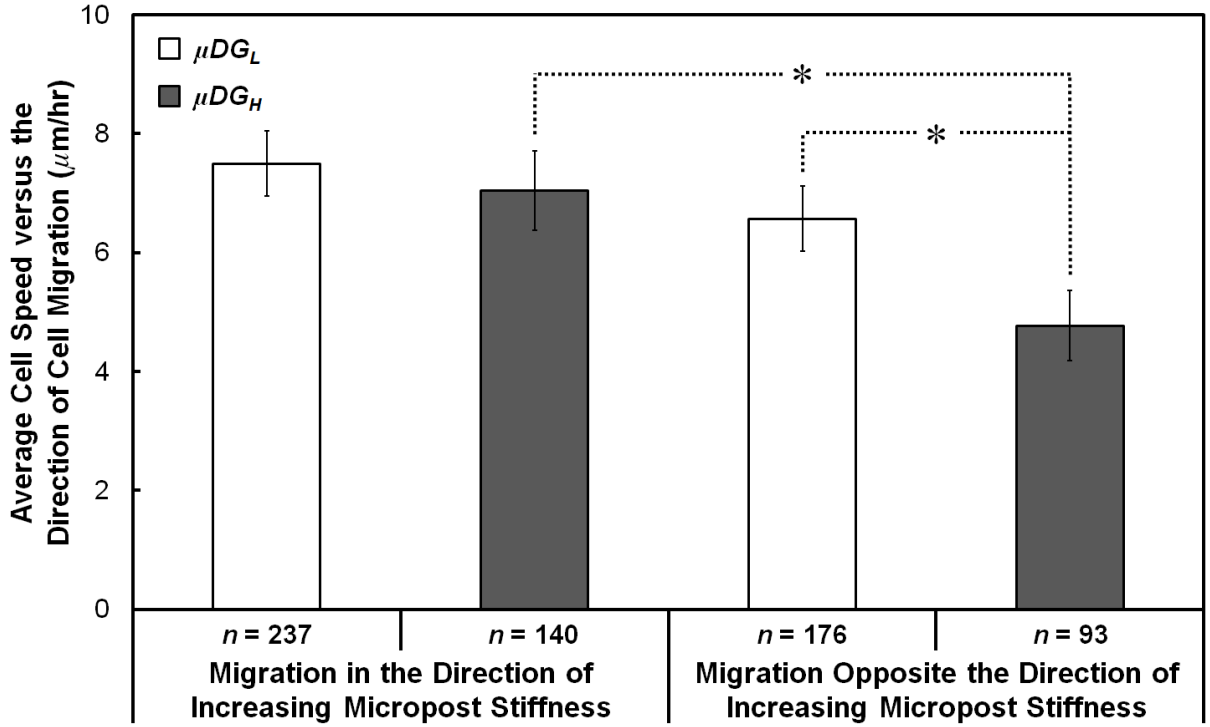

Figure 2.9 Experimental results for average BAEC velocities *versus* the direction BAEC movement on the μDG_L (*white*) and μDG_H (*dark grey*) for 18-hour studies. * denotes $p < 0.05$ statistically significant differences; Error bars denote s.e.m.; *n* denotes the number of time-steps.

On the *μDG*s, the speed of cell movement was found to vary with respect to the direction of the substrate-based stiffness cues. BAECs on both substrates were observed to exhibit higher sample mean speeds for migration in the direction of the mechanical stimuli *versus* movement opposite that direction. For cells seeded on the μDG_H, this difference was statistically significant, with BAECs migrating 46% faster in the direction of increasing micropost stiffness compared to movement opposite that direction ($p < 0.05$). Thus, not only were the proportions of displaced cells as well as the displacements of cells observed to be higher in the direction of increasing micropost stiffness, but also the speed of BAEC movement was found to be higher in that same direction. As prior work has not yet elucidated the effects of rigidity gradients on the directional speed of cell movement, these results suggest that further study is needed to examine cell speeds in response to unidirectional substrate stiffness cues.

2.4.2 Cell Motility on *μDDG*s

Experimental observations revealed that both *μDDG*s promoted unidirectional motility, as seeded BAECs migrated preferentially in the direction of increasing micropost stiffness, with limited movement perpendicular to that direction. In contrast, BAECs were observed to migrate bidirectionally on the C_E (*i.e.*, the negative control substrate with identical elliptical microposts). However, the C_C (*i.e.*, the negative control substrate with identical circular microposts) was not found to influence the direction of cell migration. **Figure 2.10** shows representative sequential time-lapse images of: (*i*) non-directional BAEC migration on the C_C (**Fig. 2.10a**), (*ii*) bidirectional migration along the axis of increased stiffness (*X-axis*) on the C_E (**Fig. 2.10b**),

and (*iii*) unidirectional migration in the direction of increasing micropost stiffness (*positive X-Axis*) on both the μDDG_L (**Fig. 2.10c**) and μDDG_H (**Fig. 2.10d**).

The two-dimensional 18-hour cell paths for migration on the C_C, C_E, μDDG_L, and μDDG_H are shown in **Figure 2.11a**, **2.11b**, **2.11c**, and **2.11d**, respectively. **Figure 2.12a-d** show radial percentage histograms of the corresponding directionality for BAEC displacement on each substrate. Additionally, a previously developed classification system[16] was employed to quantify cell directionality on each substrate (**Fig. 2.12e**). On the C_C, seeded BAECs were found to displace an average of 2.4±8.0 μm (n = 27 cells) in the negative X-axis direction by the end of the 18-hour studies (**Fig. 2.13a**). Although a larger proportion of final cell displacements was observed along the Y-axis compared to the X-axis for the C_C (**Fig. 2.12a**, **e**), the average net displacement in the X-axis direction was slightly higher than the average net displacement in the Y-axis direction (this difference was not statistically significant (p = 0.75)) (**Fig. 2.13b**). At the end of the studies, 48% (13 from a total of 27) of BAECs exhibited displacement in the positive X-axis direction relative to their initial positions at the start of the studies. These results suggest that BAEC migration on the C_C substrate was not directionally biased.

The anisotropic structure of elliptical microposts was found to promote bidirectional cell motility on the C_E; however, unidirectional biases were not observed. The 18-hour studies of BAECs seeded on the C_E revealed an average final displacement of 3.6±8.8 μm (n = 26 cells) in the negative X-axis direction (**Fig. 2.13a**). At the end of the studies, 46.2% (12 from a total of 26) of BAECs exhibited displacement in the positive X-axis direction relative to their initial positions at the start of the studies. In contrast to the C_C, a smaller proportion of final cell displacements was observed along the Y-axis compared to the stiffer X-axis for the C_E (**Fig. 2.12b**, **e**). In particular, the proportion of BAECs on the C_E exhibiting a final displacement within ±30º of the positive or negative Y-axis decreased to 27% (7 from a total of 26) compared to the C_C (**Fig. 2.12e** – *B*). The average net displacement in the X-axis direction for BAECs on the C_E was found to be significantly higher compared to the average net displacement along the Y-axis (p < 0.0005) (**Fig. 2.13b**). These results suggest that BAEC migration on the C_E was bidirectionally biased along the axis of increased stiffness.

The addition of a gradient in micropost anisotropy was found to enhance unidirectional behavior. BAECs seeded on the μDDG_L were observed to displace an average of 15.2±12.5 μm (n = 26 cells) in the direction of increasing micropost stiffness by the end of the 18-hour studies; however, this increase was not statistically discernable from the C_C (p = 0.24) or the C_E (p = 0.22) (**Fig. 2.13a**). Similar to the C_E, a smaller proportion of final cell displacements was observed along the Y-axis compared to the stiffer X-axis of increasing micropost stiffness for the μDDG_L (**Fig. 2.12c**, **e**). In addition, the proportion of BAECs on the μDDG_L exhibiting a final displacement within ±60º of the direction of increasing stiffness was 42% (11 from a total of 26) (**Fig. 2.12e** – *A*). At the end of the studies, 58% (15 from a total of 26) of BAECs exhibited displacement in the direction of increasing micropost stiffness relative to their initial positions at the start of the studies. Similar to the C_E, the average net displacement along the X-axis for BAECs on the μDDG_L was found to be significantly higher compared to the average net displacement along the Y-axis (p < 0.005) (**Fig. 2.13b**). These results indicate that the μDDG_L slightly promoted BAEC migration in the direction of increasing micropost stiffness, while simultaneously decreasing movement perpendicular to that direction.

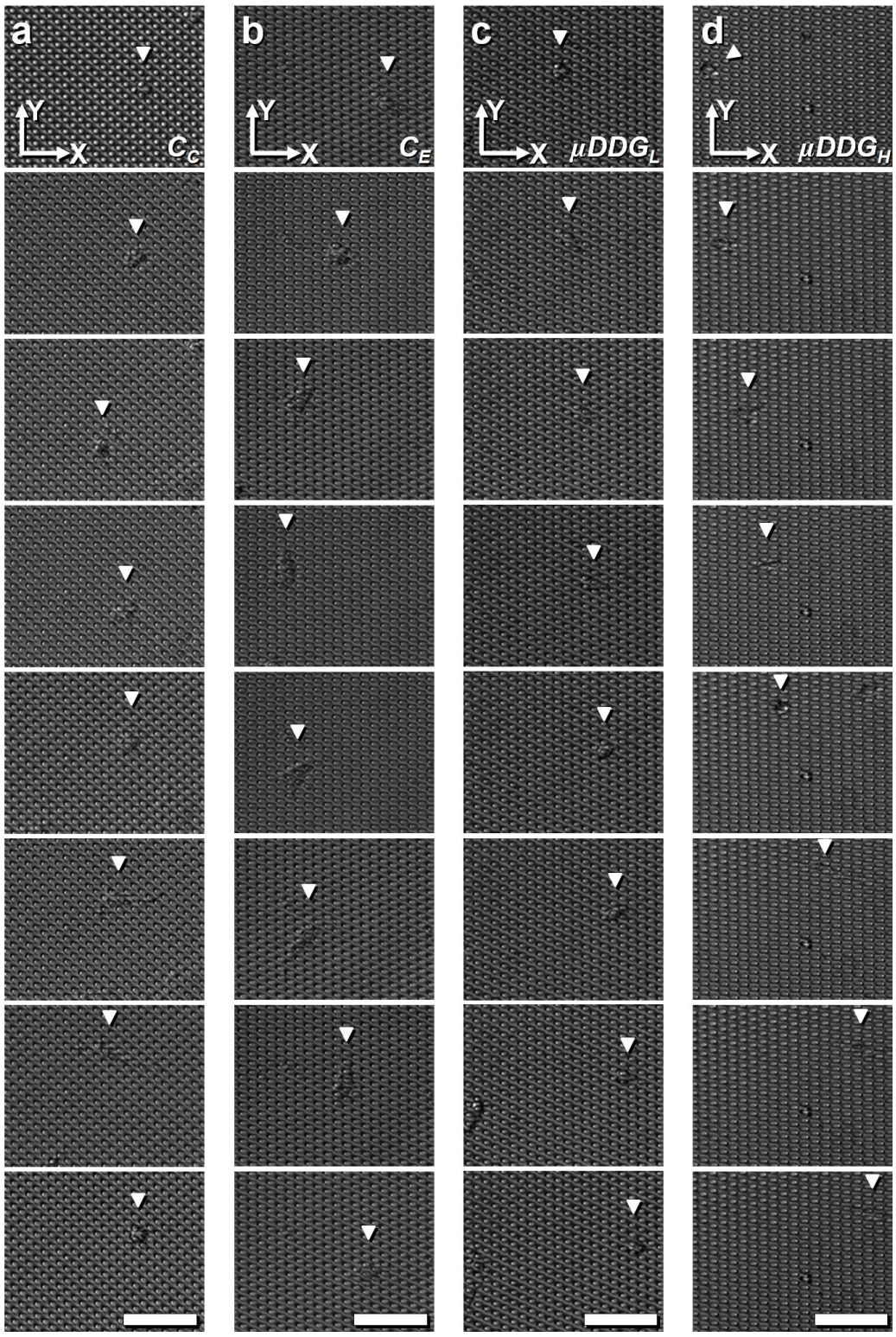

Figure 2.10 Sequential time-lapse images of BAECs (*arrow heads*) migrating on: **(a)** a negative control substrate with identical circular posts (C_C), **(b)** a bidirectional control substrate with identical elliptical microposts (C_E), and microtopographic dual-axis durotaxis gradients with **(c)** low gradient strength (μDDG_L), and **(d)** high gradient strength (μDDG_H). Scale Bars = 50 μm

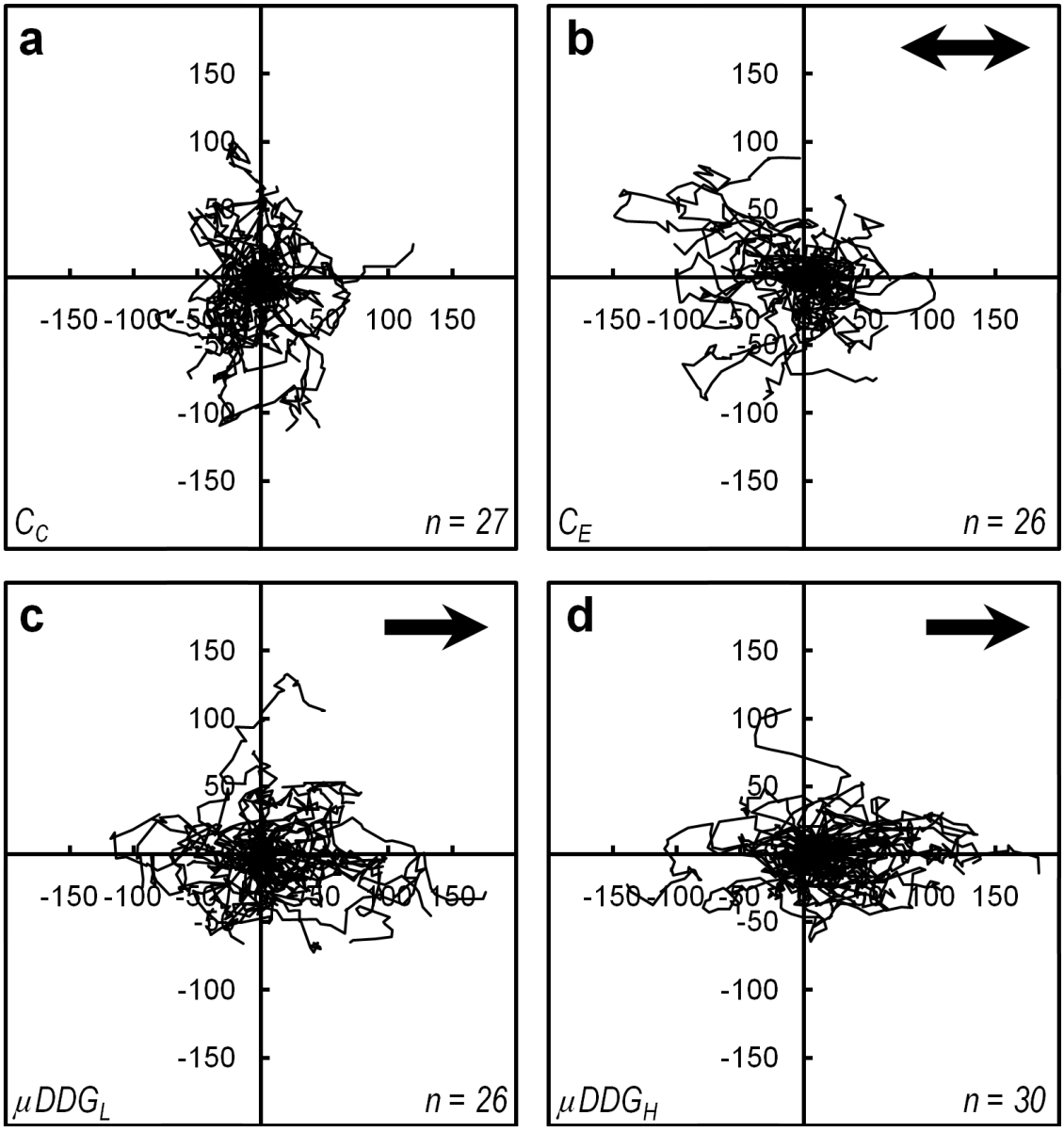

Figure 2.11 Migration paths over the course of 18-hour studies for BAECs seeded on the: **(a)** C_C, **(b)** C_E, **(c)** μDDG_L, and **(d)** μDDG_H. Axis units = μm; Black double arrow denotes the axis of increased stiffness (*i.e.*, the major axes); Black single arrows denote the direction of increasing micropost stiffness.

Although the proportion of BAECs on the μDDG_L exhibiting a final displacement within ±30º of the Y-axis decreased further to 23% (6 from a total of 26) compared to the C_E (**Fig. 2.12e** – *B*), the difference between the average X-axis and Y-axis net displacements did not increase. Despite the average total net displacement for the μDDG_L increasing slightly compared to the C_E (p = 0.055), the difference between the average X-axis and Y-axis net displacements decreased from 53.7 μm for the C_E to 41.3 μm for the μDDG_L (**Fig. 2.13b**). One potential basis for this result is that the ratio of the major axes to the minor axes (and therefore, the ratio of axial

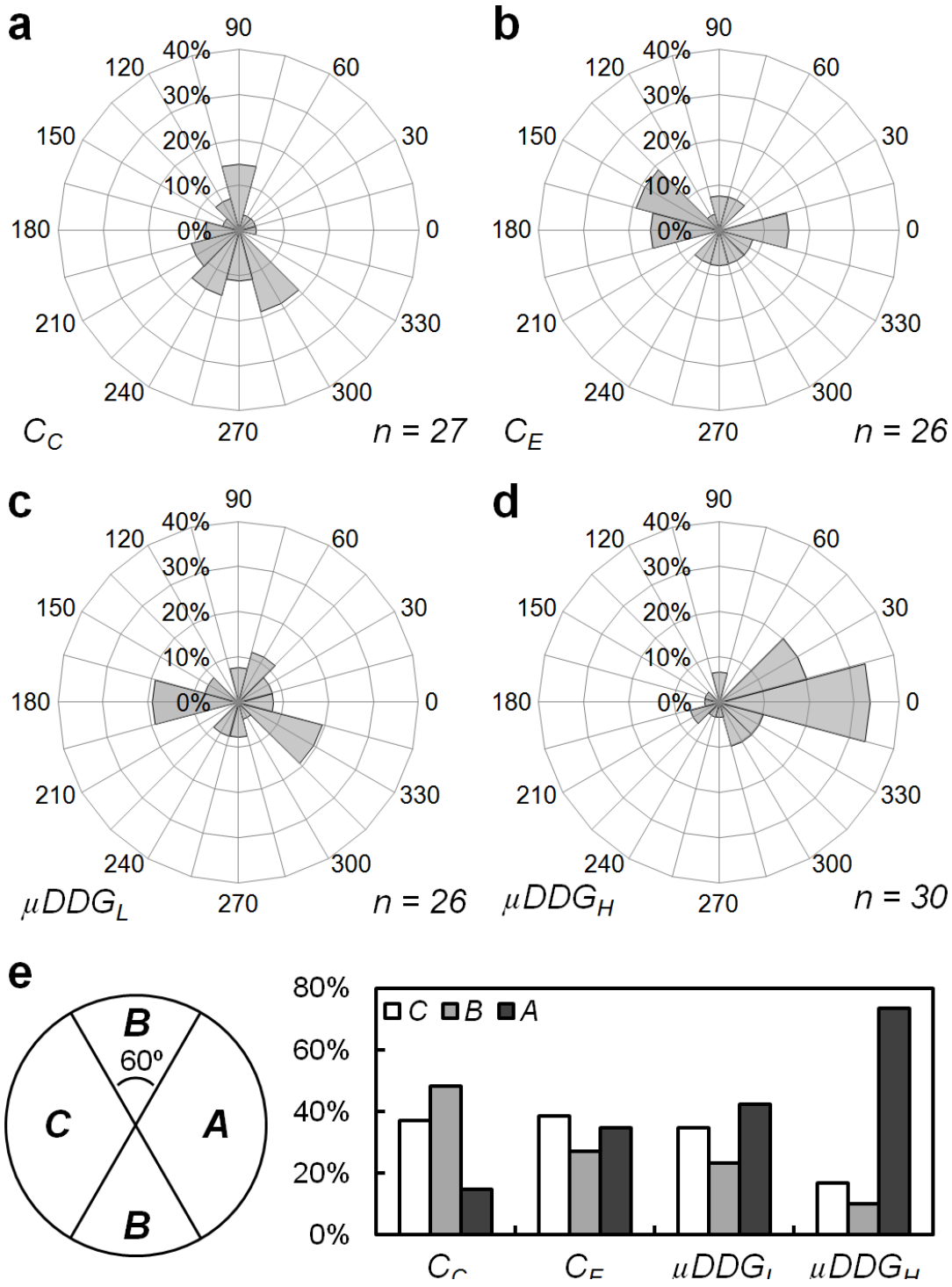

Figure 2.12 Experimental results of directional BAEC migration on the *μDDG*s and control substrates for 18-hour studies. **(a-d)** Radial percentage histograms of final displacements for cells on the: **(a)** C_C, **(b)** C_E, **(c)** μDDG_L, and **(d)** μDDG_H. Circular Axis units = Degrees; 0º denotes the positive X-axis direction (*i.e.*, the direction of increasing micropost stiffness for the *μDDG*s). **(e)** Corresponding percentage histogram of the final directional cell displacements on each microtopographic substrate into three 120º regions.

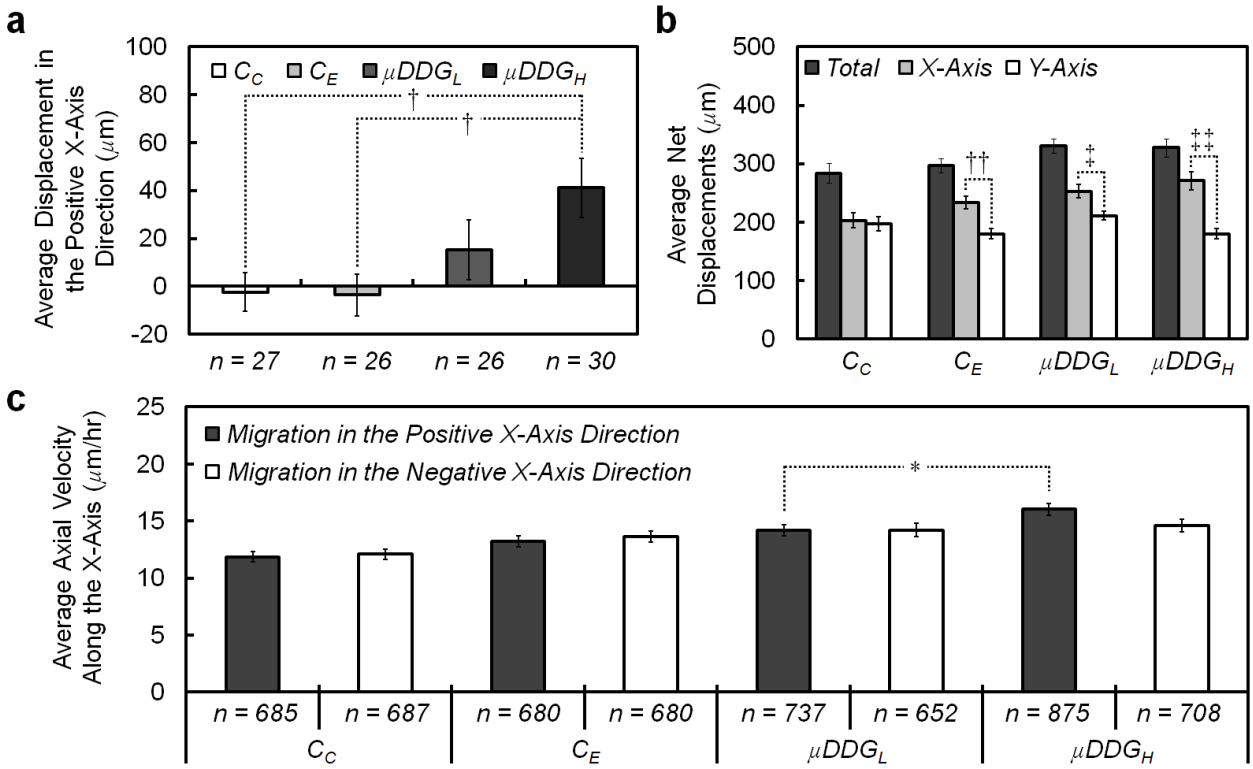

Figure 2.13 Experimental results for BAEC motility on the *μDDG*s and control substrates for 18-hour studies. **(a)** Average cell displacement in the positive X-axis direction (*i.e.*, the direction of increasing micropost stiffness for the *μDDG*s) on each substrate. **(b)** Average total (*dark grey*), X-axis (*light grey*), and Y-axis (*white*) net displacements for BAECs seeded on each substrate. **(c)** Average cell velocity along the X-axis *versus* the direction of BAEC movement on the *μDDG*s and control substrates. *, †, ‡, ††, and ‡‡ denote $p < 0.05$, $p < 0.01$, $p < 0.005$, $p < 0.0005$, and $p < 0.0001$ statistically significant differences, respectively; Error bars denote s.e.m.

stiffnesses) for the C_E was always greater than or equal to the biaxial stiffness ratios of the μDDG_L. Thus, it is likely that the relatively weaker bidirectional durotactic cues could account for the observed decrease in bidirectional control.

Higher gradient strength was found to significantly enhance the directional response. By the end of the studies, cells on the μDDG_H displaced an average of 41.1±12.3 μm (n = 30 cells) in the direction of increasing micropost stiffness (**Fig. 2.13a**). The increase in average BAEC displacement was significantly larger compared to both the C_C ($p < 0.01$) and the C_E ($p < 0.01$), but it was not statistically discernable from the μDDG_L results ($p = 0.15$) (**Fig. 2.13a**). The proportion of final cell displacements in the Y-axis direction compared to the stiffer X-axis of increasing micropost stiffness was the lowest for the μDDG_H compared to all of the substrates tested (**Fig. 2.12**). Specifically, 10% (3 from a total of 30) of BAECs exhibited a final displacement within ±30º of the positive or negative Y-axis (**Fig. 2.12e** – *B*). In contrast, the proportion of BAECs on the μDDG_H exhibiting a final displacement within ±60º of the direction of increasing micropost stiffness was 73% (22 from a total of 30) (**Fig. 2.12e** – *A*). At the end of the studies, 77% (23 from a total of 30) of BAECs exhibited displacement in the

direction of increasing micropost stiffness relative to their initial positions at the start of the studies. Similar to both the C_E and the μDDG_L, the average net displacement along the X-axis for BAECs on the μDDG_H was found to be significantly higher compared to the average net displacement along the Y-axis ($p < 0.0001$) (**Fig. 2.13b**). In addition, the average X-axis net displacement was 51% higher than the average Y-axis net displacement, which was the largest difference observed for all of the substrates tested (**Fig. 2.13b**). These results demonstrate that the μDDG_H strongly promoted unidirectional BAEC migration in the direction of increasing micropost stiffness, while simultaneously limiting movement perpendicular to that direction.

The directional speed of cell movement was found to be slightly affected by the microtopographic durotactic stimuli during the 18-hour studies. Cell velocities were examined with respect to the direction of the mechanical stimuli. For both of the control substrates, neither the number of steps nor the directional velocity varied for migration in the positive X-axis direction *versus* the negative X-axis direction ($p = 0.70$ for the C_C; $p = 0.56$ for the C_E) (**Fig. 2.13c**). On the μDDG_L, BAECs took more steps in the direction of increasing micropost stiffness *versus* opposite that direction; however, the velocity did not vary ($p = 0.97$). The increased gradient strength of the μDDG_H resulted in a higher proportion of steps in the direction of increasing micropost stiffness compared to opposite that direction. Additionally, the sample mean velocity in the direction of increasing stiffness was slightly larger than the mean velocity opposite that direction; however, this result was not quite statistically significant ($p = 0.058$) (**Fig. 2.13c**). Although the axial velocity opposite the direction of increasing stiffness did not vary significantly between the μDDG_L and μDDG_H ($p = 0.63$), the higher gradient strength of the μDDG_H was found to significantly enhance the axial migration velocity in the direction of increasing micropost stiffness ($p < 0.05$) (**Fig. 2.13c**).

The observed migratory results are consistent with past studies of the cellular response to substrate stiffness cues.[9, 10, 49, 66, 75] The bidirectional motile behavior of BAECs seeded on the C_E is consistent with durotaxis predictions and prior studies of cells seeded on substrates with elliptical microposts.[66, 75] Additionally, the limited movement perpendicular to the direction of increasing micropost stiffness on the μDDG_L and the μDDG_H is also in agreement with *a priori* durotaxis predictions and prior reports.[66, 75] However, the bidirectional experimental results for the C_E and μDDGs cannot be attributed exclusively to durotaxis. To ensure that the overall *%ECM* and topographic surface density remained constant over the length of the substrates, the spacing perpendicular to the axis of increased stiffness was always larger than the spacing parallel to the axis of increased stiffness. As a result, it is likely that the decreased spacing along the stiffer axis contributed to the observed bidirectional migratory response, similar to prior reports.[66, 75] However, compared to the μDGs in **Section 2.4.1**, the μDDGs included closer spacing between microposts perpendicular to the axis of increasing stiffness, yet the μDDGs were found to better limit cell movement perpendicular to the direction of increasing stiffness. Previously, researchers have shown that elliptical-shaped ECM islands can promote bidirectional behavior.[47] This suggests that geometric chemical factors could have also contributed to the bidirectional movement observed on the C_E and μDDGs.

Similar to prior work as well as the results in **Section 2.4.1**, higher gradient strength was found to enhance cell migration in the direction of increasing substrate stiffness.[9] Although this behavior was consistent for the displacement results, the effects of the μDDGs on cell velocities

differed from the cell speed results in **Section 2.4.1**. For cells seeded on the μDG_H, BAECs migrated 46% faster in the direction of increasing micropost stiffness compared to movement opposite that direction ($p < 0.05$) (**Fig. 2.9**). In contrast, cells on the μDDG_H migrated 10% faster in the direction of increasing micropost stiffness compared to movement opposite that direction – a result that was not statistically significant ($p = 0.058$) (**Fig. 2.13c**). Higher gradient strength was found to significantly limit cell velocities opposite the direction of increasing stiffness on the *μDG*s ($p < 0.05$), but did not enhance migration in the direction of increasing micropost stiffness (**Fig. 2.9**). Conversely, experiments with the *μDDG*s revealed to opposite behavior. Specifically, movement opposite the direction of increasing stiffness did not vary significantly between the *μDDG*s ($p = 0.63$); however, higher gradient strength was found to significantly enhance cell velocities in the direction of increasing micropost stiffness ($p < 0.05$) (**Fig. 2.13c**). One potential basis for these observed differences in cell speed behavior is due to the effects of changes in micropost-specific top surface area. In particular, the *μDG*s included increasing micropost-specific top surface area in the direction of increasing micropost stiffness, while the *μDDG*s included a constant micropost-specific top surface area over the length of the arrays. As discussed in **Section 2.4.1**, the potential chemical factors associated with varying the top surface area could have impacted the migratory results. Thus, it is likely that the migratory results for the *μDDG*s better represent the effects of microtopographic durotactic cues on the motility of seeded cells.

2.4.3 Cell Motility on *μSG*s

Experimental observations revealed that both *μSG*s promoted unidirectional motility, as seeded BAECs migrated preferentially in the direction of decreasing interpost spacing. In contrast, the *C* substrate was not found to influence the direction of cell migration. **Figure 2.14** shows sequential time-lapse images of: (*i*) non-directional BAEC migration on the *C* substrate (**Fig. 2.14a**), and (*ii*) unidirectional migration in the direction of decreasing interpost spacing (*positive X-Axis*) on both the μSG_L (**Fig. 2.14b**) and μSG_H (**Fig. 2.14c**). The two-dimensional 18-hour cell paths for migration on the *C*, μSG_L, and μSG_H are shown in **Figure 2.15a**, **2.15b**, and **2.15c**, respectively. **Figure 2.15d-f** show radial percentage histograms of the corresponding directionality for BAEC displacement on each substrate. A previously developed classification system[16] was employed to quantify cell directionality on each substrate (**Fig. 2.15g**).

On the *C* substrate, seeded BAECs were found to displace an average of 4.0±12.7 μm ($n = 25$ cells) in the negative X-axis direction by the end of the 18-hour studies (**Fig. 2.16a**). The final cell displacements were observed to be evenly distributed, without particular directionality (**Fig. 2.15d**, **g**). At the end of the studies, 36% (9 from a total of 25) of seeded BAECs had displaced within ±60º of the positive X-axis (**Fig. 2.15g – *A***), 32% (8 from a total of 25) had displaced within ±60º of the negative X-axis (**Fig. 2.15g – *C***), and 32% (8 from a total of 25) had displaced within ±30º of the positive or negative Y-axis (**Fig. 2.15g – *B***). The average net displacement in the Y-axis direction was slightly higher than the average net displacement in the X-axis direction; however, this difference was not statistically significant ($p = 0.77$) (**Fig. 2.16b**). At the end of the studies, 48% (12 from a total of 25) of BAECs exhibited displacement in the positive X-axis direction relative to their initial positions at the start of the studies. These results suggest that BAEC migration on the *C* substrate was not directionally biased.

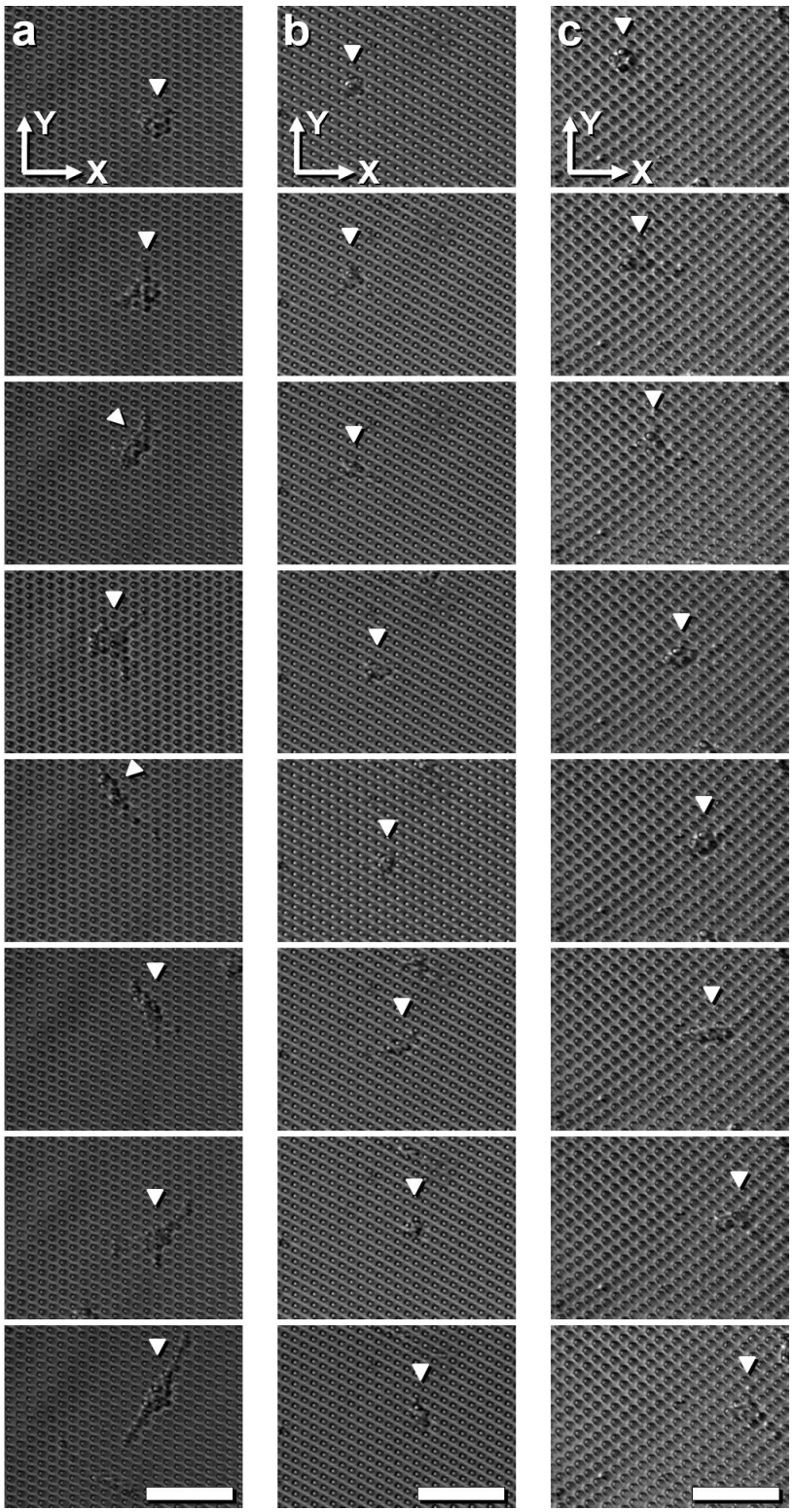

Figure 2.14 Sequential time-lapse images of BAECs (*arrow heads*) migrating on: **(a)** a control substrate with identical interpost spacing (*C*), and microtopographic spatiotaxis gradients with **(b)** low gradient strength (μSG_L), and **(c)** high gradient strength (μSG_H). The positive X-axis direction marks the direction of decreasing interpost spacing for the μSGs. Scale Bars = 50 μm

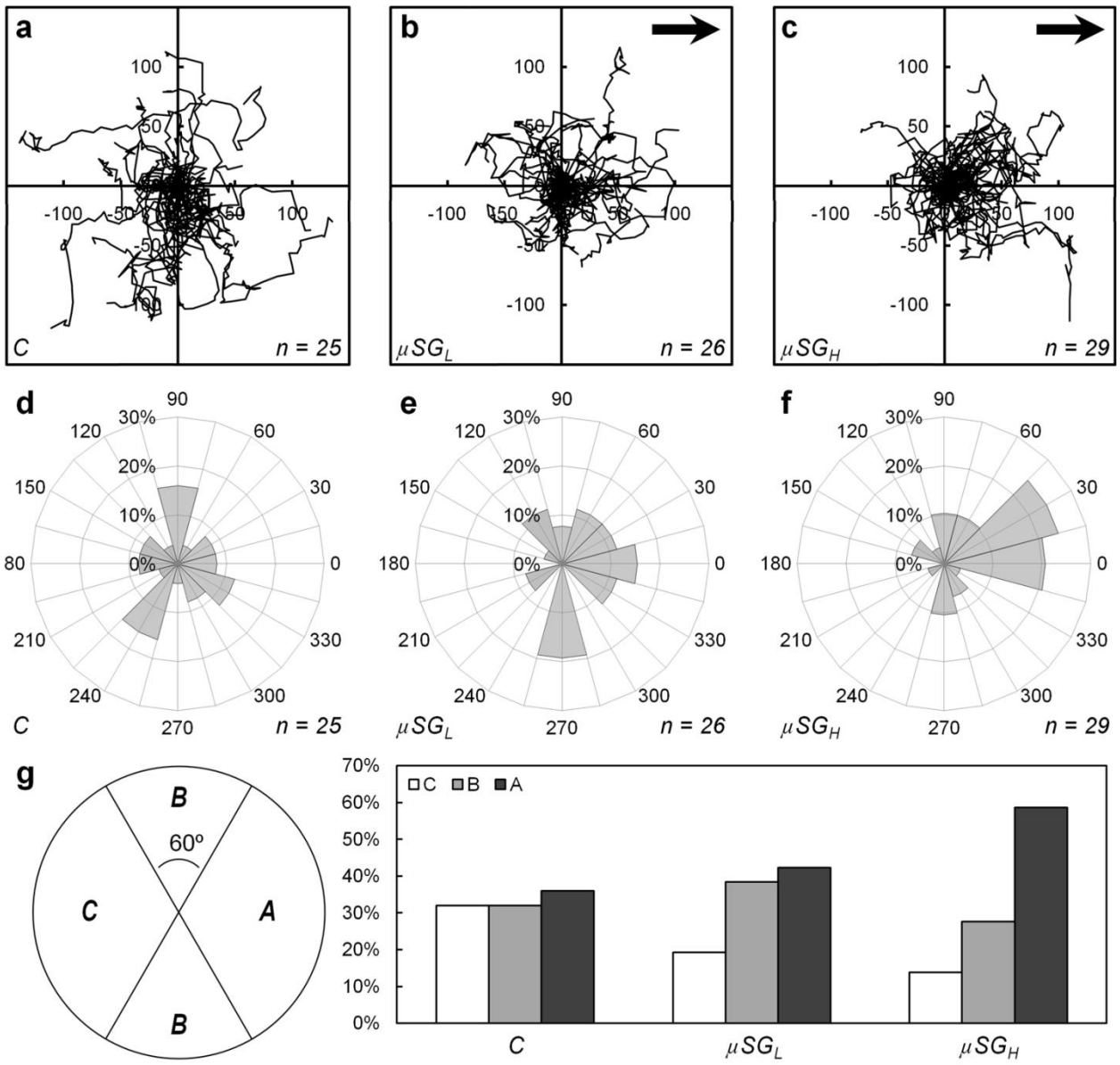

Figure 2.15 Experimental results for BAEC migration on the μSGs and control substrate for 18-hour studies. **(a-c)** Migration paths over the course of the studies for BAECs seeded on the: **(a)** *C*, **(b)** μSG_L, and **(c)** μSG_H. Axis units = μm; Black single arrows denote the direction of decreasing interpost spacing. **(d-f)** Radial percentage histograms of final displacements for cells on the: **(d)** *C*, **(e)** μSG_L, and **(f)** μSG_H. Circular Axis units = Degrees; 0º denotes the positive X-axis direction (*i.e.*, the direction of decreasing interpost spacing for the μSGs). **(g)** Corresponding percentage histogram of the final directional cell displacements on each substrate into three 120º regions.

The addition of a gradient in interpost spacing was found to enhance unidirectional behavior. BAECs seeded on the μSG_L were observed to displace an average of 13.9±7.6 μm (n = 26 cells) in the direction of decreasing interpost spacing by the end of the 18-hour studies; however, this increase was not statistically discernable from the *C* substrate (p = 0.23)

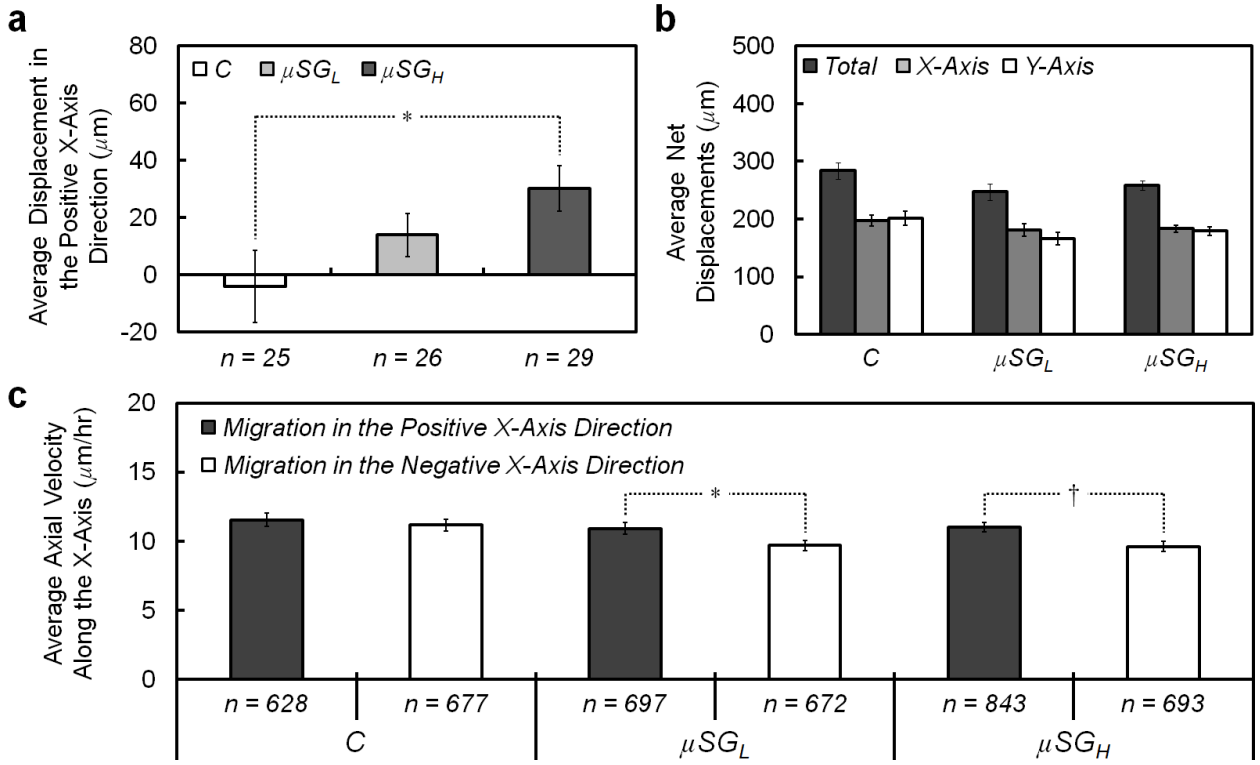

Figure 2.16 Experimental results for BAEC motility on the *μDDG*s and control substrates for 18-hour studies. **(a)** Average cell displacement in the positive X-axis direction (*i.e.*, the direction of decreasing interpost spacing for the *μSG*s) on each substrate. **(b)** Average total (*dark grey*), X-axis (*light grey*), and Y-axis (*white*) net displacements for BAECs seeded on each substrate. **(c)** Average cell velocity along the X-axis *versus* the direction of BAEC movement on the *μSG*s and control substrate. * and † denote $p < 0.05$ and $p < 0.01$ statistically significant differences, respectively; Error bars denote s.e.m.

(**Fig. 2.16a**). In contrast to the *C* substrate, a smaller proportion of final cell displacements was observed in the negative X-axis direction (*i.e.*, opposite the direction of decreasing interpost spacing) (**Fig. 2.15e**), as 19% (5 from a total of 25) had displaced within ±60º of the negative X-axis (**Fig. 2.15g** – *C*). In addition, the proportion of BAECs on the μSG_L exhibiting a final displacement within ±60º of the direction of decreasing interpost spacing increased to 42% (11 from a total of 26) (**Fig. 2.15g**). At the end of the studies, 65% (17 from a total of 26) of BAECs exhibited displacement in the direction of decreasing interpost spacing relative to their initial positions at the start of the studies. In contrast to the *C* substrate, the average net displacement along the X-axis for BAECs on the μSG_L was found to be slightly higher compared to the average net displacement along the Y-axis; however, this result was not statistically significant ($p = 0.31$) (**Fig. 2.16b**). These results indicate that the μSG_L slightly promoted BAEC migration in the direction of decreasing interpost spacing.

Higher gradient strength was found to significantly enhance the directional response. By the end of the studies, cells on the μSG_H displaced an average of 30.1±8.0 μm ($n = 29$ cells) in the direction of decreasing interpost spacing (**Fig. 2.16a**). The increase in average BAEC displacement was significantly larger compared to the *C* substrate ($p < 0.05$), but it was not statistically discernable from the μSG_L results ($p = 0.15$) (**Fig. 2.16a**). The proportions of final

cell displacements in the Y-axis direction and negative X-axis direction (*i.e.*, opposite the direction of decreasing interpost spacing) were the lowest for the μSG_H compared to all of the substrates tested (**Fig. 2.15d-g**). Specifically, 28% (8 from a total of 29) of seeded BAECs had displaced within ±30º of the Y-axis (**Fig. 2.15g – *B***), and 14% (4 from a total of 29) had displaced within ±60º of the negative X-axis (**Fig. 2.15g – *C***). At the end of the studies, 76% (22 from a total of 29) of BAECs exhibited displacement in the direction of decreasing interpost spacing relative to their initial positions at the start of the studies. Similar to the μSG_L, the average net displacement along the X-axis for BAECs on the μSG_H was found to be slightly higher compared to the average net displacement along the Y-axis, but not statistically significant ($p = 0.71$) (**Fig. 2.16b**). These results demonstrate that the μSG_H strongly promoted unidirectional BAEC migration in the direction of decreasing interpost spacing.

The microtopographic spatial stimuli were found to significantly affect the directional speed of cell movement during the 18-hour studies. Cell velocities were examined with respect to the direction of the spatial cues. For the *C* substrate, although the number of steps in the positive X-axis direction was lower compared to the number of steps opposite that direction, the mean axial velocity in the positive X-axis direction was slightly higher, but not significantly ($p = 0.53$) (**Fig. 2.16c**). On the μSG_L, BAECs took a higher number of steps in the direction of decreasing interpost spacing *versus* opposite that direction, and migrated faster in the direction of decreasing interpost spacing ($p < 0.05$) (**Fig. 2.16c**). Higher gradient strength further enhanced this response as BAECs on the μSG_H migrated 15% faster during movement in the direction of decreasing interpost spacing, while also taking 22% more steps in the direction of decreasing interpost spacing *versus* opposite that direction (**Fig. 2.16c**). Thus, not only did BAECs on the μSGs migrate more often in the direction of decreasing interpost spacing, they also exhibited higher cell velocities in that same direction.

At present, the specific mechanisms underlying the spatiotaxis migratory response remain unclear. One potential basis for this behavior is that variable interpost spacing may impact the location where the leading cellular protrusion stabilizes. During cell movement, the migration direction is dictated by the establishment of a single, dominant protrusion anchored to the substratum; however, protrusive activity is a stochastic and dynamic process.[77] Thus, differences in interpost spacing could result in a higher probability of motile cells first contacting and forming adhesions onto comparatively closer microposts. As a result, cellular protrusions could more readily stabilize in the direction of decreasing interpost spacing, thereby influencing the direction of migration. Spatiotactic behavior could also be attributed to intracellular energy optimization. Protrusive activity is an energy intensive process, and the length of cellular protrusions is related to the polymerization of actin monomers, which are transported to the leading edge of protrusive sites.[44, 78] Thus, generating shorter leading protrusions would reduce the energy needed for actin transport and polymerization, thereby rendering anchorage and migration to closer microfeatures energetically favorable. These potential mechanisms underlying the spatiotaxis phenomenon could also contribute to the bidirectional movement cells exhibit on microgrooved substrates.[27, 69]

2.4.4 Cell Motility on the *μDSG*s

Experimental observations revealed that changes in micropost spacing significantly affected the mechanical response of seeded BAECs. In contrast to the experimental results for BAECs seeded on the μDG_L in **Section 2.4.1**, the addition of variable interpost spacing was found to significantly offset the durotactic response ($p < 0.05$). For example, **Fig. 2.17a** shows sequential time-lapse images of a BAEC (*white arrows*) migrating in the direction of decreasing interpost spacing (*black arrow*), opposite the direction of increasing micropost stiffness. The two-dimensional 18-hour cell paths for 38 BAECs seeded on the *μDSG* are shown in **Fig. 2.17b**. Although cells were observed to migrate throughout the course of the experiments (**Fig. 2.17c**), directional biases were not observed initially (**Fig. 2.17d**). However, by the end of the studies, seeded BAECs were found to displace an average of 9.6±7.3 μm in the direction of decreasing interpost spacing (**Fig. 2.17d**). The maximum observed displacements during the studies were 149 μm for cell movement in the direction of decreasing interpost spacing, and 115 μm for displacement opposite that direction. In contrast, lateral migration did not appear to be biased, as BAECs exhibited a final average displacement of 4.2±11.5 μm perpendicular to the axis of decreasing interpost spacing (**Fig. 2.17e**). At the end of the studies, 61% (23 from a total of 38) of BAECs exhibited displacement in the direction of decreasing interpost spacing relative to their initial positions at the start of the study.

The speed of cell movement was also found to be influenced by variable micropost spacing. In **Section 2.4.1**, cells seeded on the μDG_L (with only mechanical cues) exhibited average speeds of 7.5±0.5 μm/hr for movement in the direction of increasing stiffness, and 6.6±0.5 μm/hr during migration opposite that direction. The addition of variable interpost spacing appeared to reverse this trend. During the 18-hour cell studies, the average speed of BAEC migration was 5.42±0.36 μm/hr for movement in the direction of decreasing interpost spacing. In contrast, for migration opposite that direction, BAECs exhibited an average speed of 4.67±0.31 μm/hr; however, this difference was not statistically significant ($p = 0.12$).

The experimental results suggest that changes in micropost spacing can limit and even counteract the effects of microtopographic mechanical stimuli. Although the spatial stimuli appeared to be the dominant migratory cue overall, there remained periods where migration was observed opposite the direction of decreasing spacing (**Fig. 2.17d**). It is possible that this behavior was due to the opposing mechanical stimuli. Increasingly the post-to-post spacing increment could further enhance the effects of the spatial cues; however, further study is needed to elucidate the effects of spacing gradient strength on the mechanical migratory response.

On the *μDSG*, BAECs were observed to migrate in the direction of decreasing interpost spacing, rather than in the direction of the mechanical cues (*i.e.*, in the direction of increasing micropost stiffness). At present, the specific mechanisms underlying this migratory response remain unclear; however, the effects of the different migratory cues on cell motility could be related to the order of locomotive processes. The basis for controlling cellular movement on each microtopographic gradient can be attributed to the capability of manipulating distinct steps of the locomotive process, with the *μSG*s and *μDG*s influencing membrane extension and substrate adhesion, respectively. As discussed in **Section 2.4.3**, one potential basis for spatiotactic behavior is the effect of variable spacing on the location where the leading protrusion

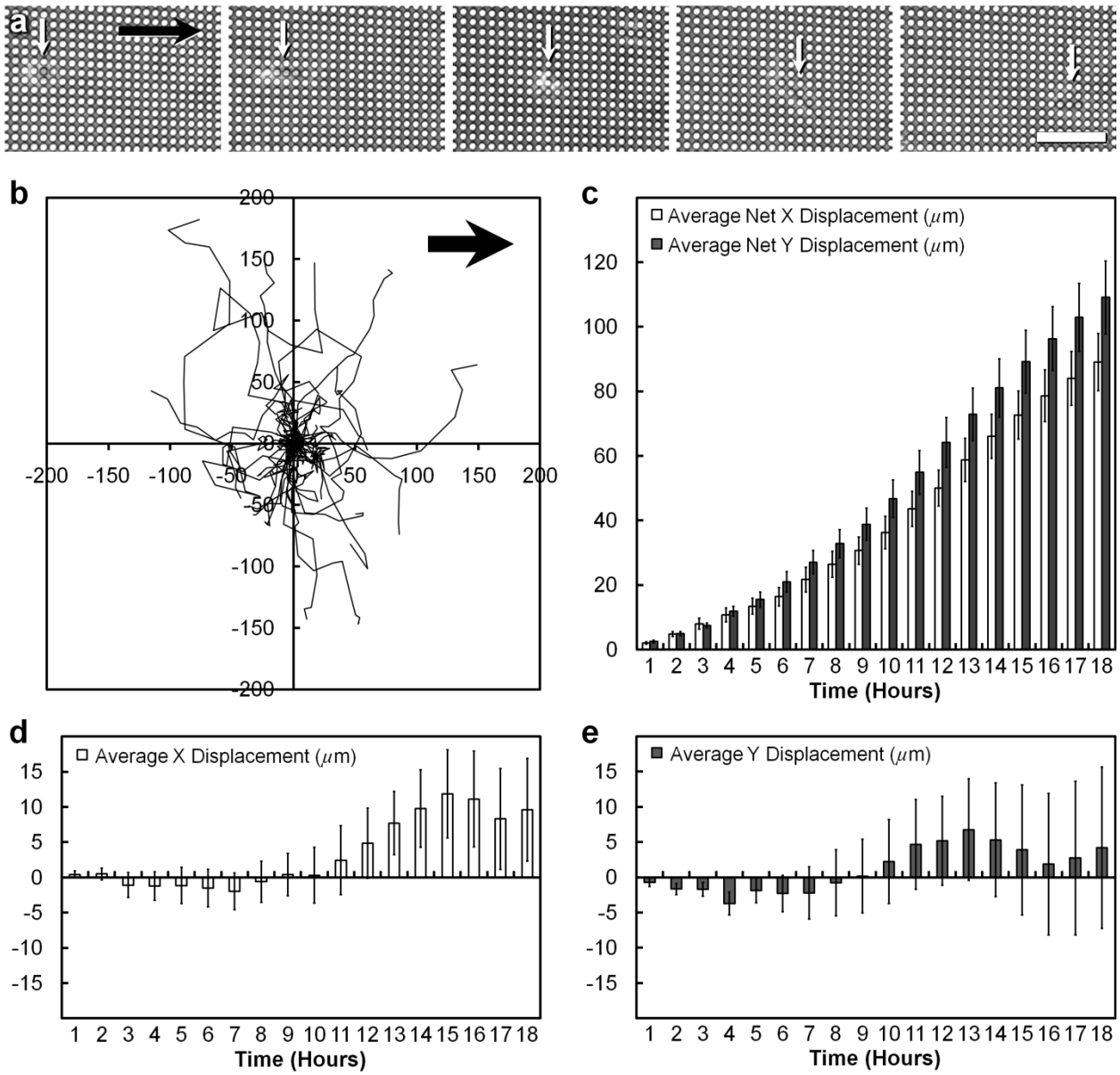

Figure 2.17 Experimental results of BAEC migration on the *μDSG* for 18-hour studies. **(a)** Sequential time-lapse images of a BAEC (*white arrows*) migrating in the direction of decreasing interpost spacing (*black arrow*) on the *μDSG*, opposite the direction of increasing micropost stiffness. Scale Bar = 50 *μ*m. **(b)** Two-dimensional cell paths for 38 cells seeded on the *μDSG*. Axis units = *μ*m; Black arrow denotes the direction of decreasing interpost spacing. **(c)** Averaged net cell displacements *versus* time in the direction of decreasing interpost spacing (*white*) and perpendicular to the direction of decreasing interpost spacing (*dark grey*). **(d)** Averaged cell displacements *versus* time in the direction of decreasing interpost spacing. **(e)** Averaged cell displacements *versus* time perpendicular to the direction of decreasing interpost spacing. Error bars denote s.e.m.

stabilizes. Specifically, because protrusive activity is a stochastic and dynamic process, it is likely that cells on *μSG*s will first contact and form adhesions onto comparatively closer

microposts. On the *μDG*s, relatively stronger adhesive contacts can be formed on stiffer microposts compared to softer microposts.[14] This behavior would enhance cellular attachment to stiffer microposts while simultaneously facilitating detachment from softer microposts, and could account for the observed migration in the direction of increasing micropost stiffness in **Section 2.4.1** and **Section 2.4.2**. On the *μDSG*, because relatively longer protrusions are required for cells to reach microposts in the direction of increasing micropost stiffness, the formation of new adhesive contacts on stiffer microposts is limited initially (*i.e.*, until after membrane extension has occurred). Such factors could provide an explanation as to why the spatial cues dominated the durotactic response on the *μDSG*. Although the overall *%ECM* was held constant throughout the *μDSG*, one caveat to the experimental results is that the micropost-specific top surface area increased from post-to-post as the radii were increased. As discussed in **Section 2.4.1**, this would increase the potential for chemical (*i.e.*, haptotactic) cues to promote migration in the direction of increasing micropost stiffness. Thus, if such cues did affect BAEC migration, the spatiotactic response would in fact be more robust than observed.

Chapter 3: Arrayed Microposts for Microparticle Handling in Microfluidic Systems

3.1 Introduction

3.1.1 Particulate-Handling in Microfluidic Systems

Microfluidic particulate-based microarrays offer an ideal platform for chemical and biological applications, including quantitative cell biology, cellular investigations, medical diagnostics, drug screening, and molecular detection; thus, precision hydrodynamic controls of microparticles (*e.g.*, cells and microbeads) are in critical demand.[1, 79] System miniaturization results in a variety of benefits, including high surface-to-volume ratios, low reagent volumes, and rapid diffusion times. As a result, there has been significant development of dynamic microarrays, which are characterized by the loading of microparticle suspensions into microfluidic systems.[80-83] To benefit from the advantages of dynamic microarray platforms, researchers have utilized diverse techniques to: (*i*) transport, immobilize, and array both living cells and microbeads in microfluidic systems, (*ii*) mix microparticles with multiple fluidic reagents and washes, and (*iii*) release cells and microbeads from microarrays.[30-37, 40-43, 80-85] Through improved microparticle handling, multiplexed reactions could be implemented in microfluidic platforms to increase throughput for particulate-based microarrays.[86-88] Hydrodynamic methods, which enable the transportation and immobilization of high numbers of suspended microparticles *via* passive fluidic forces, are ideally suited for handling cells and microbeads in microfluidic systems.[38, 81]

3.1.2 Arraying Microparticles *via* Hydrodynamic Techniques

Previously, researchers have developed a variety of hydrodynamic methods for arraying microparticles in designated trapping locations. In particular, microwell arrays, which involve loading microparticle suspensions and allowing the particles to settle into microfabricated wells, have been widely used to array cells[30-33] and microbeads.[89, 90] Di Carlo *et al*. designed pachinko-style elevated U-shaped weir structures to array living cells[34, 35] – a technique that has been adapted to corral cells[40, 41] and for cellular pairing applications.[36]

In contrast to the aforementioned two-layer techniques, researchers have also developed single-layer hydrodynamic arraying methods that bypass the limitations (*e.g.*, time and labor) associated with multi-layer microfabrication processes. For example, Tan and Takeuchi presented a microfluidic system consisting of trapping channels that cross a meander-shaped main channel to array microbeads[81] and hydrogel-encapsulated cells.[37] In this system, a lower fluidic resistance through a vacant trap results in particle trapping. After a microparticle is trapped, the resistance across the trap increases, which causes subsequent particles to bypass occupied trapping sites.[81] This technique has also been adapted to achieve long-term trapping of single cells,[91] and for pairing of both microbeads[92] and cells.[39, 93]

3.1.3 Multi-Stage Fluidic Reactions and Analyses in Particulate-Based Microarrays

Previously, particulate-based assays have been developed to achieve microfluidic mixing and visualization with either mobile or non-mobile microparticles. For mobile (*i.e.*, dynamic) particulate-based microarrays, microparticles suspended in solution undergo microfluidic mixing with reagents and are then visualized dynamically (*e.g.*, *via* flow cytometry) for detection.[87, 94] In such systems, the microparticles are never immobilized during the fluidic reaction process. In contrast, non-mobile (*i.e.*, fixed) particulate-based arrays consist of cells or microbeads that are first immobilized in microfluidic systems (*e.g.*, using microwells or weir structures), and then fluidic reagents are delivered to the non-mobile particles.[1, 33-35, 95-99] The efficacy of dynamic particulate-based microarrays could be further extended by incorporating these two techniques into a single system capable of achieving: (*i*) dynamic mixing of mobile microparticles with distinct reagents, and then (*ii*) microparticle immobilization for visualization and signal detection. By integrating controlled microfluidic mixing of suspended microparticles with hydrodynamic particulate arraying techniques, such microfluidic platforms could offer a low-cost alternative to more complex flow cytometry-based methods, for applications including point-of-care (POC) diagnostics and on-site bio-chemical analysis.[100, 101]

3.1.4 Releasing Arrayed Microparticles in Microfluidic Systems

Historically, researchers have focused primarily on arraying microparticles (*e.g.*, cells and microbeads) in microfluidic systems.[30-35] Recently however, research has shifted toward enabling full microarray resettability after particle trapping.[42, 43, 102] Resettable microfluidic systems can significantly reduce limitations associated with one-time-use devices, particularly in terms of the cost, time, and labor required to fabricate a new device for each particulate-based experiment.[43] Additionally, fully resettable microarrays enable the rapid retrieval of high numbers of microparticles, which can then be used for analysis or in subsequent experiments.[42]

An ideal resettable dynamic microarray architecture would facilitate: (*i*) the release of all arrayed microparticles, (*ii*) high trapping efficiencies and yields, (*iii*) high trapping densities of individual particles (*i.e.*, without particle-particle contact), and (*iv*) simplified processes associated with device fabrication and operation. Despite considerable progress, simultaneously achieving these goals has remained a significant challenge. Previously, researchers have implemented a variety of techniques to achieve microarray resettability. To release microparticles from the Tan and Takeuchi trapping system during forward flow rates, microbubbles generated *via* laser-induced heating of aluminum plates have been used to displace cells[37] and microbeads[81] from trapping positions. This technique is advantageous for releasing individual microparticles of interest; however, thermal bubble generation is inefficient for resetting an entire microarray (*i.e.*, with hundreds of arrayed microparticles). Thus, researchers in the Takeuchi group have further adapted the Tan and Takeuchi trapping system (*see* **Section 3.1.2**) to enable full microarray resettability during reverse (alternatively, backward) flow.[42, 102] By using microfeature-based obstacles, Iwai *et al*. varied experimental parameters to demonstrate bead-based systems with: (*i*) a 93% trapping rate and an 85% releasing rate, and (*ii*) a 100% trapping rate and a 77% releasing rate. Additionally, the system facilitated an approximate trapping density of 100 microbeads (15 μm in diameter) in a 0.75 mm^2 area.[42]

Pneumatic valves have also been used to control microparticle trapping and releasing in microfluidic systems.[43, 102] In particular, Fu *et al.* developed a pneumatic valve-based microarray to trap and release microbeads; however, neither microbead trapping without bead-bead contact nor full microarray resettability were demonstrated with this system.[43] At present, achieving full resettability for microarrays with suspended cells has remained a significant challenge.

3.1.5 Cell Handling *versus* Microbead Handling in Dynamic Microarrays

Previously, dynamic microarray platforms have been employed for both cells and microbeads;[84] however, there are a number of differences between handling suspended cells and microbeads in microfluidic systems. Living cells are significantly more polydisperse compared to microbeads, particularly in terms of particle size and shape. After being transported and arrayed in designated trapping positions, motile cells can independently migrate from the trapping sites. If the experimental conditions (*e.g.*, temperature, fluidic shear stress) are not regulated properly, cell death can occur in the microfluidic system.[91, 103] Additionally, releasing cells from dynamic microarrays has proven difficult because cells can form strong attachments to surfaces surrounding trapping sites. Historically, such issues have led researchers to primarily focus on demonstrating and characterizing dynamic microarrays with microbead suspensions first (*i.e.*, prior to using cell suspensions), which bypass the aforementioned limitations.[81, 92] Thereafter, the dynamic microarrays have been adapted for use with cell suspensions.[37, 39, 91] For example, the Tan and Takeuchi system (*see* **Section 3.1.2**) was first demonstrated using microbeads,[81] then hydrogel-encapsulated cells,[37] and lastly with living cells.[91] Thus, the demonstration of microbead handling in dynamic microarrays represents a critical first step toward developing microfluidic platforms for handling suspended cells.

3.2 Design of Microfluidic Systems for Microparticle Handling

3.2.1 Resettable Micropost Array Trapping (μPAT)

To improve microparticle handling in microfluidic systems, a hydrodynamic resettable micropost array trapping (μPAT) methodology was developed. **Figure 3.1** shows conceptual illustrations of the resettable μPAT process. The μPAT technique consists of arrayed rectangular microposts that produce parallel flow channels to promote or prevent microparticle immobilization based on the flow polarity. By altering two fundamental geometric dimensions – the trapping width (W_T) and the resetting width (W_R) (**Fig. 3.1a**) – both the trapping mode and the resetting mode can be tuned, respectively.

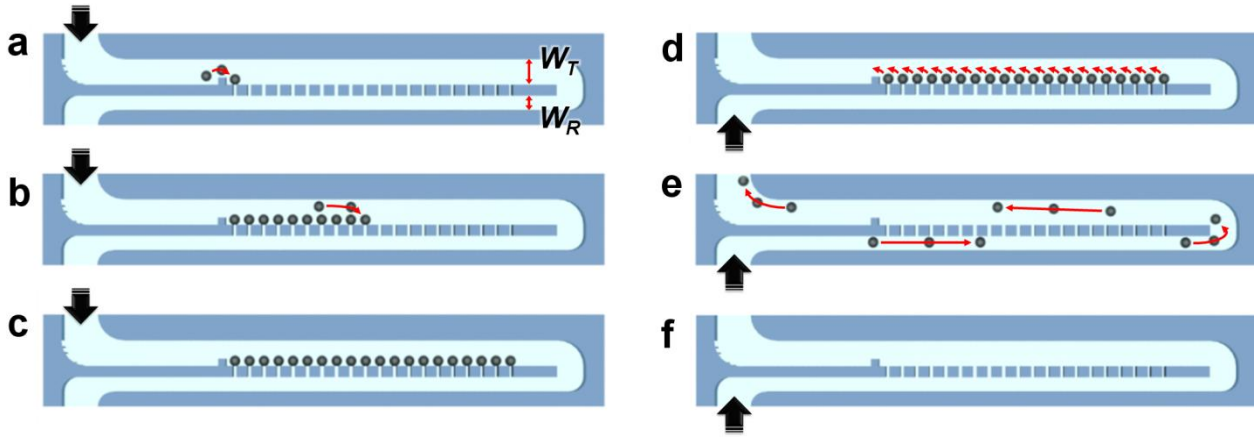

Figure 3.1 Conceptual illustrations of the resettable micropost array trapping (μPAT) process. The trapping width (W_T) and resetting width (W_R) can be adjusted to tune the trapping mode and resetting mode, respectively. **(a-c)** Resettable μPAT trapping mode. Under positive fluidic flow, microparticles immobilize in the designated trapping sites between microposts. **(d-f)** Resettable μPAT resetting mode. When the flow polarity is reversed, microparticles release from the trapping sites to reset the array.

Under positive fluidic flow, suspended microparticles immobilize in the designated trapping sites between microposts (**Fig. 3.1a**). When microparticles immobilize at each trapping location, fluid flow is diverted from the occupied trap to the remaining vacant trapping sites. This facilitates the transport and immobilization of subsequent microparticles in the remaining vacant traps (**Fig. 3.1b**). After particles are immobilized in all of the trapping sites (**Fig. 3.1c**), additional microparticles are directed to the next μPAT system in series or to an outlet port.

By reversing the flow polarity, microarray resettability can be achieved. Under negative fluidic flow, the microparticles are initially released from the trapping sites (**Fig. 3.1d**). For device configurations where several μPAT systems are arrayed in series, microparticles can be transported to the backs of the trapping sites. In these cases, W_R is tuned to prevent particles from re-arraying at the backs of the trapping sites (**Fig. 3.1e**). By directing microparticles to an outlet port, the arrays can be reset (**Fig. 3.1f**). Thereafter, the microparticles can be retrieved (*e.g.*, for observation or for use in subsequent experiments). The microarray can also be used to

perform additional experiments with new sets of microbeads or cells, thereby enabling the use of a single microdevice for multiple particulate-based experiments.

3.2.2 A Dynamic Microarray with *μ*PAT for Parallel DNA Detection

To demonstrate a dynamic particulate-based microarray that integrates both microfluidic mixing of mobile (*i.e.*, suspended) particles and hydrodynamic microparticle arraying capabilities on a single chip, a microfluidic system was designed for simultaneously detecting multiple bio-molecules in parallel using microbeads. Specifically, the system was developed to detect single nucleotide polymorphisms (SNPs) for single-stranded DNA (ssDNA) oligonucleotide sequences *via* molecular beacon probes (MBs) conjugated to polystyrene microbead substrates.

The advancement of microfluidic platforms for surface-based biochemical assays impacts a broad range of biomedical fields, including genomics, proteomics, drug discovery, and molecular diagnostics.[82, 104] Bead-based microfluidic platforms have attracted significant attention in recent years due to their enhanced reaction kinetics, reduced background noise, and decreased system costs.[80-84, 87, 88] Additionally, microbeads can be functionalized with a variety of chemicals and bio-molecules to achieve diverse chemical and biological assays (*e.g.*, immunoassays[105]). Previously, MBs have been employed as a detection mechanism for target bio-molecules, such as cytokines[106] and SNPs.[107] The MBs used for this study are ssDNA sequences containing a stem-and-loop structure, with a fluorophore and a quencher molecule on opposing ends. In the absence of a loop-complementary target DNA oligonucleotide sequence, the MBs maintain their stem-and-loop structure, which restricts fluorescence *via* a Förster Resonance Energy Transfer (FRET) interaction between the fluorophore and quencher molecules.[108-111] In the presence of a loop-complementary target sequence, the loop region of the MB hybridizes with the DNA oligonucleotide, which dissociates the stem structure. This conformational change positions the fluorophore and quencher molecules at a distance where FRET is no longer possible, enabling the fluorophore to fluoresce when excited.[108-111] The fluorescence response is reduced as the number of base-pair mismatches increases, thereby enabling the detection of SNPs for unlabeled DNA analytes.[107]

Conceptual illustrations of the dynamic microarray architecture and reaction processes are shown in **Figure 3.2**. MB-based genotyping is combined with hydrodynamic microbead arraying to simultaneously detect multiple ssDNA oligonucleotide sequences in parallel. A suspension of polystyrene microbeads conjugated to an extended streptavidin-based linker and a solution of biotinylated MBs are loaded separately (**Fig. 3.2**). Laminar diffusion-based mixing in the microfluidic channel enables MBs to bind to the surface of the microbead substrates and maintain a conformation with quenched fluorescence. *Via* separate inlets, four distinct homogenous solutions are loaded: (*i*) *Perfect Match* (PM) – the target DNA oligonucleotide sequence, which is perfectly complementary to the MB, (*ii*) *One Mismatch* (SNP) – a DNA oligonucleotide sequence with a single base-pair mismatch to the MB, (*iii*) *Mismatch* (MM) – a DNA oligonucleotide sequence with multiple base-pair mismatches, and (*iv*) *Blank* – a negative control solution of PBS (**Table 3.1**).[87, 112] The MB-microbead solution is distributed to four microchannels, each mixing independently with a singular DNA or PBS solution (**Fig. 3.2**). When the MB-microbead solution is mixed with the PM solution, the complementary target

DNA oligonucleotide sequences hybridize with the MBs, resulting in a detectable fluorescence on the surface of each microbead. After the MB-microbead solution is mixed with the SNP solution, the fluorescence response of the MBs is reduced due to the single base-pair mismatch. For the MM solution, the fluorescence response is further reduced due to the high number of base-pair mismatches between the analyte DNA and the MB. The Blank solution provides a baseline reference value for the auto-fluorescence of the MBs on the microbead surface. To analyze the fluorescence response of the MBs corresponding to each solution, the microbeads are ultimately immobilized *via* a non-resettable version of the μPAT system discussed in **Section 3.2.1**, thereby precluding the need for flow cytometry equipment.[97, 113, 114]

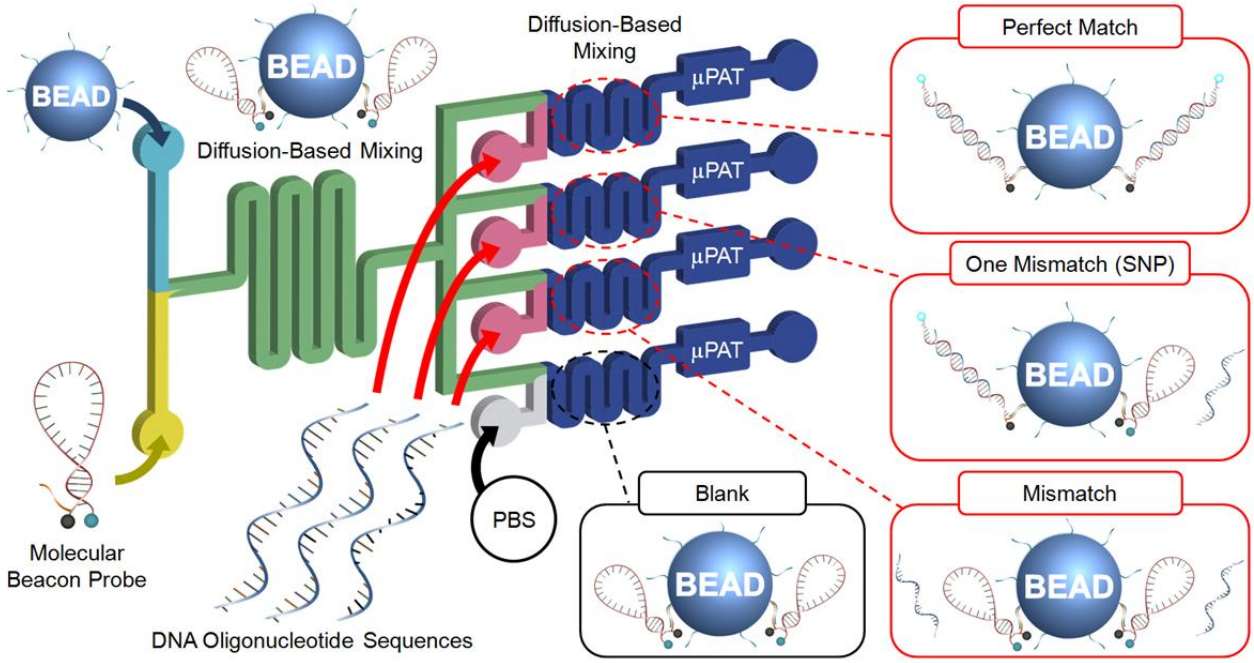

Figure 3.2 Conceptual illustrations of the dynamic particulate-based microarray for parallel DNA detection. Diffusion-based mixing in the microfluidic channel enables the immobilization of molecular beacon probes (MBs) onto the microbead substrates. Three distinct DNA oligonucleotide sequences and PBS are inputted *via* separate inlets, each mixing independently with the MB-microbead solution. Hybridization occurs corresponding to the degree of matching between the MB and the DNA analytes, resulting in varying overall levels of fluorescence. After mixing, the microbeads are immobilized for fluorescence detection *via* a non-resettable version of micropost array trapping (μPAT) (*see* **Section 3.2.1**).

Table 3.1 Names and sequences of the molecular beacon probe (MB) and DNA oligonucleotide sequences based on the Hepatitis C viral (HCV) genome.[112]

Name	**Sequence**
Molecular Beacon (MB)	5'-6-FAM-GCGAGC-CACCGGAATTGCCAGGACGACC-GCTCGC-BHQ-1-3'
Perfect Match (PM)	3'-GTGGCCTTAACGGTCCTGCTGG-5'
One Mismatch (SNP)	3'-GTGGCCTTAACGG**G**CCTGCTGG-5'
Mismatch (MM)	3'-GAGGGGCGGCGACTGGTGAG-5'

3.2.3 'Microfluidic Ping Pong' (MPP) for Multi-Stage Fluidic Reactions Under Discontinuous Flow Conditions

Although the dynamic microarray presented in **Section 3.2.2** was designed to provide advantages compared to static microarrays (*e.g.*, enhanced diffusion times, the ability to 'mix-and-match' microparticles corresponding to different screenings, *etc.*), the microfluidic platform included several limitations inherent to the system's design. For example, ensuring complete diffusion-based mixing of reagents corresponding to each reaction-step necessitates significant device area. By mixing all of the experimental reagents with the suspended microbeads prior to bead-immobilization, there is a high likelihood that undesired solution-phase binding will occur, which can decrease assay sensitivity and increase background noise. Additionally, the design precluded the ability to implement fluidic washes between reaction-steps. Because bead-immobilization occurs after reaction completion, optical visualization and fluorescence detection is restricted to only the final step of multi-stage reaction processes. Such issues are prevalent among current dynamic bead-based microarrays that preclude the need for flow cytometry or magnetic microbeads. As a result, the use of microfluidic bead-based platforms for achieving multi-stage reaction processes (*e.g.*, sandwich assays) remains limited. To overcome the aforementioned limitations, a novel dynamic bead-based microarray platform was designed.

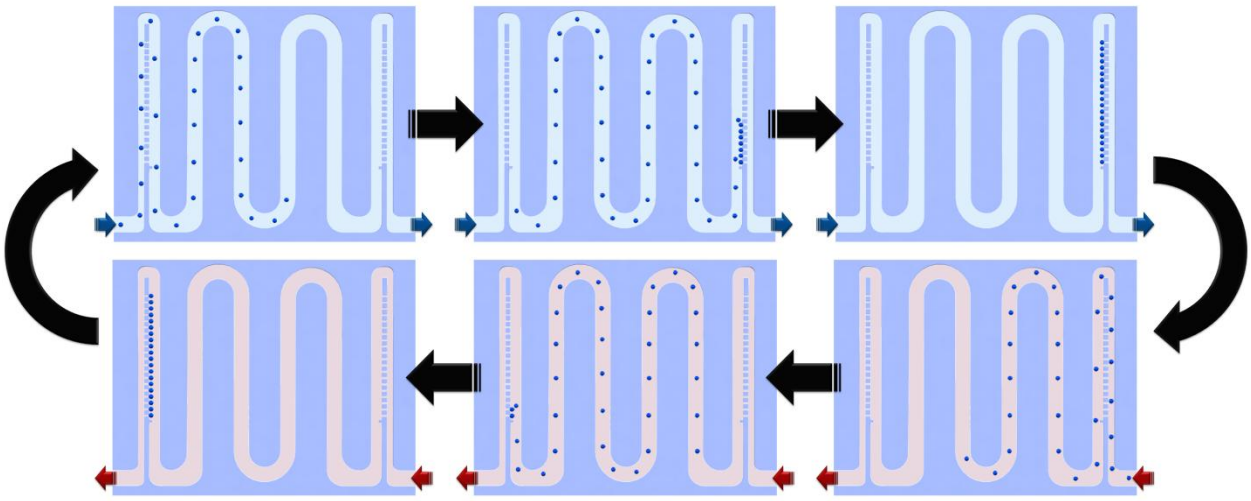

Figure 3.3 Conceptual illustrations of the Microfluidic Ping Pong (MPP) process. The MPP technique consists of two sets of resettable μPAT components that are mirrored with respect to each other and connected by a serpentine mixing channel. (*Top*) For *rightward* flow (*blue arrows*), microparticles: (*i*) bypass the left-side μPAT arrays, (*ii*) undergo dynamic mixing with the inputted solution in the mixing channel, and (*iii*) immobilize in the right-side μPAT arrays. (*Bottom*) By switching the flow polarity to achieve *leftward* flow (*red arrows*), this process is reversed with particles immobilizing in the left-side μPAT arrays. This process can be repeated continuously by switching the flow polarity as desired to mix the microparticles with additional reagents and washes.

The Microfluidic Ping Pong (MPP) concept is illustrated in **Figure 3.3**. In the MPP system, two sets of resettable μPAT components are mirrored with respect to each other and are connected *via* a serpentine microfluidic mixing channel (**Fig. 3.3**). For *rightward* flow,

microparticles: (*i*) bypass the left-side trapping arrays, (*ii*) enter the microfluidic mixing channel for dynamic mixing with the inputted solution, and (*iii*) immobilize in the designated trapping positions in the right-side trapping arrays (**Fig. 3.3** – *top*). By reversing the flow polarity to achieve *leftward* flow, microparticles release from the right-side trapping arrays to enter the mixing channel for dynamic mixing, and then immobilize in the left-side trapping arrays (**Fig. 3.3** – *bottom*). After each switch in the flow polarity, the immobilized particles can be observed visually (*e.g.*, for fluorescence detection). This process can be repeated continuously by reversing the flow polarity to achieve dynamic mixing of microbeads with distinct reagents and fluidic washes. Thus, the trapping arrays are analogous to *ping pong paddles*, ensuring that the microparticles *ping pong* from side-to-side within the MPP system (**Fig. 3.3**).

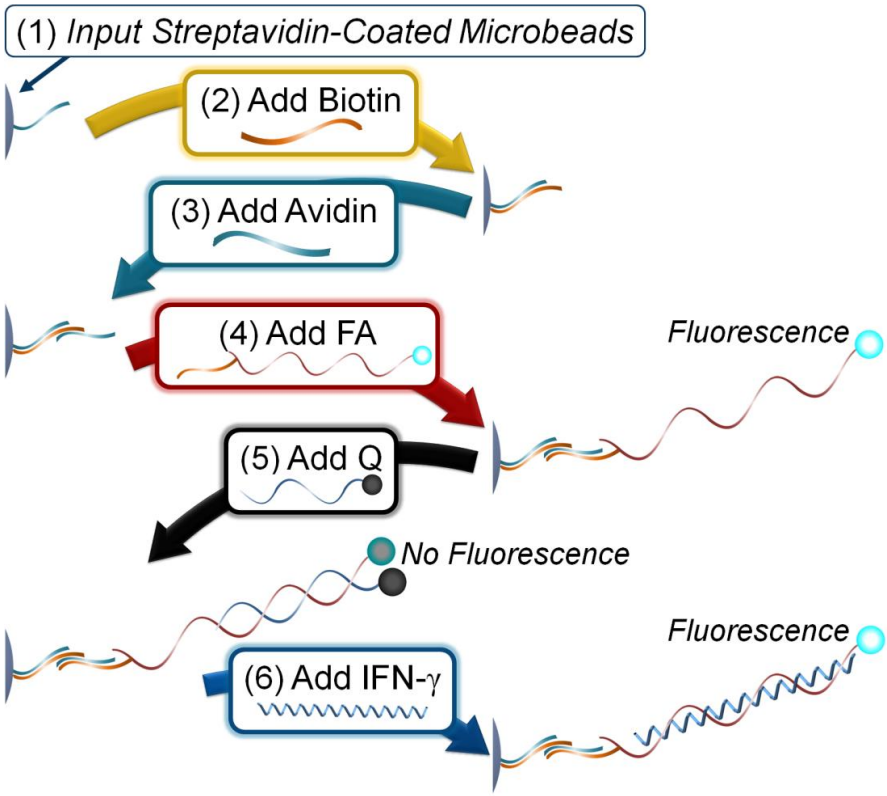

Figure 3.4 Conceptual illustrations of the aptamer beacon-based sandwich assay process for cytokine detection *via* MPP. (1) A suspension of streptavidin-coated microbeads are inputted into the system. (2) The microbeads *ping pong* with a solution of biotinylated bovine serum albumin (BSA). (3) The beads *ping pong* with a solution of NeutrAvidin. (4) The beads *ping pong* with a solution of biotinylated Fluorescent Aptamers (FAs), resulting in fluorescence. (5) The beads *ping pong* with a solution of Quenchers (Qs), which restricts fluorescence. (6) The beads *ping pong* with a solution of the cytokine, Interferon-Gamma (IFN-γ), which displaces the Qs, resulting in fluorescence. In addition, the beads *ping pong* with a wash solution of PBS between each step.

As a demonstrative example of using the MPP platform to achieve multi-stage fluidic reactions and washes, the MPP system was employed to detect the inflammatory cytokine, interferon-gamma (IFN-γ), on microbead substrates *via* a six-step aptamer-based sandwich assay

(**Fig. 3.4**), with a PBS wash between every step (for a total of 11 fluidic stages). The aptamer beacon used was designed previously by Tuleuova *et al.* and consists of two distinct complementary ssDNA sequences: a fluorescent aptamer (FA), and a quencher (Q) (**Table 3.2**).[106] **Figure 3.4** shows conceptual illustrations of the six-step sandwich assay used for detecting IFN-γ *via* MPP: (1) A suspension of streptavidin-coated microbeads was inputted into the MPP system. (2) The microbeads were *ping ponged* with a solution of biotinylated bovine serum albumin (BSA) to facilitate binding of the biotin molecule to the bead surface (*via* the biotin-streptavidin interaction). (3) The microbeads were *ping ponged* with a solution of NeutrAvidin to facilitate binding of the avidin molecule to the bead surface (*via* the avidin-biotin interaction). Steps 1-3 complete the synthesis of the non-fluorescing extended biological linker. (4) The microbeads were *ping ponged* with a solution of biotinylated FAs, resulting in the highest level of fluorescence on the surface of the microbeads (*i.e.*, the positive control). (5) The microbeads were *ping ponged* with a solution of FA-complementary quenchers (Qs) to facilitate hybridization with the FAs, thereby restricting microbead fluorescence (*i.e.*, for the negative control) *via* a FRET interaction. (6) Lastly, the microbeads were *ping ponged* with a solution of IFN-γ to displace the Qs, resulting in an increase in fluorescence (*i.e.*, corresponding to the concentration of IFN-γ in the solution). Additionally, the microbeads were *ping ponged* with PBS washes between each reaction-step. Thus, the full process consisted of 11 fluidic stages in total.

Table 3.2 Names and Sequences (5'-3' orientation) for the Aptamer Beacon.[106]

Name	**Sequence**
Fluorescent Aptamer (FA)	6-FAM-TGGGGTTGGTTGTGTTGGGTGTTGTGT
Quencher (Q)	ACAACCAACCCCA-BHQ-1

3.2.4 Micropost Array Railing (*μ*PAR) for Multi-Stage Fluidic Reactions Under Continuous Flow Conditions

The MPP system presented in **Section 3.2.3** was designed to facilitate multi-stage fluidic reactions *via* a non-continuous flow process. Specifically, each reagent or fluidic wash must be loaded sequentially and separately (*i.e.*, one at a time). Continuous flow methodologies could provide advantages for multi-stage fluidic reactions, particularly in terms of operation time and labor. Unfortunately, the ability to achieve continuous flow mixing of either microbeads or cells with multiple fluidic reagents and washes has remained a significant challenge. Railed microfluidics offers an ideal method for rapidly transporting microparticles into distinct, adjacent flow streams; however, prior microfluidic railing systems have been limited to photopolymerized microstructures[115-117] and microdroplets.[118-120]

Previously, arrayed microposts have been employed in microfluidic systems to regulate microbead immobilization[42] (*see* **Section 3.1.4**) and for transporting microdroplets into parallel flow streams. For microdroplets, Zhang *et al.* used microposts in microfluidics to guide droplets into discrete, sequential streams of polyelectrolytes and washes.[120] One limitation of this system was that one inlet and one outlet were needed for each additional layer or wash step (*i.e.*, for a total of 16 ports). Recently, Kantak *et al.* improved upon this design by enabling the same multi-

layer process to be achieved with only eight ports.[119] Termed "Microfluidic Pinball," this system was used to guide microdroplets (approximately 300 μm in diameter) along rows of circular microposts (40 μm in diameter) into parallel fluidic streams. Although these systems have been successfully employed for microdroplet functionalization, the transportion of microparticles, such as microbeads or cells, into adjacent flow streams has not been demonstrated. The advent of microfluidic railing systems for microparticles could enable diverse continuous flow reaction processes, such as rapid layer-by-layer (LbL) synthesis on microbead substrates.

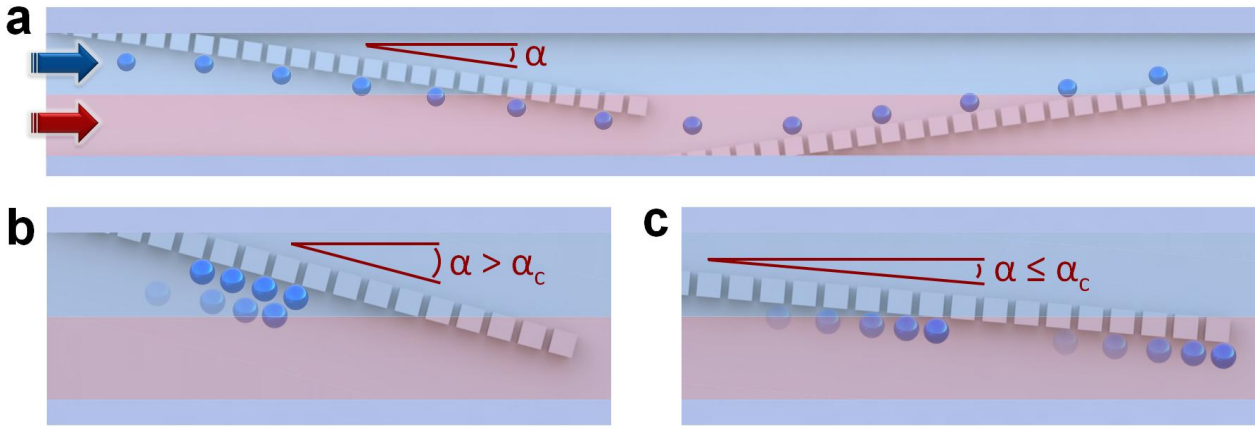

Figure 3.5 Conceptual illustrations of the Micropost Array Railing (μPAR) process. **(a)** Microposts arrayed at an angle, 'α,' serve as a railing system for directing suspended microparticles into adjacent flow streams of reagents and washes. **(b)** For cases where α is greater than the critical angle, 'α_c,' microparticles immobilize in the gaps between microposts. **(c)** For cases where α is less than or equal to α_c, microparticle immobilization is prevented.

Conceptual illustrations of the μPAR concept are shown in **Figure 3.5**. In the μPAR system, microposts are arrayed at an angle, α, with respect to the direction of fluid flow (**Fig. 3.5a**). When suspended microparticles are introduced into the system, the arrayed microposts serve as a railing system for directing the microparticles into parallel fluidic streams (*e.g.*, consisting of bio-molecules or washes) (**Fig. 3.5a**). For cases where the angle α is too high, microparticles will immobilize in the gaps between microposts (**Fig. 3.5b**). As a result, microparticle clogging can occur, leading to device failure. In contrast, when the angle α is less than or equal to the critical angle, α_c, microparticle immobilization is prevented (**Fig. 3.5c**). By tuning α, microparticle immobilization in the microfluidic system can be regulated as desired. Furthermore, additional fluidic reagents and washes can be loaded in parallel to facilitate dynamic microparticle mixing with higher numbers of adjacent solutions.

To demonstrate the functionality of the μPAR methodology, a multiplexed μPAR system was designed to simultaneously synthesize four distinct extended biological linkers onto the surfaces of microbeads in parallel. The ability to achieve multi-layer synthesis on the surface of microbeads is critical for diverse chemical and biological assays.[81, 88, 113] For example, microbeads can be functionalized with MBs to detect a variety of bio-molecules, such as DNA analytes and inflammatory cytokines.[106, 121] Previously, researchers have demonstrated that the length between fluorescent probes (*e.g.*, MBs) and the microbead surface significantly affects the fluorescence response.[122-124] Specifically, increasing the linker length can enhance probe

performance;[87, 125] however, prior reports have also shown that increasing this distance beyond an optimal linker length can result in a decrease in the fluorescence response.[123] To control the distance between immobilized fluorescent probes and the bead surface, extended biological linkers (*e.g.*, consisting of biotin-avidin pairs) can be synthesized onto the surface of microbeads.[87] Unfortunately, functionalizing microbeads with chemicals and bio-molecules off-chip requires considerable time and labor, which has previously hindered the use of bead-based microarrays for applications that require a high number of fluidic stages. This issue presents a particular challenge for situations where extended biological linkers consisting of several biotin-avidin pairs are desired. To overcome such limitations, the μPAR methodology is ideally suited for simultaneously functionalizing microbeads with several distinct linker lengths in parallel under continuous flow conditions.

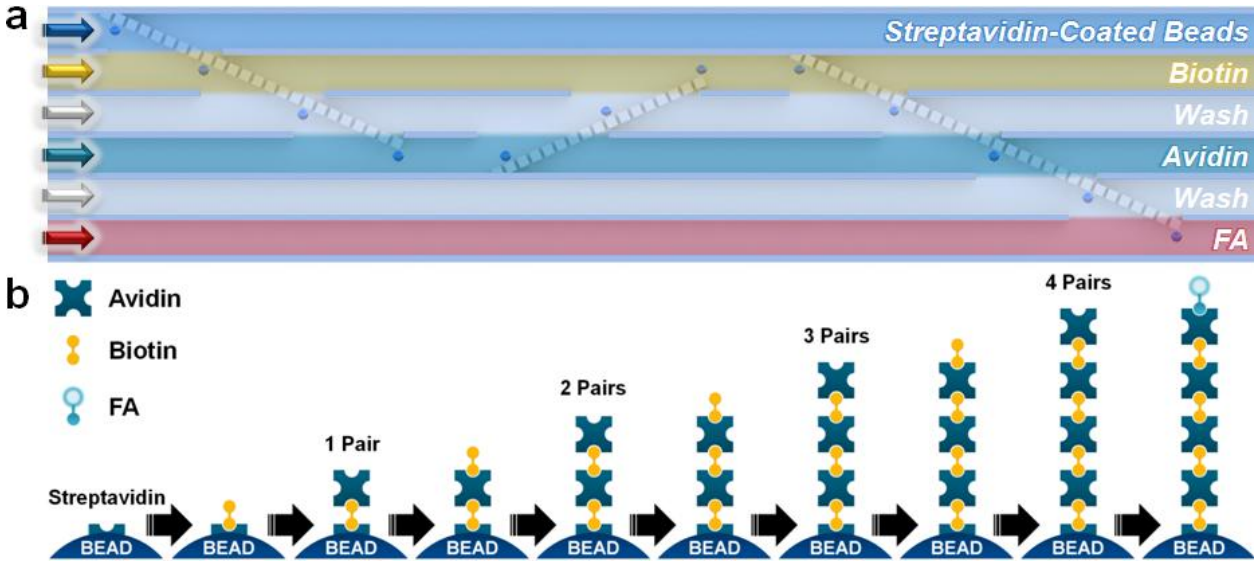

Figure 3.6 Conceptual illustrations of the μPAR system for continuous flow layer-by-layer (LbL) microbead functionalization of extended biotin-avidin-based biological linkers. **(a)** Simplified architecture of the μPAR system (*not to scale*) for the example of synthesizing two biotin-avidin pairs onto streptavidin-coated microbeads. A suspension of streptavidin-coated microbeads (*blue*) is loaded into the device. The microbeads are railed sequentially into adjacent solutions of: (1) biotinylated BSA (*yellow*), (2) PBS wash (*white*), (3) NeutrAvidin (*green*), (4) PBS wash, (5) biotinylated BSA, (6) PBS wash, (7) NeutrAvidin, (8) PBS wash, and (9) biotinylated fluorescent aptamers (*FA*s) (*red*). This process can be repeated or reduced to synthesize a higher or lower number of biotin-avidin pairs onto the streptavidin-coated microbeads, respectively. **(b)** Conceptual illustrations of the reaction process for synthesizing an extended biological linker consisting of four biotin-avidin pairs onto a streptavidin-coated microbead. Ultimately, a FA molecule is immobilized onto the extended biological linker, which results in a detectable fluorescence on the surface of the microbead. This process involves 10 steps with additional fluidic washes between reagents for a total of 18 fluidic stages.

Figure 3.6a shows conceptual illustrations of the μPAR system for the demonstrative example of conjugating an extended biological linker of two biotin-avidin pairs onto streptavidin-coated microbeads. Six input solutions/suspensions were used, including a

suspension of streptavidin-coated microbeads (*blue*), and solutions of biotinylated BSA (*yellow*; *biotin*), NeutrAvidin (*green*; *avidin*), biotinylated FAs (*red*), and two wash solutions of PBS (*white*; *wash*). The PBS wash solutions prevent undesired mixing of the fluidic reagents. The micropost array rails facilitate the sequential transport of suspended microbeads into adjacent fluidic solutions of: (1) biotinylated BSA, (2) PBS wash, (3) NeutrAvidin, (4) PBS wash, (5) biotinylated BSA, (6) PBS wash, (7) NeutrAvidin, (8) PBS wash, and (9) biotinylated fluorescent aptamers (*FA*s) (**Fig. 3.6a**). By adding or removing μPAR sets (*i.e.*, to increase or decrease the number of times microbeads are mixed with the fluidic reagents and washes), a higher or lower number of biotin-avidin pairs can be functionalized onto the streptavidin-coated microbeads, respectively.

Conceptual illustrations of the LbL reaction process for synthesizing an extended biological linker consisting of four biotin-avidin pairs onto the surface of streptavidin-coated microbeads are shown **Figure 3.6b**. The railing process facilitates the repeated, sequential mixing of microbeads with parallel solutions of biotinylated BSA and NeutrAvidin to increase the length of the biological linker one layer at a time *via* biotin-avidin binding interactions. In the multiplexed μPAR system, streptavidin coated-microbeads were functionalized with one, two, three, or four biotin-avidin pairs. At the end of the biological linker synthesis process, each set of microbeads were independently mixed with a solution of biotinylated FAs to immobilize FAs to the microbeads. Thereafter, each set of microbeads were ultimately immobilized *via* separate μPAT arrays (*see* **Section 3.2.1**) for fluorescence visualization and signal detection. At maximum, the reaction process for synthesizing an extended biological linker consisting of four biotin-avidin pairs onto a streptavidin-coated microbead involves 10 stages (**Fig. 3.6b**). Accounting for the additional fluidic wash steps between reagent mixing results in a total of 18 fluidic stages.

3.3 Materials and Methods

3.3.1 Microfabrication

All of the microfluidic systems were fabricated *via* standard soft lithography processes, as shown in **Figure 3.7**. The negative photoresist, SU-8 2010 (*MicroChem*), was spin-coated onto clean Si wafers (**Fig. 3.7a**). Microfeatures were defined *via* contact photolithography (*Hybralign, Series 400, Optical Associates*) (**Fig. 3.7b**). Using the developed photoresist as a negative master, the device was micromolded with the silicone elastomer, PDMS, at a 10:1 (base : curing agent) ratio (*Sylgard 184, Dow Corning, Corning*) (**Fig. 3.7c**). After curing at 55 °C for at least two hours, the PDMS was removed and individual devices were subsequently cut from the PDMS (**Fig. 3.7d**). Ports for the catheter couplers (*Instech Laboratories*) were punched at inlet and outlet locations (**Fig. 3.7e)**. The PDMS devices were cleaned and covalently bonded to Fisherbrand glass microscope slides (*Fisher Scientific*) *via* UV ozone treatment (*UVO cleaner, model 42, Jetlight Company*) (**Fig. 3.7f**).

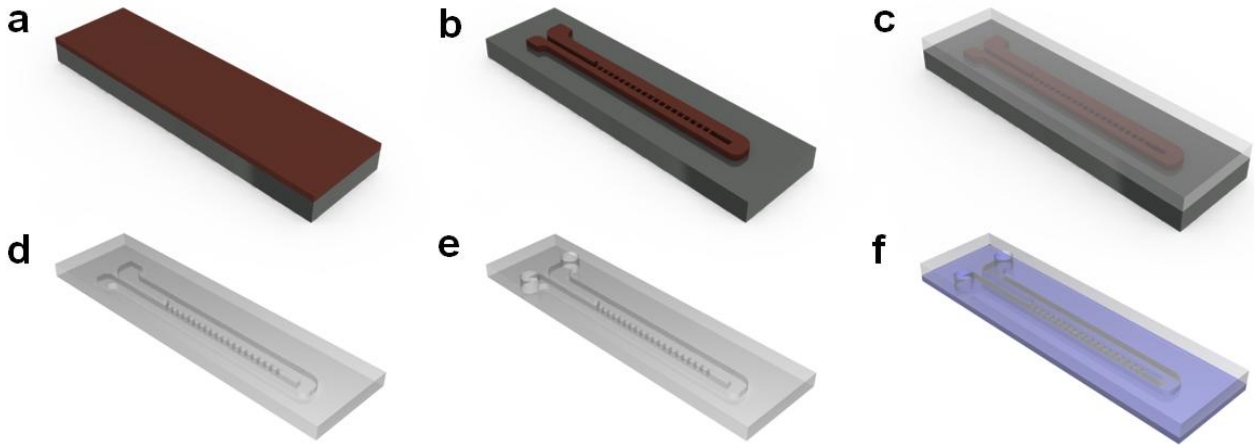

Figure 3.7 Conceptual illustrations of the microdevice fabrication process. **(a)** The negative photoresist, SU-8 2010, was spin-coated onto standard 4" Si wafers. **(b)** Microfeatures were defined *via* contact photolithography. The developed photoresist served as a negative master. **(c)** The device was micromolded with PDMS. **(d)** After curing, the PDMS was removed. **(e)** Ports for the catheter couplers were punched at inlet and outlet locations. **(f)** The PDMS devices were thermally bonded to glass slides.

The devices were designed for 15 μm diameter streptavidin-coated polystyrene microbeads (*#SVP-150*-4, *Spherotech, Inc*.) and suspended BAECs (approximately 10-15 μm in diameter on average). Due to the polydispersity of the microbeads and cells, the heights of the microchannels were set at 18 μm. A filter was integrated into the inlet to limit large microparticles (> 16 μm in diameter) and debris from entering the channels. For the resettable μPAT systems, the microposts were 15×15 μm^2, and the gaps between microposts were 5 μm. For experimental testing, W_T was varied at 30 μm, 35 μm and 40 μm, while W_R was varied at 20 μm, 25 μm and 30 μm. SEM micrographs of fabrication results for a μPAT system with W_T = 35 μm and W_R = 20 μm are shown in **Figure 3.8**.

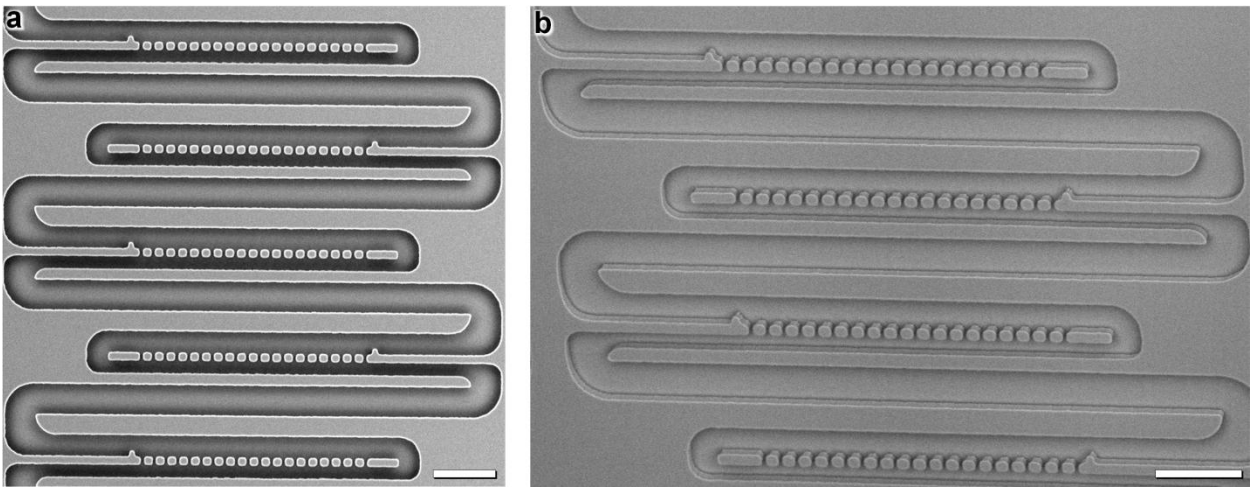

Figure 3.8 SEM micrographs of a resettable μPAT system with W_T = 35 μm and W_R = 20 μm. **(a)** Top view. **(b)** 30° view. Scale Bars = 100 μm

The dynamic microarray for parallel DNA detection (*see* **Section 3.2.2**) was 2 cm × 3 cm in area and included microchannel widths of 50 μm. The MB-microbead mixing channel was 43 cm. Each of the MB-microbead-DNA/Blank mixing channels were 22 cm. For the μPAT arrays, the height of the systems remained 18 μm, the width of the channels (*i.e.*, both W_T and W_R) were 45 μm, the microposts were 15×15 μm^2, and the gaps between microposts were 5 μm.

For the MPP system described in **Section 3.2.3**, two MPP devices were fabricated: (*i*) a singular system for loading one fluidic reagent or wash at a time (**Fig. 3.9a**), and (*ii*) a multiplexed system consisting of four singular systems in parallel (*i.e.*, for simultaneously loading up to four distinct fluidic reagents or washes at a time) (**Fig. 3.9b**). The multiplexed system included five *top* inlets, corresponding to four distinct fluidic reagents or washes (**Fig. 3.9b –** *red*, *clear*, *blue*, *yellow*), as well as an additional buffer solution of PBS to prevent undesired reagent mixing and backflow (**Fig. 3.9b –** *green*). All of the resettable μPAT arrays in the MPP system included a height of 18 μm, W_T of 35 μm, and W_R of 20 μm.

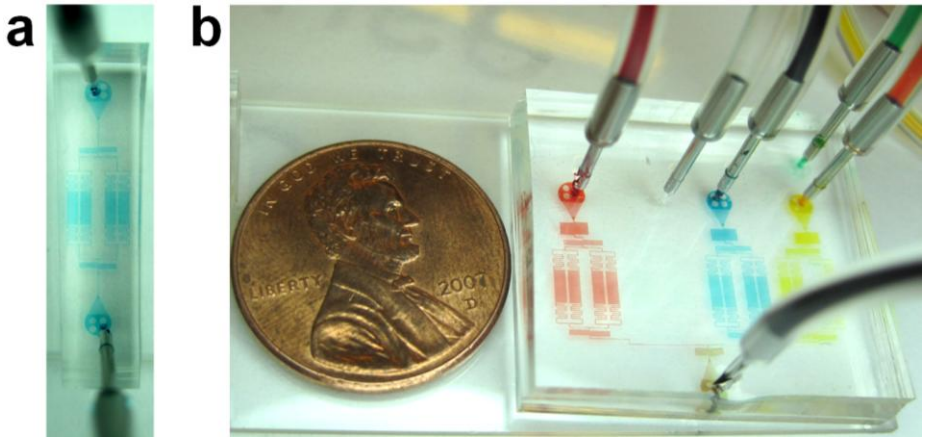

Figure 3.9 Fabrication results for the MPP devices. **(a)** A singular MPP system. **(b)** A multiplexed device with four singular MPP systems in parallel (next to a U.S. penny).

For the μPAR technique described in **Section 3.2.4**, two μPAR systems were fabricated: (*i*) a testing system for experimentally investigating the critical angle, α_c, and (*ii*) a multiplexed system for synthesizing four distinct extended biological linkers in parallel (**Fig. 3.10**). The testing systems included values of α equivalent to 30°, 20°, 10°, 5°, 2.5°, and 1°.

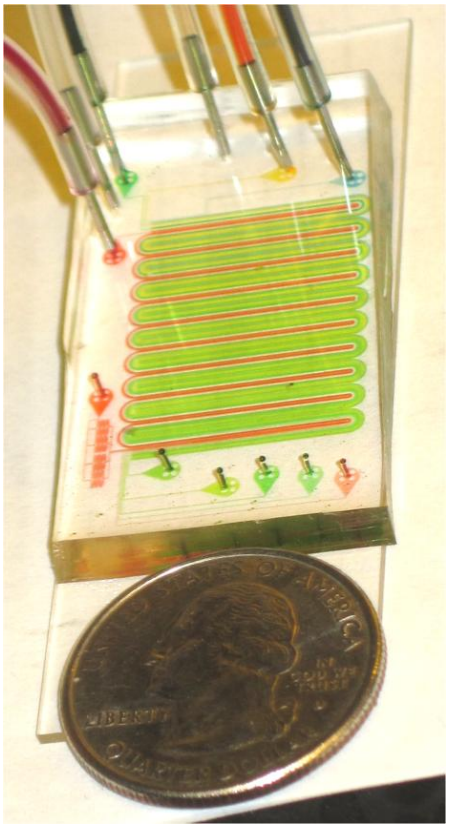

Figure 3.10 Fabrication results for the multiplexed μPAR device (next to a U.S. quarter).

3.3.2 Fluid Velocity Field and Pressure Field Simulations for Resettable μPAT

Three-dimensional fluid velocity field and pressure field simulations were accomplished using the commercial finite element analysis software, COMSOL Multiphysics version 3.5a. The three-dimensional "Incompressible Navier–Stokes" application mode for steady-state analysis was used for all simulations. For the velocity field simulations, the fluid velocity at the inlet was set at 7.0 mm/s. For the pressure field simulations, the pressure at the inlet was set at 480 Pa. For all simulations, the pressure at the outlet was set at 0 Pa, while all other boundary conditions were set to have no-slip conditions. The mesh size was refined to ensure that the simulation results were independent of mesh size. All simulations included mesh sizes of 76,000 ± 3,000 elements. Water ($\rho = 10^3$ kg/m^3; $\eta = 10^{-3}$ Pa·s) was modeled in all of the simulations.

3.3.3 Experimental Reagents

The biotinylated MBs were purchased from Biosearch Technologies, Inc. The MBs were terminally labeled with fluorescein (FAM) on the 5' end of the probe, and a black hole quencher

(BHQ-1) on the 3' end (**Table 3.1**). The biotinylated FAs and Qs were also purchased from Biosearch Technologies, Inc. The FAs were terminally labeled with fluorescein (FAM) on the 5' end of the probe, while the Qs included a black hole quencher (BHQ-1) on the 3' end (**Table 3.2**). The PM, SNP, and MM DNA oligonucleotide sequences (*see* **Section 3.2.1**) were all purchased from Invitrogen Corp. The recombinant human INF-γ was purchased from R&D Systems (*#285-IF-100*). Both the biotinylated BSA and NeutrAvidin were purchased from Sigma-Aldrich Corp. All of the reagents were used without further purification or amplification. For the Blank solutions and all PBS washes, GIBCO^{TM} Dulbecco's 1X PBS (*#14287072; Invitrogen*) was used.

3.3.4 Microbead Functionalization for the Parallel DNA Detection Assay

For the parallel DNA detection experiment described in **Section 3.2.2**, an extended biological linker was synthesized to the streptavidin-coated 15 μm diameter polystyrene microbeads (*#SVP-150-4, Spherotech, Inc*.) prior to loading. Specifically, an extended biological linker composed of biotinylated BSA (biotin) and NeutrAvidin (avidin), which were both purchased from Sigma-Aldrich Corp., was conjugated onto the surface of the microbeads because the fluorescence response of bead-immobilized MBs can be enhanced by increasing the distance from the microbead surface.[87] Laminar diffusion-based mixing facilitated the binding of biotinylated MBs to the microbead surface (*i.e*., microbead – streptavidin – biotinylated BSA – avidin – biotinylated MB).

3.3.5 Cell Suspension Preparation

BAECs were used to investigate the potential of using the: (*i*) resettable μPAT system to trap-and-release cells, and (*ii*) μPAR system to transport cells into adjacent flow streams. After the cells were passaged and cultured as described in **Section 2.3.2**, the remaining cell suspensions were used for testing cell handling in the microfluidic devices.

3.3.6 Experimental Setup

All experiments were conducted under room temperature environment (20-25 °C) and without thermal cycling during device operation. To limit the immobilization of microparticles at locations other than the designated trapping sites, the polysorbate surfactant, Tween 20 (20% in PBS, *Fisher*), was vacuum loaded into all devices prior to operation for a 15 minute incubation period.

3.3.6.1 Resettable μPAT Experiments

For testing the resettable μPAT system (*see* **Section 3.2.1**), a syringe pump (*NE-300, New Era Pump Systems, Inc.*) was used to control the input flow rates. For the trapping efficiency and loading efficiency testing, the flow rate for the microbead suspension (inputted *via* the inlet; 15 μL; 30 beads/μL) was set at 0.25 μL/min. For the resetting efficiency testing, the flow rate for the microbead suspension (inputted *via* the outlet; 60 μL; 5 beads/μL) was set at 1.5 μL/min. For resetting μPAT systems filled with arrayed microbeads, the flow rate for the DI water (inputted *via* the outlet) was set at 1.5 μL/min. For cell handling testing, the trapping mode was

first tested by loading the BAEC suspension (180 cells/μL) *via* the inlet using a syringe pump set at a flow rate of 0.1 μL/min. For testing the resetting mode, two experiments were conducted to examine the efficacy of using DI water and 0.5X trypsin to achieve device resettability. After cells had immobilized in μPAT systems, solutions of either DI water or 0.5X trypsin were loaded *via* the outlet using a syringe pump set at a flow rate of 1.5 μL/min.

3.3.6.2 Parallel DNA Detection Experiments

The dynamic microarray for parallel DNA detection (*see* **Section 3.2.2**), four syringe pumps were used to load PBS into the device at a flow rate of 1 μL/min each *via* the PM, SNP, MM, and Blank inlets, until the Tween solution was removed from the device. Thereafter, six syringe pumps were used to independently control the input flow rates of each homogenous solution or suspension (*i.e.*, microbeads, MBs, PM, SNP, MM, and Blank). The flow rates for the microbead suspension (20 μL; 250 beads/μL) and the MB solution (20 μL; 10 μM) were each set at 0.60 μL/min, while the flow rates for the DNA oligonucleotide solutions (10 μL; 30 μM) and Blank solution (10 μL) were all set at 0.17 μL/min. Laminar diffusion-based mixing of the MB-microbead solution and the MB-microbead-DNA/Blank solutions each occurred in separate serpentine microchannels.

3.3.6.3 MPP Experiments

For the experiments with the singular MPP system (*see* **Section 3.3.1**), a syringe pump was used to control the input flow rates (2 μL/min) for each homogenous solution, suspension, and wash. For the multiplexed system (*see* **Section 3.3.1**), five syringe pumps were used to control the input flow rates (0.5 μL/min) during parallel loading of the homogenous solutions and PBS washes, while a single syringe pump was used to control the input flow rates (2 μL/min) during singular loading of homogenous solutions, suspensions, and PBS washes.

3.3.6.4 μPAR Experiments

For the μPAR α testing experiments (*see* **Section 3.3.1**), three syringe pumps were used to control the input flow rates (0.5 μL/min) for each homogenous solution or suspension. For the multiplexed μPAR system (*see* **Section 3.3.1**), six syringe pumps were used to control the input flow rates (0.5 μL/min) during parallel loading of the homogenous suspensions, solutions, and washes. To determine the fluorescence response of streptavidin-coated microbeads after mixing with the FA solution (*i.e.*, for the negative control), the biotin and avidin solutions were replaced with PBS washes. The control experiments were also run using the multiplexed μPAR device. For cell handling experiments with the μPAR system, the BAEC suspension (180 cells/μL) was loaded into the $\alpha = 1°$ testing system in parallel with a blue-dyed solution and a yellow-dyed solution *via* separate inlet ports. Three syringe pumps were used to control the input flow rates (0.5 μL/min) for each dyed-solution and the cell suspension.

3.3.7 Data Acquisition

All images were taken using a fluorescent inverted microscope (*Motic AE31, Motic Instruments, Inc.*) connected to a Micropublisher 5.0 RTV charge-coupled device (CCD) camera (*QImaging*) and calibrated with QCapturePro (*QImaging*). For the bead-based experimental

runs, all fluorescent images were captured at 100X magnification. For both the dynamic microarray for parallel DNA detection (*see* **Section 3.2.2**) and the μPAR systems (*see* **Section 3.2.4**), fluorescent images were acquired after microbeads were arrayed in the final μPAT arrays. For experiments with the MPP systems (*see* **Section 3.2.3**), images were acquired after the μPAT arrays were filled with trapped microbeads following each reaction-step. The freely available software, ImageJ (*NIH*), was used to quantify the fluorescence response of each arrayed microbead directly from the captured images. Since contact between microbeads can distort the fluorescence response, data was excluded for microbeads that were in contact with other microbeads, or not immobilized in the designated trapping sites.

3.3.8 Quantification of Experimental Results

3.3.8.1 Quantification of μPAT Efficiencies

In prior reports, terms for quantifying particulate-based arrays, such as the "trapping efficiency" (or "yield") and "loading efficiency," have been assigned a variety of definitions. Here, standardized equations are presented for quantifying the efficiencies associated with particulate-based arraying systems. The trapping efficiency (*TE*) was calculated as:

$$TE = \frac{N_a}{N_T} \qquad \textbf{Equation 3.1}$$

where N_a is the number of discrete arrayed particles (*i.e.*, without particle-particle contact) in the designated trapping sites, and N_T is the total number of potential trapping sites that could have been occupied. For testing systems where microparticle clogging was observed, the *TE* was quantified as 0%. **Figure 3.11a** shows *TE*s of 100% (*top*) and 65% (*bottom*).

Defining the loading efficiency (*LE*) as the proportion of loaded particles that are immobilized can be misleading because loading a low number of particles in a system with high numbers of potential trapping sites would produce a high efficiency. To preclude this issue, the *LE* was calculated as:

$$LE = \frac{N_i}{N_L} \text{ for } N_L = N_T \qquad \textbf{Equation 3.2}$$

where N_i is the number of particles immobilized, and N_L is the number of particles loaded – with the condition that the number of particles loaded (N_L) is equivalent to the number of potential trapping sites that could have been occupied (N_T). For testing systems where microparticle clogging was observed, the *LE* was quantified as 0%. **Figure 3.11b** and **Figure 3.11c** show *LE*s of 95% and 100%, respectively.

To quantify microarray resettability, the resetting efficiency (*RE*) for this study was calculated as:

$$RE = \frac{N_m}{N_L} \qquad \textbf{Equation 3.3}$$

where N_m is the number of particles that remain mobile (*i.e.*, particles that are not immobilized at the backs of trapping sites) and N_L is the number of particles loaded from the opposite direction (*e.g.*, *via* the outlet). For testing systems where microparticle clogging was observed, the *RE* was quantified as 0%. **Figure 3.11d** shows a *RE* of 33%.

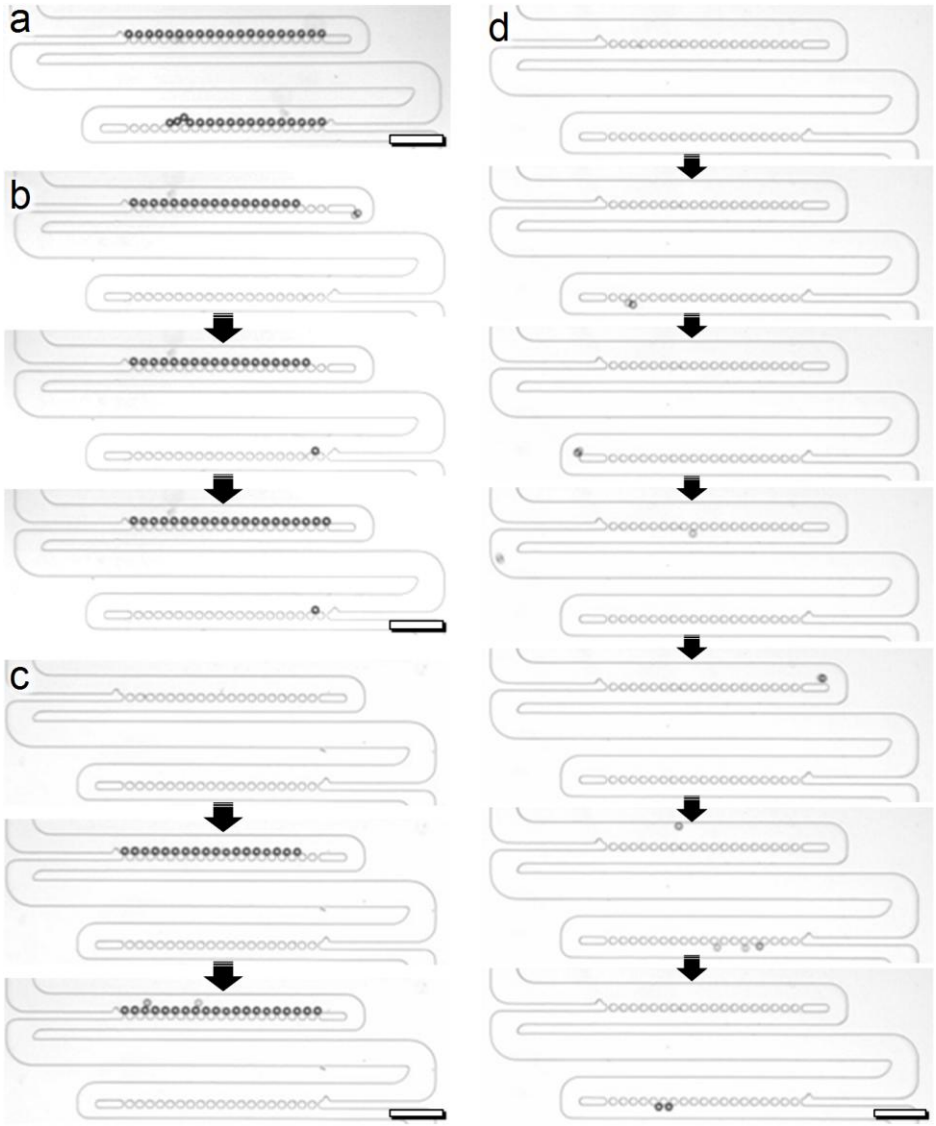

Figure 3.11 Examples for trapping efficiency (*TE*), loading efficiency (*LE*), and resetting efficiency (*RE*) quantification. All efficiencies were quantified using **Equations 3.1-3.3**. **(a)** *TE*s shown are: (*top*) 100%, corresponding to 20 trapped microbeads for 20 potential traps, and (*bottom*) 65%, corresponding to 13 trapped microbeads (*i.e.*, that are not in contact with other beads) for 20 potential traps. **(b)** Sequential micrographs showing a *LE* of 95%, corresponding to 19 of 20 loaded microbeads trapping in the 20 potential vacant traps. **(c)** Sequential micrographs showing a *LE* of 100%, corresponding to 20 of 20 loaded microbeads trapping in the 20 potential vacant traps. **(d)** Sequential micrographs showing a *RE* of 33%, corresponding to 1 of 3 loaded microbeads bypassing the backs of the trapping sites. Scale Bars = 100 μm

3.3.8.2 Quantification of Relative Fluorescence Intensities (*RFI*s) for the Parallel DNA Detection Experiments

Relative fluorescence intensities (*RFIs*) associated with bead-based experiments were quantified from fluorescence images of μPAT-immobilized 15 μm diameter microbeads. For experiments with the dynamic microarray for parallel DNA detection (*see* **Section 3.2.2**), *RFI* values for individual microbeads were calculated as:

$$RFI_i = \frac{x_i - \bar{x}_{Blank}}{\bar{x}_{PM} - \bar{x}_{Blank}} \qquad \textbf{Equation 3.4}$$

where x_i is the fluorescent intensity of a single microbead, $\bar{x}_{Blank}$ is the mean fluorescent intensity of the microbeads that mixed with the Blank solution for the corresponding experiment, and $\bar{x}_{PM}$ is the mean fluorescent intensity of microbeads that mixed with the PM solution for the corresponding experiment. The calculation of *RFI* values normalized the fluorescence results such that the mean *RFI* for the PM case was set at 1, while the mean *RFI* for the Blank case was set at 0.

3.3.8.3 Quantification of *RFI*s for the MPP Experiments

For the MPP experiments (*see* **Section 3.2.3**), *RFI* values for individual microbeads were calculated as:

$$RFI_i = \frac{x_i - \bar{x}_Q}{\bar{x}_{FA} - \bar{x}_Q} \qquad \textbf{Equation 3.5}$$

where x_i is the fluorescent intensity of a single microbead, $\bar{x}_Q$ is the mean fluorescent intensity of the microbeads after mixing with the Q solution for the corresponding experiment, and $\bar{x}_{FA}$ is the mean fluorescent intensity of the microbeads after mixing with the FA solution for the corresponding experiment. The calculation of *RFI* values normalized the fluorescence results such that the mean *RFI*s for the FA case and Q case were set at 1 and 0, respectively.

3.3.8.4 Quantification of *RFI*s for the Multiplexed μPAR Experiments

For the multiplexed μPAR experiments (*see* **Section 3.2.4**), *RFI* values for individual microbeads were calculated as:

$$RFI_i = x_i - \bar{x}_S \qquad \textbf{Equation 3.6}$$

where x_i is the fluorescent intensity of a single microbead, and $\bar{x}_S$ is the mean fluorescent intensity of the microbeads without any biotin-avidin pairs (*i.e.*, with only streptavidin) for the corresponding experiment. The calculation of *RFI* values normalized the fluorescence results such that the mean *RFI* for the streptavidin (*negative control*) case was set at 0.

3.3.8.5 Quantification of Railing Failure Rates (*RFRs*) for the *μ*PAR α Testing Experiments

Railing Failure Rates (*RFR*s) associated with the *μ*PAR α testing experiments (*see* **Section 3.3.1**) were quantified as:

$$RFR = \frac{N_B}{N_G} \qquad \textbf{Equation 3.7}$$

where N_B is the number of microparticles that immobilized in the gaps between microposts, and N_G is the total number of potential gaps between microposts where microparticles could have been immobilized. Thus, an ideal microfluidic railing system would yield a *RFR* of 0%, a system where microbeads immobilized in each gap would yield a *RFR* of 100%, and a system with microbeads that immobilized on top of other immobilized microbeads would yield a *RFR* greater than 100%.

3.3.9 Statistical Analysis

Experimental results are presented as mean ± s.e.m. For experiments with the dynamic microarray for parallel DNA detection (*see* **Section 3.2.2**), the *p* values corresponding to differences in *RFI* between distinct DNA oligonucleotide sequences were calculated *via* one-way analysis of variance (ANOVA) and confirmed *via* unpaired *Student's t tests*. The *p* value corresponding to differences in *RFI* between the MM and Blank cases was calculated *via* unpaired *Student's t tests* because the mean *RFIs* for these cases were not assumed to be different. For all other experiments, *p* values corresponding to differences in *RFI* were calculated *via* unpaired *Student's t tests*. Differences with *p* values less than 0.05 were considered statistically significant.

3.4 Results and Discussion

3.4.1 Resettable μPAT for Particulate Handling

3.4.1.1 Microfluidic Simulations

Three-dimensional COMSOL simulations were performed for the resettable μPAT system using ideal microspheres of 15 μm in diameter. The simulation results are presented in **Figure 3.12**. For the trapping mode (*i.e.*, the positive fluidic flow case), **Figure 3.12a-c** show both the reduction in fluid velocities through the traps after microbead immobilization, and the resulting increase in fluid velocities through the remaining vacant trapping sites. For example, the immobilization of ten microbeads resulted in a 20% decrease in the maximum fluid velocity through the first trapping site, and a 100% increase in the maximum fluid velocity through the eleventh trapping site (**Fig. 3.12a**, **b**). The vacant μPAT arrays in **Figure 3.12a** and **Figure 3.12d** show that the flow through the trapping sites is highest for the first vacant trap and decreases successively. This suggests that sequential microbead trapping would be promoted during the arraying process. As shown in **Figure 3.12e** and **Figure 3.12f**, the pressure drop across the trapping sites suggests that previously trapped microbeads would remain immobilized in the array positions. However, because the pressure drop is highest across the first trapping site and decreases sequentially (**Fig. 3.12f**), the microbeads immobilized in the latter array positions would have a comparatively higher risk of being displaced from the traps (*e.g.*, due to contact from subsequent microbeads entering a 100% filled array).

Figure 3.12g-l show the effects of decreasing the channel size (*i.e.*, reducing W_R) on the flow patterns surrounding microbeads located at trapping channels. In particular, the expanded views of the velocity fields show that that component of the velocity vectors (*red arrows*) perpendicular to the trapping channel are all oriented in the same direction (*rightward*) (**Fig. 3.12g-i**). This is in stark contrast to the expanded views from **Figure 3.12b** and **Figure 3.12c**, where the majority of velocity vectors (*red arrows*) outlining the contour of the trapped microbead are directed into the trapping channel. The flow profile in the velocity and pressure fields for negative fluidic flow suggest that microbead immobilization at the backs of trapping sites would be deterred during experimental runs (**Fig. 3.12g-l**).

3.4.1.2 Trapping Mode for Microbead Suspensions

Experimental results for the trapping mode are shown in **Figure 3.13**. Both W_T and W_R were varied for a total of nine distinct μPAT testing systems. As shown in **Figure 3.13a** and **Figure 3.13b**, systems where W_T = 35 μm were found to have the highest *TE*s and *LEs*, while microbead clogging in the device was not observed for any of these systems. The low *TE*s for the testing systems with W_T = 30 μm were primarily due to a higher proportion of vacant trapping sites (**Fig. 3.13a**). The majority of trap vacancies were caused by subsequent microbeads impacting previously immobilized microbeads that were located in the latter array positions. This issue not only limited the *LE*s (**Fig. 3.13b**), but also resulted in microbead clogging for cases where too many microbeads were simultaneously displaced from the trapping sites. In contrast, the low *TE*s for the testing systems with W_T = 40 μm (**Fig. 3.13a**) were primarily due to a higher proportion of bead-bead contact from subsequent microbeads arraying

on top of previously arrayed beads. This issue consistently resulted in microbead clogging for cases where too many beads arrayed on top of the previously trapped microbeads. While the *LE*s were initially high for these systems, the prevalence of microbead clogging limited the efficiencies (**Fig. 3.13b**).

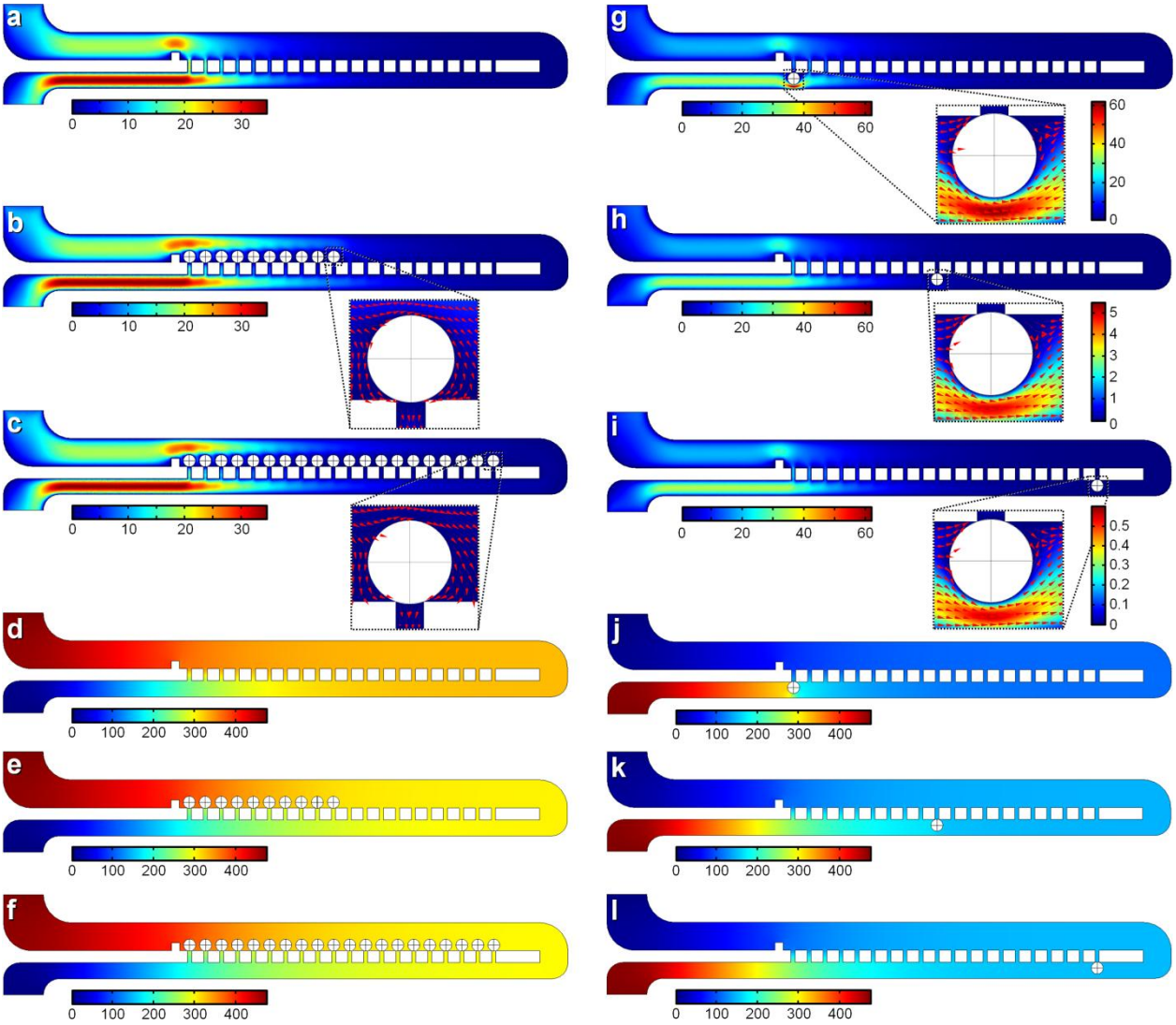

Figure 3.12 Three-dimensional COMSOL simulations of the resettable μPAT system for the trapping mode **(a-f)** and resetting mode **(g-l)**. **(a-c)** Sequential velocity field simulations for μPAT systems with **(a)** zero, **(b)** ten, and **(c)** 20 trapped microbeads under positive fluidic flow. **(d-f)** Sequential pressure field simulations for μPAT systems with **(d)** zero, **(e)** ten, and **(f)** 20 trapped microbeads under positive fluidic flow. **(g-i)** Sequential velocity field simulations for μPAT systems with one microbead located at the back of the **(g)** first, **(h)** tenth, and **(i)** last trapping site under negative fluidic flow. **(j-l)** Sequential pressure field simulations for μPAT systems with one microbead located at the back of the **(j)** first, **(k)** tenth, and **(l)** last trapping site under negative fluidic flow. Units for the velocity fields and pressure fields are mm/s and Pa, respectively. The overlaid red arrows in the expanded views **(b, c, g-i)** mark the direction of the fluid velocity field. W_T and resetting width W_R are 35 μm and 20 μm, respectively.

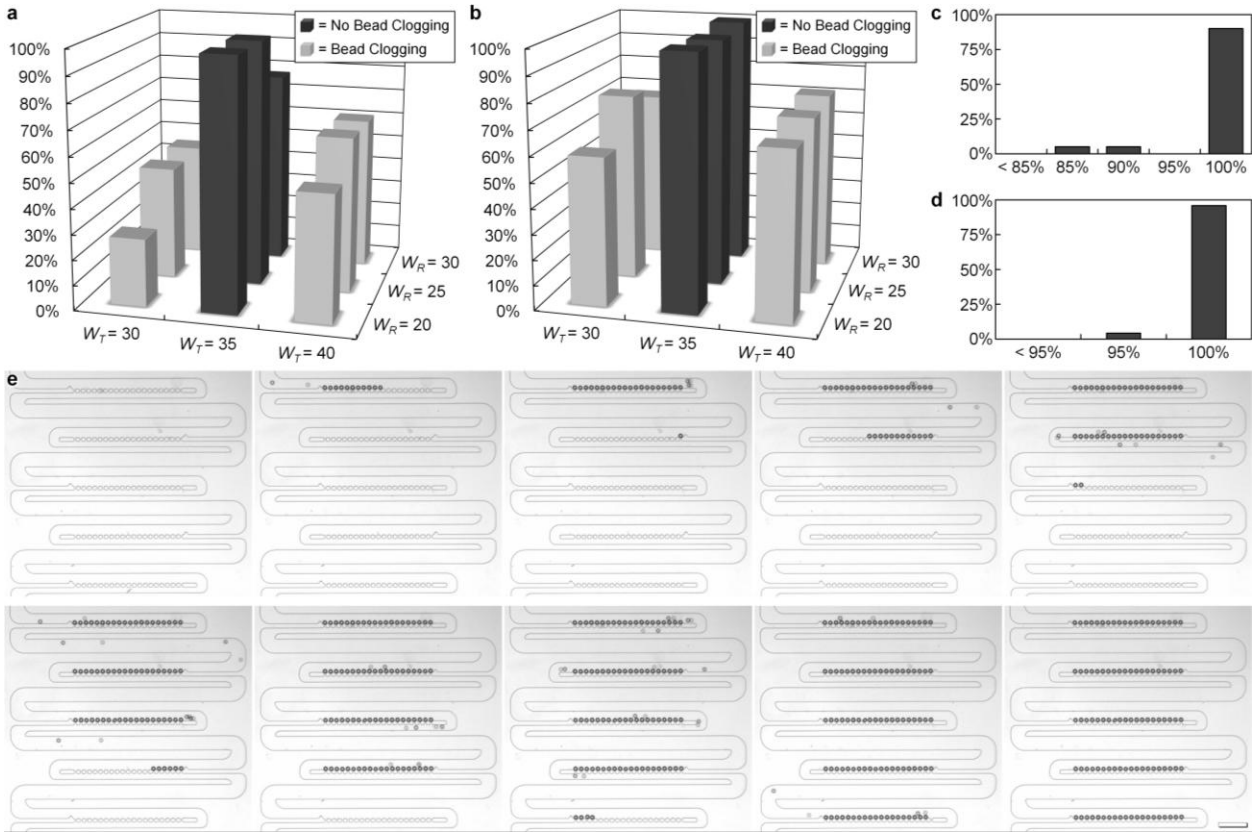

Figure 3.13 Trapping mode experimental results for microbeads in the resettable μPAT system. **(a)** Trapping efficiencies (*TE*s) were quantified using **Equation 3.1** for μPAT arrays with varying trapping widths (W_T) and resetting widths (W_R). **(b)** Loading efficiencies (*LE*s) were quantified using **Equation 3.2** for μPAT arrays with varying W_T and W_R. **(c)** Percentage histogram of *TE* for the μPAT system with W_T = 35 μm and W_R = 20 μm (n = 20 systems). **(d)** Percentage histogram of *LE* for the μPAT system with W_T = 35 μm and W_R = 20 μm (n = 24 systems). **(e)** Sequential micrographs of 100 microbeads (15 μm in diameter) trapping in the μPAT system with W_T = 35 μm and W_R = 20 μm. Dark gray bars denote systems where bead clogging did not occur. Light gray bars denote systems where bead clogging did occur. Scale Bar = 100 μm

For the resettable μPAT system with W_T = 35 μm and W_R = 20 μm, experimental device runs revealed a *TE* of 99% (n = 395 discrete microbeads in 400 traps) and a *LE* of 99.8% (n = 479 microbeads loaded into a possible 480 traps) (**Fig. 3.13a**, **b**). Although microbead trapping was generally sequential in nature, non-sequential trapping was observed during the microbead loading process. **Figure 3.13c** shows a percentage histogram for the observed *TE*s. For the 20 μPAT systems tested, one system included a microbead arrayed on two previously immobilized microbeads, and another system included two microbeads arrayed on three previously immobilized microbeads. All other systems were observed to have 100% *TE*s (**Fig. 3.13c**). **Figure 3.13d** shows a percentage histogram of the observed *LE*s. Of the 24 systems tested, one system was found to have a *LE* of 95% (*i.e.*, due to one microbead bypassing the final vacant trapping site), while *LE*s of 100% were observed for all other systems

(**Fig. 3.13d**). **Figure 3.13e** shows 100 microbeads arraying (over the course of 3.5 min) in the resettable μPAT system for a trapping density of 100 microbeads (15 μm in diameter) in a 0.6 mm^2 area.

3.4.1.3 Resetting Mode for Microbeads

Experimental results for the resetting mode are shown in **Figure 3.14**. Experimental device runs revealed *RE*s of 100% for all systems where W_R = 20 μm (**Fig. 3.14a**). Microbead clogging was not observed in any of these systems. Increasing W_R was found to decrease the *RE*s. Specifically, microbead clogging was observed in all of the testing systems where W_R = 25 μm or 30 μm (**Fig. 3.14a**). For example, **Figure 3.14b** shows one microbead bypassing the backs of the trapping sites while beads clog in a testing system with W_T = 30 μm and

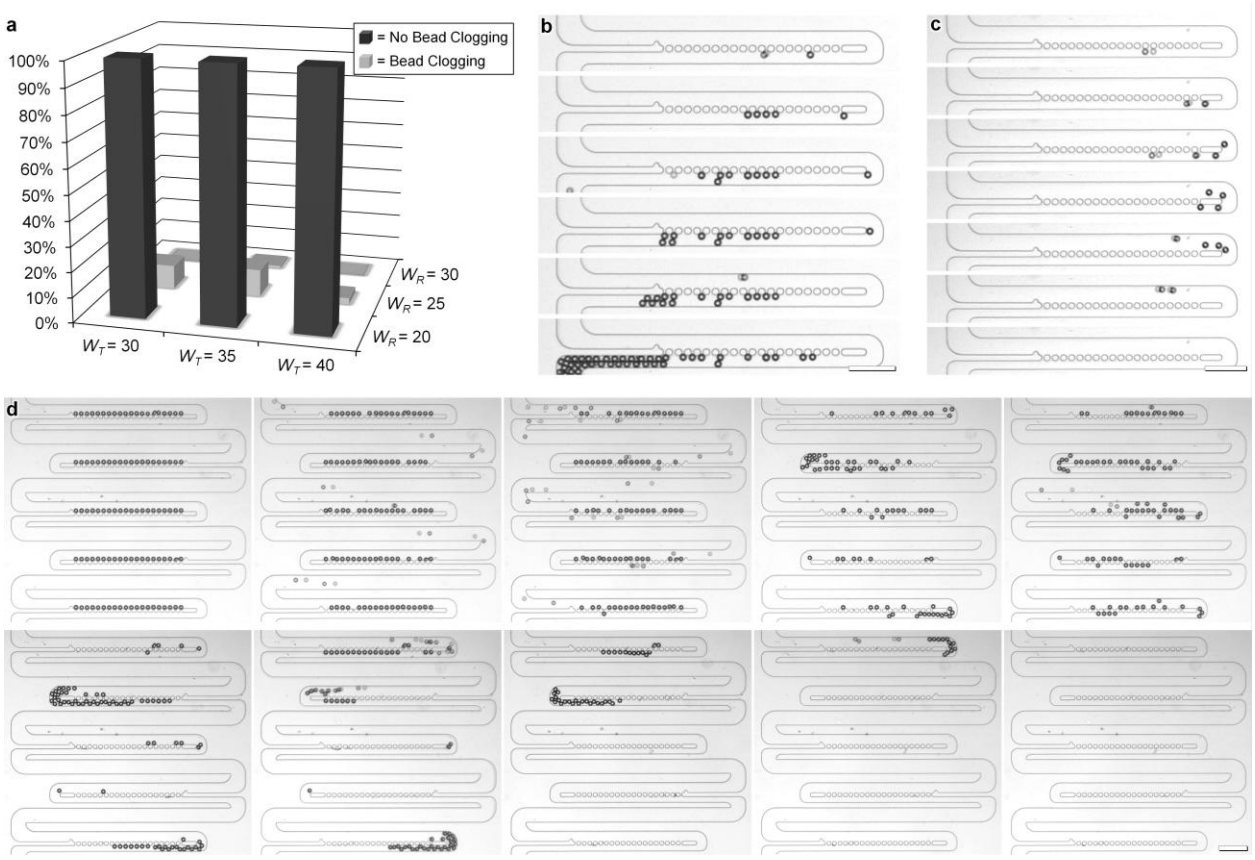

Figure 3.14 Resetting mode experimental results for microbeads in the resettable μPAT system. **(a)** Resetting efficiencies (*RE*s) were quantified using **Equation 3.3** for μPAT arrays with varying trapping widths (W_T) and resetting widths (W_R). Dark gray bars denote systems where bead clogging did not occur. Light gray bars denote systems where bead clogging did occur. **(b)** Sequential micrographs of one microbead (15 μm in diameter) bypassing the backs of the trapping sites while a bead clog is formed in a testing system with W_T = 30 μm and W_R = 25 μm. **(c)** Sequential micrographs of microbeads (15 μm in diameter) bypassing the backs of the trapping sites in a testing system with W_T = 40 μm and W_R = 20 μm. **(d)** Sequential micrographs of 100 arrayed microbeads (15 μm in diameter) releasing from a μPAT array with W_T = 35 μm and W_R = 20 μm. Scale Bars = 100 μm

W_R = 25 μm. Microbead clogging primarily occurred *via* a three-step process where: (*i*) microbeads would immobilize at the backs of the trapping sites, (*ii*) subsequent microbeads entering the system would follow flow streams that bypass a previously immobilized microbead, and then (*iii*) the subsequent microbeads would become trapped between the previously immobilized microbeads and the channel wall (*i.e.*, due to the width of the channel). However, by decreasing W_R to 20 μm, this issue was avoided for all values of W_T tested (**Fig. 3.14a**). For example, **Figure 3.14c** shows a *RE* of 100% for a testing system with W_T = 40 μm and W_R = 20 μm.

For the resettable μPAT system with W_T = 35 μm and W_R = 20 μm, experimental testing revealed a *RE* of 100% (n = 400 microbeads in 24 systems) (**Fig. 3.14a**). Because this μPAT system was demonstrated to successfully array microbeads in the designated trapping positions (**Fig. 3.13e**), microarray resettability after the microbead arraying process was also investigated. One issue associated with releasing functionalized microbeads from PDMS traps is that the microbeads can *attach* to their surrounding area. Although this phenomenon was observed to some extent, microarray resettability was not prevented. Experimental device runs revealed 100% resettability (n = 400 microbeads from a total of 20 systems) for μPAT systems filled with microbeads. For example, **Fig. 3.14d** shows full microarray resettability (over a time-span of approximately 10 min) for 100 arrayed microbeads in the resettable μPAT system. Thus, the resetting mode was demonstrated both by loading microbead suspensions *via* the outlet port, as well as by releasing previously arrayed microbeads from the designated trapping positions to reset the microarray.

3.4.1.4 Cell Handling in the Resettable μPAT System

The capability of employing the μPAT technique to trap-and-release cells was also investigated. Suspended BAECs were loaded into μPAT systems under positive fluidic flow. Experimental observations revealed that the μPAT system effectively transported suspended cells to designated trapping sites (**Fig. 3.15a**). However, there were several differences for arraying cells compared to trapping microbeads (*see* **Section 3.4.1.2**). A higher degree of cell-cell contact was observed in the trapping sites, although this result was primarily caused by previously-formed BAEC clusters entering the device and immobilizing in the μPAT arrays (**Fig. 3.15b** – *arrow*). Microfluidic filtering systems could be designed and implemented to bypass such issues. Additionally, BAEC trapping was slightly limited by transiency. Specifically, approximately two hours after cell trapping, a small number of previously immobilized BAECs were observed to migrate through the gaps between microposts (**Fig. 3.15c** – *arrow*). The number of cells exhibiting such behavior increased with time. One potential basis for this result is that the flow patterns in the μPAT arrays would promote cellular mechanotaxis through the trapping sites due to the directions of fluidic shear stress and pressure (**Fig. 3.12**). These results suggest that the microfluidic conditions should be optimized if longer experimental time-lengths for cell arraying are desired, which is consistent with prior reports of cell trapping in dynamic microarrays.[91]

After BAECs were immobilized in the μPAT arrays, the potential for releasing cells from the system was also examined by reversing the flow direction. Device resettability was investigated for solutions or DI water and 0.5X Trypsin in separate experiments. Under reverse

fluidic flow of DI water, only partial resettability was achieved. For example, **Figure 3.15d** shows sequential micrographs of a low percentage of cells releasing from trapping sites during reverse loading of DI water. In contrast to microbeads, cells can form strong attachments to their surrounding microenvironment. It is likely that the strength of cell adhesions could account for the limited resettability observed under reverse flow of DI water. To bypass issues associated with cell adhesion in the microfluidic system, a solution of 0.5X Trypsin – a chemical that is widely used to facilitate cellular detachment from the substratum – was loaded under reverse flow conditions. Experimental observations revealed that 0.5X Trypsin was effective for promoting the release of previously immobilized cells from the trapping sites. For example, **Figure 3.15e** shows sequential micrographs of previously arrayed cells being released from all of the trapping sites during reverse loading of 0.5X Trypsin. These results suggest that the resettable μPAT methodology could provide a valuable platform for achieving both high-density single cell trapping and full device resettability for dynamic cell-based microarrays.

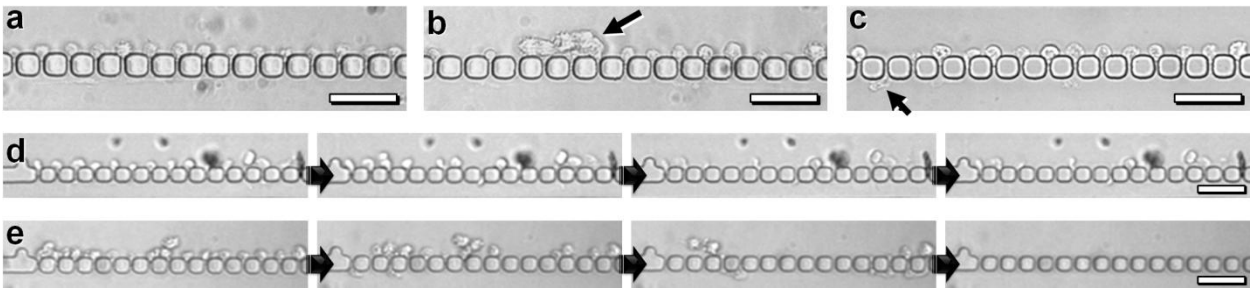

Figure 3.15 Experimental results for **(a-c)** trapping and **(d, e)** releasing BAECs in the resettable μPAT system. **(a)** Micrograph showing 100% *TE* of cells immobilized in trapping positions *via* μPAT. **(b)** Micrograph showing μPAT-immobilized cells and a cell cluster (*arrow*). **(c)** Micrograph showing μPAT-immobilized cells after two hours, with a cell that migrated through a trapping site (*arrow*). **(d)** Sequential micrographs showing limited resettability under reverse flow of DI water. **(e)** Sequential micrographs showing full resettability under reverse flow of 0.5X Trypsin. Scale Bars = 50 μm

3.4.2 Parallel DNA Detection *via* a Dynamic Bead-Based Microarray with μPAT

The microfluidic bead-based platform described in **Section 3.2.2** was employed to: (*i*) immobilize solution-phase MBs onto the surfaces of microbeads, (*ii*) simultaneously mix the microbeads with four homogenous solutions (*i.e.*, PM, SNP, MM, and Blank) in parallel, and then (*iii*) array each set of suspended microbeads in separate μPAT arrays to detect the fluorescence response corresponding to each solution. Experimental results revealed that the microbeads with surface-immobilized MBs exhibited distinct and reproducible fluorescence intensities corresponding to each of the ssDNA oligonucleotide sequences (**Fig. 3.16**). **Figure 3.16a-d** show fluorescence micrographs of μPAT-immobilized microbeads from a single experiment after mixing with the: **(a)** PM, **(b)** SNP, **(c)** MM, and **(d)** Blank solutions in parallel. Prior to quantification, differences in fluorescence between the three DNA analytes can be observed visually. Solution phase MB-DNA hybridization occurred in the microchannels, which resulted in background fluorescence corresponding to the degree of matching between the MB and the DNA oligonucleotide sequences. However, because of the high fluorescence of the

microbead-immobilized MBs, **Figure 3.16** shows that accurate and quantitative results were achieved without the need for additional time-consuming fluidic wash steps to eliminate the background noise.

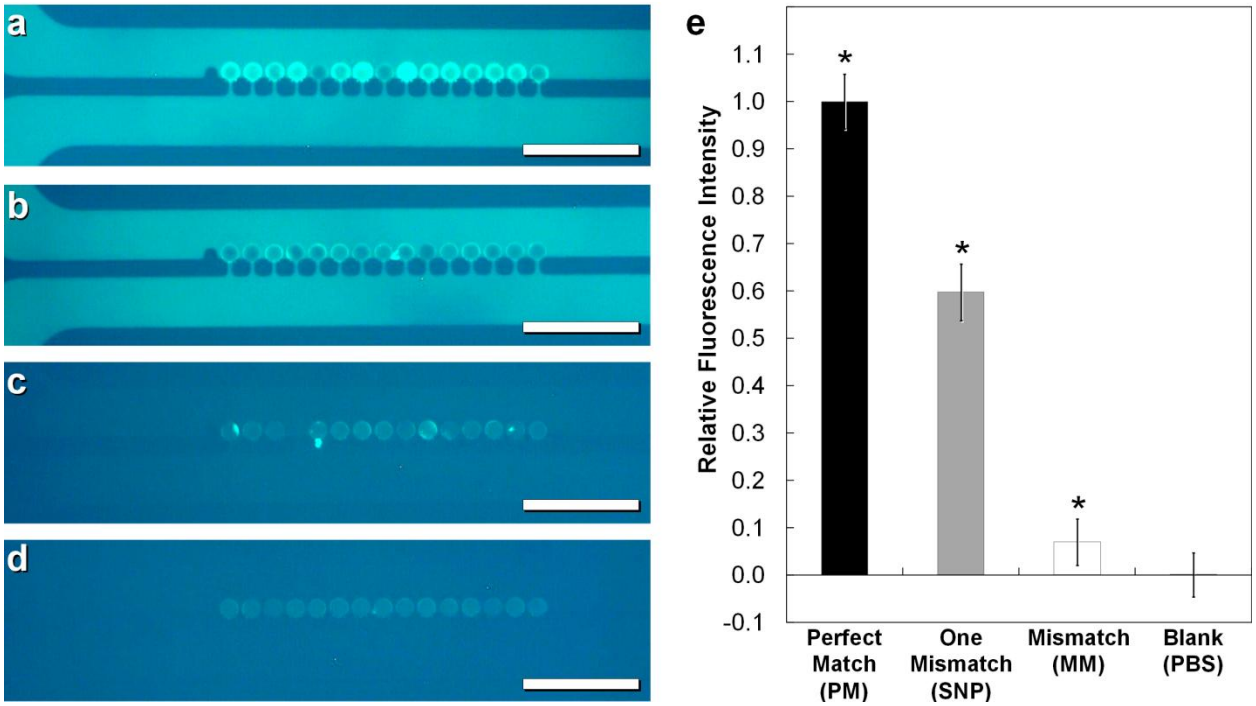

Figure 3.16 Experimental results for microbead fluorescence. **(a-d)** Fluorescence micrographs from a single experiment showing arrayed 15 μm in diameter microbeads with surface-immobilized MBs after mixing with: **(a)** Perfect Match (PM), **(b)** One Mismatch (SNP), **(c)** Mismatch (MM), and **(d)** Blank (PBS) solutions. Scale Bars = 100 μm. **(e)** Relative fluorescence intensities (*RFIs*) corresponding to PM (n = 148), SNP (n = 194), MM (n = 124), and Blank (n = 158) solutions. *RFI*s were quantified using **Equation 3.4**. * denotes $p < 10^{-5}$ statistically significant differences. Error bars represent s.e.m.

Microbead *RFI*s were quantified using **Equation 3.4**. The quantified fluorescence results are shown in **Figure 3.16e**. Each DNA oligonucleotide sequence was found to produce a statistically discernable *RFI*. Microbeads with surface-immobilized MBs that mixed with the PM solution produced the highest fluorescence response, with an average *RFI* of 1.00±0.06. A single base-pair mismatch was found to significantly reduce the microbead fluorescence ($p < 10^{-5}$). The average *RFI* corresponding to the SNP solution was 0.60±0.06. After mixing with the MM solution, microbeads exhibited an average *RFI* of 0.07±0.05. The MM average *RFI* was distinguished from both the PM and SNP cases ($p < 10^{-5}$). In contrast, the MM average *RFI* was not discernable from the Blank case (p = 0.31), which demonstrates the specific binding of the MB. Microbeads that mixed with the PBS solution produced an average *RFI* of 0.00±0.05. Thus, although the three DNA oligonucleotide sequences were observed to exhibit distinct fluorescence intensities, the fluorescence response corresponding to the MM and Blank solutions was not statistically distinguishable (**Fig. 3.16e**).

3.4.3 MPP for Bead-Based Cytokine Detection

3.4.3.1 Multiplexed MPP for Extended Biological Linker Length Optimization

Initially, the multiplexed MPP system was employed to optimize the extended biological linker length for detecting IFN-γ (*i.e.*, instead of maximizing the microbead fluorescence response). Four distinct biological linkers were synthesized onto the microbeads off-chip, prior to loading the microbeads in the microfluidic system. The four sets of streptavidin-coated microbeads included: (*i*) zero biotin-avidin pairs (S), (*ii*) one biotin-avidin pair (SBA), (*iii*) two biotin-avidin pairs (SBABA), and (*iv*) three biotin-avidin pairs (SBABABA). IFN-γ *RFI*s were quantified using **Equation 3.5**. The results of the biological linker optimization test are shown in **Figure 3.17**. The extended biological linker with one biotin-avidin pair bound to a streptavidin molecule resulted in the highest average IFN-γ *RFI* (**Fig. 3.17** – SBA). Thus, this extended biological linker was used for the 11-stage MPP-based IFN-γ detection assays.

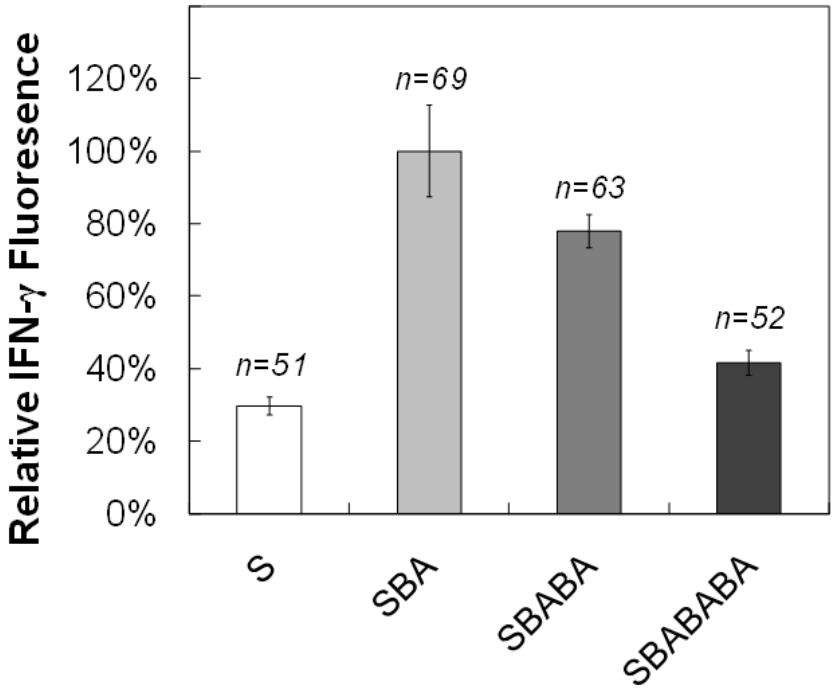

Figure 3.17 Biological linker optimization experimental results for the relative IFN-γ fluorescence intensity. Relative IFN-γ fluorescence intensities were quantified using **Equation 3.5**. 'S' = Streptavidin; 'B' = Biotin; 'A' = Avidin; Error Bars denote s.e.m.

3.4.3.2 MPP for Cytokine Detection *via* an 11-Stage Fluidic Process

The single MPP system was employed to accomplish an 11-stage fluidic process and detect IFN-γ at a concentration of 100 pM. After dynamic mixing with distinct reagents and wash steps, the same set of microbeads was visualized for fluorescence detection after every stage of the multi-step process. **Figure 3.18a-f** show fluorescence micrographs of arrayed 15 μm diameter microbeads after each of the six steps of the aptamer-based sandwich assay for cytokine

detection (*see* **Fig. 3.4**). Prior to quantification, differences in fluorescence between the FA, Q, and IFN-γ cases can be observed visually. Solution-phase FAs were found to produce background noise for the FA case; however, this background noise was eliminated after the subsequent PBS wash.

Microbead *RFI*s were quantified using **Equation 3.5**. The quantified fluorescence results are shown in **Figure 3.18g**. The experimental results revealed that after the build-up of the extended biological linker (*i.e.*, Streptavidin-Biotin-Avidin), each of the subsequent solutions produced statistically discernable fluorescence intensities. Additionally, the average *RFI* values were consistent between multiple experiments. After mixing with the FA solution, the microbeads exhibited the highest fluorescence response, corresponding to a *RFI* of 1.00±0.02. Mixing with the Q solution was found to significantly reduce the microbead fluorescence ($p < 0.0001$). The average *RFI* corresponding to the Q solution was 0.00±0.01. However, mixing with the 100 pM solution of IFN-γ significantly increased the microbead fluorescence ($p < 0.0005$), resulting in an average *RFI* of 0.06±0.01. Thus, these results demonstrate the detection sensitivity of 100 pM of IFN-γ *via* the MPP system.

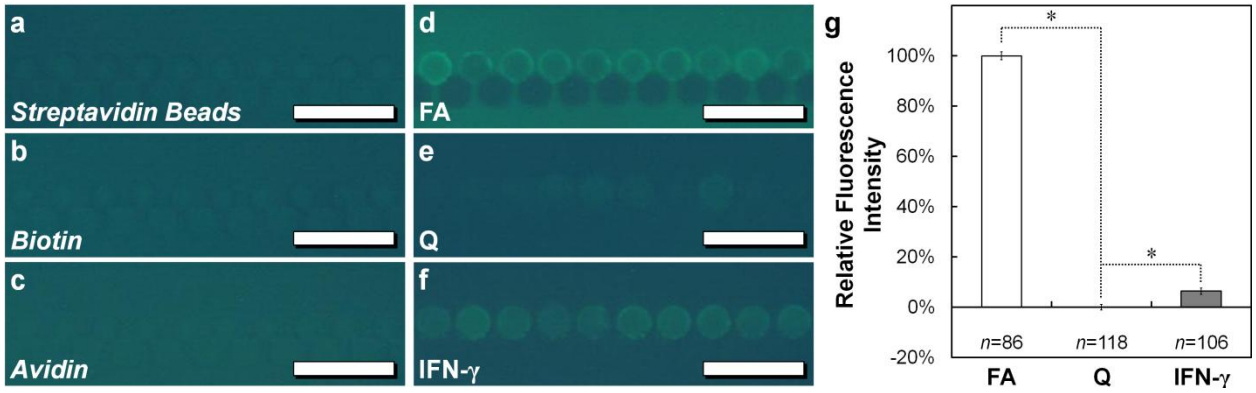

Figure 3.18 Experimental results for IFN-γ detection *via* an aptamer-based sandwich assay in the MPP System. **(a-f)** Fluorescence micrographs of arrayed 15 μm diameter microbeads after each step of the aptamer-based sandwich assay (*see* **Fig. 3.4**). Scale Bars = 50 μm. **(g)** Average relative fluorescence intensities (*RFI*s) of arrayed microbeads after mixing with the FA, Q, and IFN-γ solutions. *RFI*s were quantified using **Equation 3.5**. Error Bars denote s.e.m.; * denotes $p < 0.0005$ statistically significant differences.

3.4.4 μPAR for Continuous Flow Particulate Handling

3.4.4.1 μPAR α Testing

The first step toward characterizing the μPAR technique was to employ the μPAR α testing systems (*see* **Section 3.3.1**) to experimentally investigate the critical angle, α_c, required for preventing microbeads from immobilizing in the gaps between microposts. Previously, an α of 30° was demonstrated to successfully guide microdroplets;[119] however, microbeads were observed to immobilize in the spaces between microposts when α was too large (**Fig. 3.19**). For example, **Figure 3.19a-d** show microbeads immobilized in μPAR systems with: **(a)** α = 30°, **(b)** α = 20°, **(c)** α = 10°, and **(d)** α = 5°. Experimental observations revealed that decreasing α

resulted in a lower number of microbeads immobilizing in the μPAR testing systems. **Figure 3.19e** shows sequential micrographs of microbeads being railed and then immobilized in a system with $\alpha = 2.5°$ (*top*), while microbeads are successfully railed in a system with $\alpha = 1°$ (*bottom*). *RFR*s were quantified using **Equation 3.7**. The quantified results for the *RFR* corresponding to each value of α tested are shown in **Figure 3.19f**. The failure rate was found to decrease as the angle α was reduced. The system with $\alpha = 1°$ was the only μPAR system tested where microbead immobilization was prevented completely. Rather, suspended microbeads were guided along the micropost array rails into the parallel flow streams.

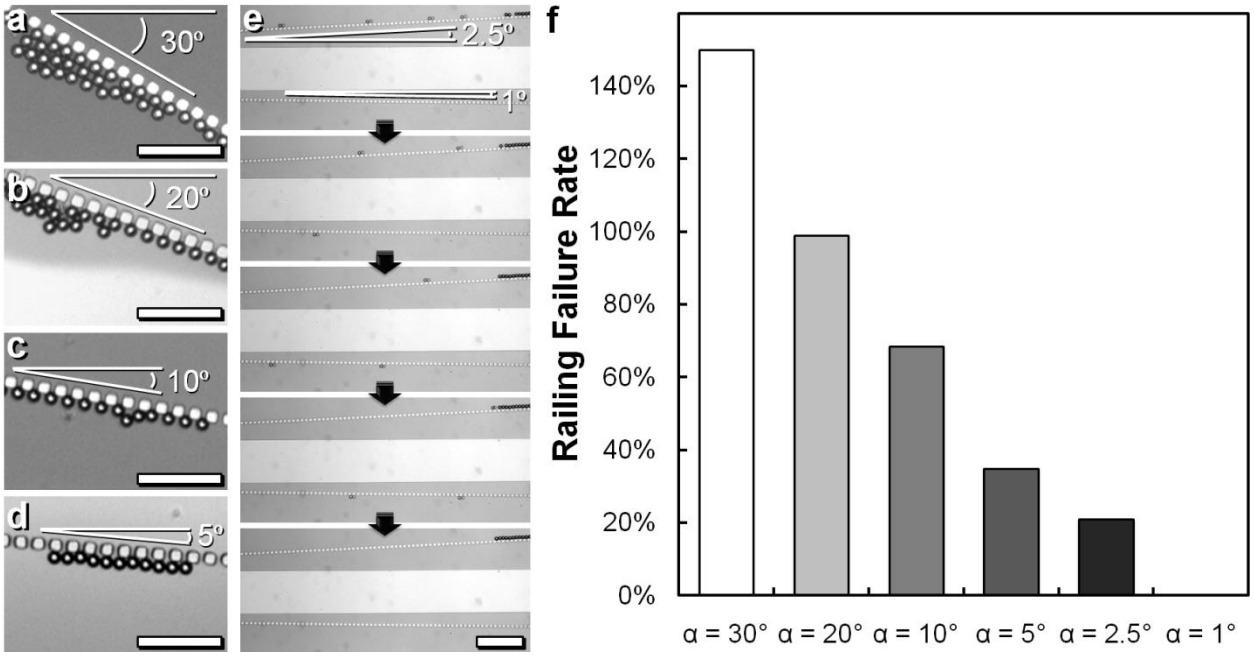

Figure 3.19 Experimental results for μPAR systems with varying α. **(a-d)** Micrographs of microbeads immobilized in μPAR systems with: **(a)** $\alpha = 30°$, **(b)** $\alpha = 20°$, **(c)** $\alpha = 10°$, and **(d)** $\alpha = 5°$. Scale Bars = 100 μm. **(e)** Sequential micrographs of microbeads railing and then immobilizing in a system with $\alpha = 2.5°$ (*top*), while microbeads are simultaneously railed without being immobilized in a system with $\alpha = 1°$ (*bottom*). Scale Bar = 200 μm. **(f)** Quantified results for the railing failure rate (*RFR*) corresponding to each α tested. *RFR* values were quantified using **Equation 3.7**.

3.4.4.2 Synthesizing Four Distinct Extended Biological Linker Lengths in Parallel *via* Multiplexed μPAR

For the synthesis of the four extended biological linkers in parallel, an α of 1° was used. The micropost array rails were observed to direct the microbeads through the distinct reagents and wash solutions as designed. For example, **Figure 3.20** shows sequential micrographs of microbeads being transported from: **(a)** the bead suspension (*blue*) to the biotinylated BSA solution (*yellow*), **(b)** the biotinylated BSA solution (*yellow*) to the PBS wash solution (*white*), **(c)** the PBS wash solution (*white*) to the NeutrAvidin solution (*green*), **(d)** the NeutrAvidin solution (*green*) back to the PBS wash solution (*white*), and **(e)** the PBS wash solution (*white*) back to the biotinylated BSA solution (*yellow*). In the multiplexed μPAR system, streptavidin

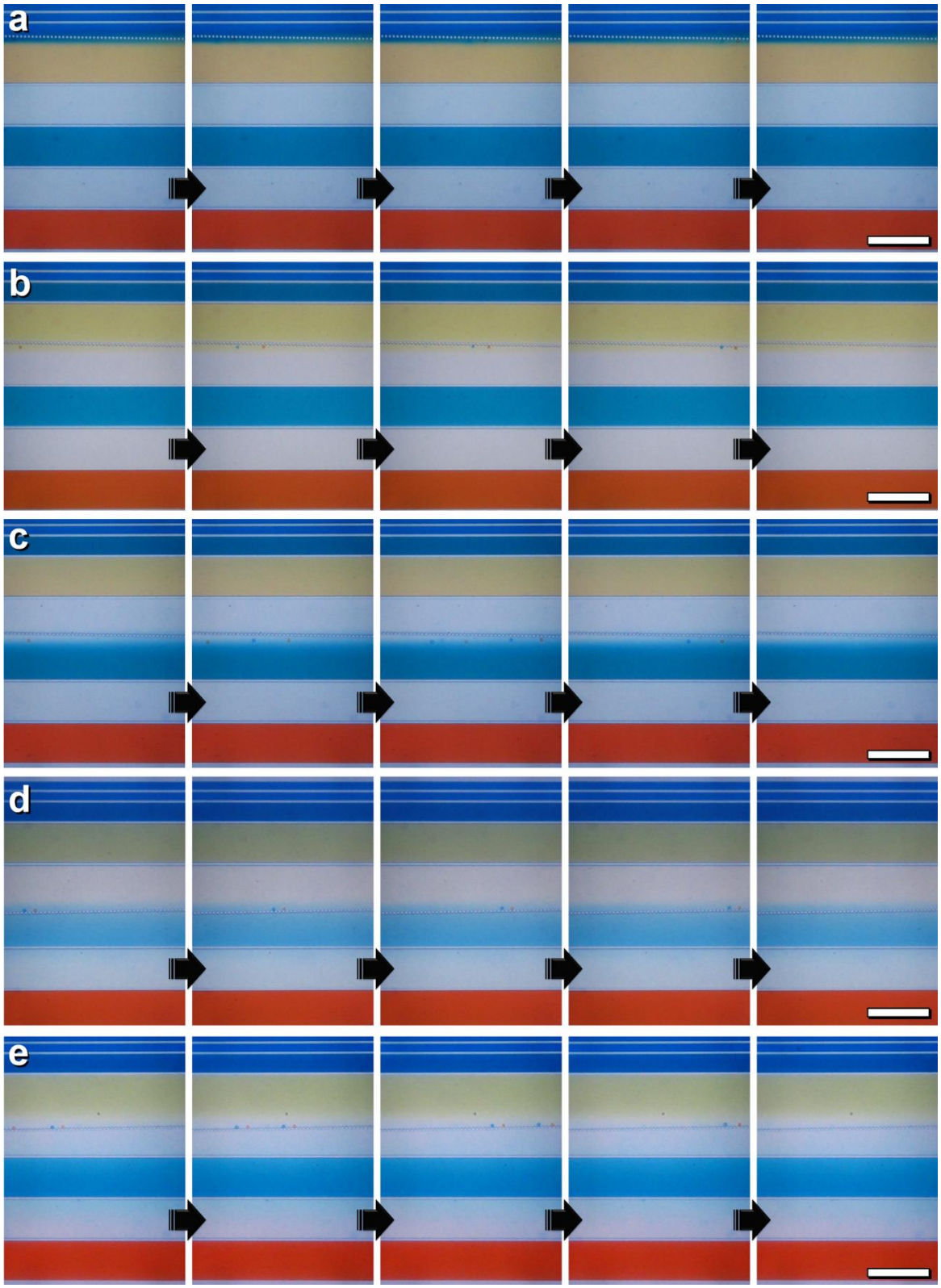

Figure 3.20 Experimental results for μPAR. Microbeads rail from: **(a)** the bead suspension to the biotin solution, **(b)** the biotin solution to the wash, **(c)** the wash to the avidin solution, **(d)** the avidin solution back to the wash, and **(e)** the wash to the biotin solution. Scale Bars = 300 μm

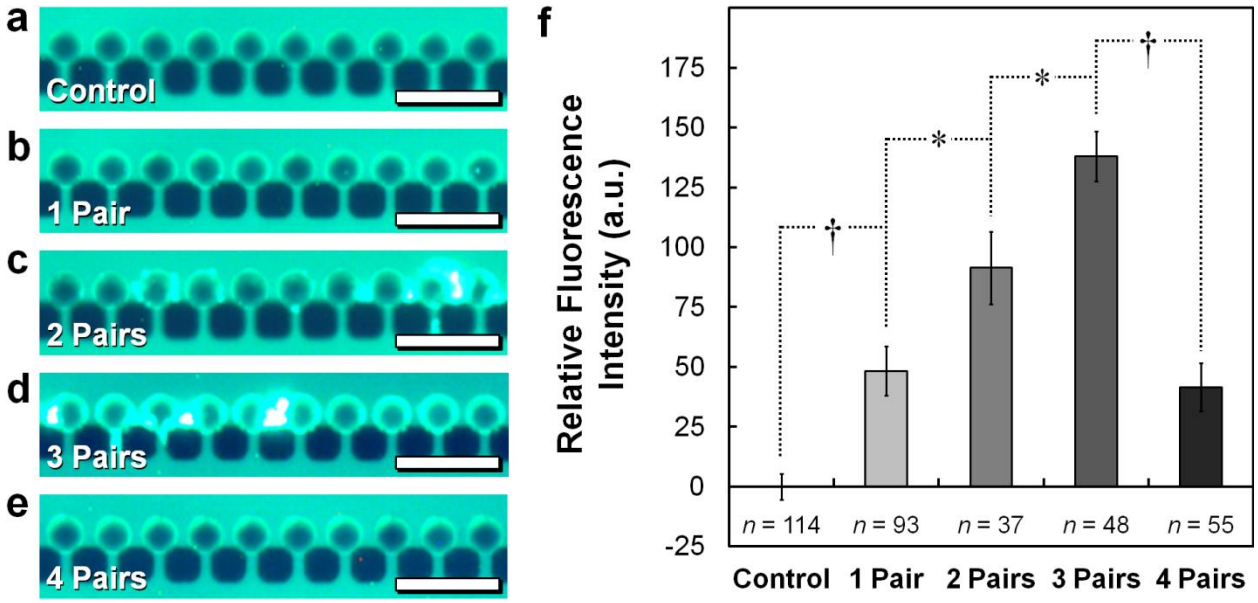

Figure 3.21 Experimental results for microbead fluorescence corresponding to microbeads with varying extended biological linker lengths. **(a-e)** Fluorescence micrographs of arrayed 15 μm diameter streptavidin-coated microbeads corresponding to: **(a)** zero biotin-avidin pairs, **(b)** one biotin-avidin pair, **(c)** two biotin-avidin pairs, **(d)** three biotin-avidin pairs, and **(e)** four biotin-avidin pairs. Scale Bars = 50 μm. **(f)** Average relative fluorescence intensities (*RFIs*) of arrayed microbeads after mixing with the FA solution. *RFI* values were quantified using **Equation 3.6**. Error Bars denote s.e.m.; * and † denote $p < 0.05$ and $p < 0.0001$ statistically significant differences, respectively.

coated-microbeads were simultaneously functionalized with one, two, three, or four biotin-avidin pairs in parallel. After fluidic mixing with the FA solution, each set of microbeads were immobilized in distinct μPAT arrays for fluorescence visualization and signal detection. For example, **Figure 3.21a-e** show fluorescence micrographs of arrayed 15 μm diameter streptavidin-coated microbeads corresponding to: **(a)** zero biotin-avidin pairs, **(b)** one biotin-avidin pair, **(c)** two biotin-avidin pairs, **(d)** three biotin-avidin pairs, and **(e)** four biotin-avidin pairs. Solution-phase FAs were found to produce background noise in all of the cases (**Fig. 3.21a-e**); however, fluorescence quantification was not prevented (**Fig. 3.21f**). Microbead *RFI* values were quantified using **Equation 3.6**. The quantified fluorescence results are shown in **Figure 3.21f**. The experimental results revealed that as the length of the extended biological linker increased up to three biotin-avidin pairs, the corresponding *RFI* increased as well. After mixing with the FA solution, microbeads with one biotin-avidin pair produced an average *RFI* of 48.3±10.3, which was significantly higher than the negative control microbeads ($p < 0.0001$). The addition of a second biotin-avidin pair resulted in an increase in microbead fluorescence ($p < 0.05$), with an average *RFI* of 91.4±15.2. The highest fluorescence intensities were observed for microbeads with three biotin-avidin pairs. Specifically, the average *RFI* for streptavidin-coated microbeads with three biotin-avidin pairs was 138.0±10.4, which was significantly higher than the two-pair case ($p < 0.05$) and the one-pair case ($p < 0.0001$). Conversely, the addition of a fourth biotin-avidin pair resulted in a significant decrease in microbead fluorescence ($p < 0.0001$). After mixing with the FA solution, streptavidin-coated

microbeads with four biotin-avidin pairs produced an average *RFI* of 41.5±10.1. Although this response was significantly higher compared to the control case ($p < 0.0005$), the fluorescence intensities for the four-pair case were not statistically discernable from the one-pair case ($p = 0.64$) (**Fig. 3.21f**). These results are in agreement with prior works that have reported that increasing the biological linker length beyond an optimal distance can result in a decrease in the fluorescence response.[123]

3.4.4.3 Cell Handling *via* μPAR

The capability of employing the μPAR technique to rail cells under continuous flow conditions was also investigated. Suspended BAECs were loaded into a μPAR system with $\alpha = 1°$. Experimental observations revealed that the μPAR system effectively transported suspended cells into adjacent flow streams of dyed solutions. For example, **Figure 3.22** shows sequential micrographs of suspended BAECs being railed from: **(a)** the cell media suspension to a blue-dyed solution, and **(b)** the blue-dyed solution to a yellow-dyed solution. These results demonstrate that the μPAR methodology could be integrated into dynamic cell-based microarrays to transport suspended cells into parallel flow streams of fluidic reagents and washes for cellular applications.

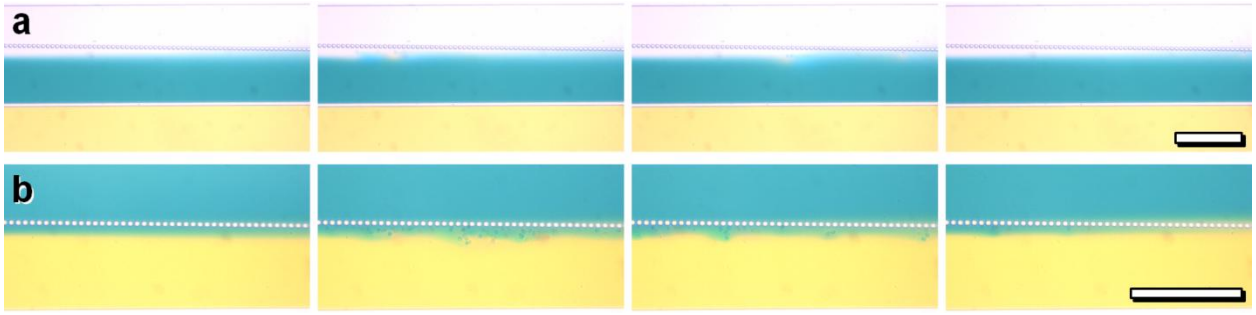

Figure 3.22 Experimental results for railing cells *via* μPAR. Sequential micrographs show BAECs transported from: **(a)** the cell media suspension to the blue-dyed solution, and **(b)** the blue-dyed solution to the yellow-dyed solution. Scale Bars = 300 μm

Chapter 4: Conclusions and Future Directions

4.1 Micropost Array Gradients for Cell Handling

Micropost array gradients provide an effective technique for engineering the biophysical properties of discrete, microscale substrate features *via* simple, accurate, and repeatable fabrication processes. Here, unidirectional micropost array gradients of variable micropost stiffness and variable interpost spacing were constructed to regulate cell motility *via* durotaxis and spatiotaxis stimuli, respectively.

4.1.1 Micropost Array Gradients for Inducing Cellular Durotaxis

Unidirectional micropost array stiffness gradients were employed to investigate cell motility in response to microtopographic mechanical cues. Two classes of micropost array durotaxis gradients were developed, corresponding to the use of circular or elliptical microposts. For the circular micropost array stiffness gradients, the radii (and therefore, stiffness) of arrayed microposts were increased in a single, designed direction. For the elliptical micropost array stiffness gradients, the major axes of arrayed microposts were increased in a single direction, while the minor axes were simultaneously decreased. BAECs seeded on both types of micropost array stiffness gradients exhibited higher displacements and speeds in the direction of increasing micropost stiffness *versus* opposite that direction. Additionally, higher gradient strength was found to enhance this directional response. Between the two types of micropost array stiffness gradients, the use of elliptical microposts offers a superior technique for applying durotactic stimuli to living cells. In particular, the anisotropy of elliptical microposts enables the application of dual-axis durotaxis cues to seeded cells. Experimental results for the elliptical micropost array stiffness gradients revealed that cell migration was not only promoted in the direction of increasing micropost stiffness, but also that cell movement perpendicular to that direction was reduced. These results suggest that the micropost array stiffness gradient methodology offers a unique and passive technique for regulating the motile processes of seeded cells *via* substrate-based mechanical cues.

4.1.2 Micropost Array Gradients for Inducing Cellular Spatiotaxis

Microtopographic techniques have previously been utilized to tune the mechanical properties of discrete substrate features for studying and directing cellular functions; however, the effects of changes in micropost spacing on cellular behavior have remained elusive. The spacing between circular microposts was gradually decreased from post-to-post over the lengths of micropost arrays. BAECs seeded on the micropost array spacing gradients exhibited higher displacements and speeds in the direction of decreasing interpost spacing *versus* opposite that direction. Higher gradient strength was found to enhance this directional response. This work represents the first explicit demonstration of unidirectional spatiotaxis, *i.e.*, the ability to regulate cell motility by varying the spacing of substrate binding sites in a single direction. Although further study is needed to elucidate the specific mechanisms underlying the spatiotaxis migratory response, the experimental results demonstrate that the spacing between microtopographic features represents a determinant factor in cell motility.

4.1.3 Micropost Array Gradients to Examine Cellular Durotaxis *versus* Spatiotaxis

A microfabricated post array with variable interpost spacing and micropost stiffness was employed to investigate the effects of microtopographic spatial stimuli on the mechanical response of living cells. Experimental results revealed that changes in micropost spacing can significantly limit the effects of mechanical substrate cues on cell motility. In response to post-to-post differences in interpost spacing of 40 nm (on average), seeded cells exhibited preferential migration opposite the direction of the mechanical stimuli. Thus, these results suggest that microtopographic spatial stimuli can be a determinant factor in directional migration. Additionally, the design of micropost spacing can be critical to the efficacy of cellular platforms for mechanobiological applications.

4.1.4 Future Directions for Micropost Array Gradients

The use of micro- and nanotopographic methods for investigating and controlling diverse cellular processes is expanding. Here, substrates were designed with post-to-post differences in stiffness of 0.5 nN/μm, 2 nN/μm, 3 nN/μm, and 7.5 nN/μm, and post-post differences in spacing of 10 nm, 20 nm, and 40 nm (on average). However, both the stiffness and spacing gradient strength of micropost arrays can be tailored corresponding to specific applications. Although the current studies employed unidirectional micropost array gradients in linear arrangements, individual microposts can be independently placed and geometrically tuned to achieve diverse configurations of substrate stiffness and interpost spacing (*e.g.*, radial gradients). Micropost array gradients could also be scaled up or down as desired. In particular, scaling the micropost array stiffness gradient methodology down to the nanoscale (*i.e.*, using nanoposts) would better mimic continuous rigidity gradients that include infinitesimally small stiffness steps. Because substrate rigidity and microtopography have been demonstrated to affect a variety of cells, the presented techniques could be adapted to examine how additional cell types respond to microtopographic stiffness and spacing gradients. Prior works have used micropost arrays to measure cellular forces on the substrate, which suggests that the presented substrates could be employed to elucidate the effects of biophysical gradients on the traction forces of motile cells. Additionally, micropost array gradients could be used to reveal how intracellular processes (*e.g.*, actin and focal adhesion dynamics) are affected by biophysical microtopographic stimuli. As a method for investigating the cellular response to substrate-based biophysical cues, micropost array gradients offer a simple, yet powerful technique for applying unidirectional biophysical stimuli to living cells. Thus, the presented methodologies could provide the foundation for new classes of passive, microtopographic substrates capable of controlling cellular motility *via* biophysical cues, particularly for cell handling applications in fields including biomaterials, tissue engineering, and regenerative medicine.

4.2 Micropost Array-Based Microfluidic Platforms for Microparticle Handling

Precision hydrodynamic controls of suspended cells are critical to the advancement of dynamic cell-based microarrays for lab-on-a-chip applications including quantitative cell biology, drug screening, and medical diagnostics. Here, novel micropost array-based methodologies (*i.e.*, μPAT and μPAR) were presented for handling both microbeads and cells in microfluidic systems. Due to the challenges associated with handling cells *versus* microbeads in microfluidic environments (*e.g.*, high polydispersity, independent mobility, increased substrate adhesivity, and experimental fragility), this work focused primarily on demonstrating and characterizing the presented techniques using microbeads. The potential of employing the μPAT and μPAR systems for cell handling applications was also investigated.

4.2.1 Trapping-and-Releasing Microbeads and Cells *via* Resettable μPAT

Hydrodynamic methods are ideally suited for transporting and arraying microparticles (*e.g.*, microbeads and cells) in microfluidic systems. The resettable μPAT technique was demonstrated as an effective single-layer resettable hydrodynamic arraying system by: (*i*) achieving high-density trapping of microparticles under positive fluidic flow, and (*ii*) releasing the microparticles after switching the flow polarity to reset the microarray. Experimental device runs with the resettable μPAT system for microbead handling revealed a *TE* of 99%, a *LE* of 99.8%, and a *RE* of 100%. Due to the increased trapping density of 100 microbeads (15 μm in diameter) in a 0.6 mm^2 area, higher numbers of data points (*i.e.*, immobilized microbeads) can be arrayed without sacrificing device area. Experimental device runs with suspended BAECs revealed that the resettable μPAT system can be employed for cell handling applications; however, there were several caveats. After trapping suspended cells in the designated array positions, a small proportion of cells were observed to migrate through the trapping sites. For releasing arrayed cells, solutions capable of enhancing cellular detachment from the substrate (*i.e.*, 0.5X Trypsin) were needed to achieve resettability.

4.2.2 Continuous Flow Railing of Microbeads and Cells *via* μPAR

The ability to rapidly mix suspended microparticles with discrete solutions of chemicals and bio-molecules is integral to diverse biological applications. Here, a μPAR system was developed for transporting suspended microparticles into sequential, parallel flow streams of reagents and fluidic washes. Experimental observations revealed that increasing the angle α above 1° decreased the railing efficiency, as microbead immobilization in the gaps between microposts was promoted. However, microposts arrayed at an angle of 1° from the flow direction served as a railing system by successfully preventing microbeads from immobilizing in the gaps between microposts. In addition to railing microbeads, the μPAR system was also successfully employed for transporting suspended BAECs into adjacent flow streams, which demonstrates the potential of using the μPAR technique for cellular applications. This work represents the first demonstration of microfluidic railing of either microbeads or cells into adjacent flow streams.

4.2.3 Microbead-Based Applications for the Microfluidic Platforms

Although one of the goals of this dissertation was to advance cell handling in microfluidic systems, the presented microfluidic platforms are not limited exclusively to cellular applications. Dynamic bead-based microarrays offer an ideal platform for chemical and biological assays; however, limitations associated with microparticle handling have hindered the efficacy of current bead-based systems. By enhancing microbead handling and enabling multi-stage fluidic reactions and analyses on the surface of microbeads, the microfluidic platforms presented in this work could provide powerful techniques for microbead handling in dynamic bead-based microarrays.

4.2.3.1 Dynamic Bead-Based Microarray with μPAT for Parallel DNA Detection

The integration of hydrodynamic microbead arraying techniques into dynamic microarrays offers a powerful and scalable technique for achieving low-cost detection of multiple bio-molecules in parallel. Here, a microfluidic bead-based platform was employed to simultaneously detect multiple ssDNA oligonucleotide sequences *via* MBs conjugated to polystyrene microbead substrates. Label-free solutions of PM, SNP, and MM DNA analytes were successfully differentiated in parallel with single base-pair mismatch specificity. Automated systems could be implemented to rapidly obtain fluorescence data from a single fluorescence image of μPAT-immobilized microbeads, serving as an effective alternative to more complex flow cytometry-based methods. Although the current system was employed to detect four homogenous solutions, the present methodology could be modified to dramatically increase parallelization by distributing the microbeads to thousands of channels – each tailored for distinct reactions. The MB used in this study was designed to detect single nucleotide differences in ssDNA oligonucleotide sequences; however, MBs can be used as a detection mechanism for diverse chemicals and bio-molecules. Thus, the dynamic bead-based microarray presented here could be adapted to achieve multiplexed detection for a wide range of biological applications, such as POC diagnostics, drug screening, and pathogen detection.

4.2.3.2 Multi-Stage Fluidic Reactions and Analyses Under Discontinuous Flow Conditions *via* MPP

Despite the capability of simultaneously detecting multiple ssDNA oligonucleotide sequences in parallel, the dynamic microarray with μPAT presented included several limitations, such as significant device area requirements and an inability to implement fluidic washes. In addition, all of the experimental reagents were mixed prior to bead-immobilization, resulting in undesired solution-phase binding, which increased background noise (and can potentially decrease assay sensitivity). To overcome these issues, the μPAT technique was utilized in a MPP system to achieve multi-stage fluidic reactions on microbeads under discontinuous flow conditions, thereby precluding chip-area requirements associated with laminar diffusion-based mixing. Fluidic washes of suspended microbeads were effectively implemented between reaction steps to limit undesired solution-phase binding of reagents. Additionally, the microbeads were immobilized after each reaction step to detect the fluorescence response for the same set of microbeads after every phase of the multi-stage process. Here, MPP was used to detect 100 pM concentrations of IFN-γ *via* a six-step aptamer-based sandwich assay; however,

the MPP technique can be adapted for diverse biological assays. These results suggest that the MPP methodology could provide a simple and effective platform to achieve multi-stage fluidic processes for a variety of chemical and biological applications.

4.2.3.3 Multi-Stage Fluidic Reactions Under Continuous Flow Conditions *via* μPAR

One disadvantage of the MPP system is that the methodology is inherently based on a non-continuous flow process, where each reagent or fluidic wash must be loaded sequentially and separately. Such discontinuous flow processes suffer from limitations associated with operational time and labor. The continuous flow process of the μPAR methodology bypasses these issues. As a demonstrative example, the μPAR technique was employed to achieve continuous flow LbL synthesis on streptavidin-coated polystyrene microbead substrates. Extended biological linkers consisting of one, two, three, and four biotin-avidin pairs were conjugated to streptavidin-coated microbeads in parallel *via* a LbL μPAR process. Thereafter, the microbeads were mixed with a fluorescently labeled analyte, resulting in detectable fluorescence intensities on the surfaces of the microbeads. At maximum, the reaction process for synthesizing an extended biological linker consisting of four biotin-avidin pairs onto a streptavidin-coated microbead included a total of 18 fluidic stages (including 8 wash steps). Experimental results revealed that microbead fluorescence was enhanced as the length of the extended biological linker increased up to three biotin-avidin pairs; however, the addition of a fourth biotin-avidin pair decreased the fluorescence response. These results suggest that the length of biological linkers can be optimized to maximize fluorescence intensities, which is consistent with prior studies.[123]

Although the continuous flow μPAR methodology provides advantages *versus* discontinuous flow processes, there remained several disadvantages for achieving multi-stage reactions and analyses compared to the MPP system. Specifically, the microbeads in the μPAR system were immobilized exclusively after reaction completion, thereby preventing microbead visualization and fluorescence detection over the course of the LbL process. This issue could be circumvented by varying the angle at which the microposts are arrayed with respect to the direction of the fluid flow (*e.g.*, from 1° to 2.5°) to immobilize a distinct number of microbeads within the μPAR system. Another issue is that the 1° angle between the arrayed microposts and the flow direction (*i.e.*, for ensuring successful railing) greatly increases the device area requirements of μPAR systems. Consequently, for cases where minimal device area is desired, the MPP methodology would present a superior technique compared to the μPAR system.

4.2.4 Future Directions for the Microfluidic Platforms for Microparticle Handling

In this dissertation, microposts were arrayed in microfluidic systems to achieve three fundamental accomplishments. First, a μPAT system was presented to facilitate the transport and immobilization of suspended cells and microbeads in designated array positions *via* a single-layer hydrodynamic technique. Secondly, microfluidic platforms were developed to mix suspended particles with multiple, discrete fluidic reagents and washes to perform multi-stage fluidic processes under discontinuous and continuous flow conditions *via* the MPP and μPAR methodologies, respectively. These systems could be particularly beneficial for surface-based biochemical assays, where the ability to rapidly synthesize multiple bio-molecules and chemicals

onto microbead substrates is desired. Lastly, the μPAT system was also demonstrated for releasing previously immobilized cells and microbeads from trapping positions to enable microarray resettability. The resettable μPAT technique could be used to rapidly retrieve high numbers of microparticles for analysis following microfluidic particulate-based assays. Additionally, the ability to reset microarrays could greatly reduce the costs, time, and labor associated with fabricating one-time-use devices.

The presented μPAT and μPAR systems were designed with microparticles and microposts that were approximately the same size. Thus, these techniques could be scaled up or down as desired (*i.e.*, to handle particles of various sizes). For example, the μPAT and μPAR systems could be tailored to handle a variety of cells types. Future work should investigate the potential to handling bacteria using the presented methodologies. To benefit from the advantages of nanoparticles, the presented platforms could also be scaled down to use arrayed nanoposts for handling nanoparticles in fluidic systems.

In this work, the microfluidic systems were primarily characterized using suspended microbeads first instead of cells (which represent a significantly higher degree of experimental complexity). Experimental testing with microbeads before cells is highly consistent with prior efforts of developing dynamic microarrays for cellular applications.[37, 39, 81, 91-93] The bead-based experimental results provide a fundamental basis for subsequent studies with living cells. Similar to prior dynamic particulate-based systems, future work should concentrate on adapting the presented platforms to achieve high control of suspended cells in microfluidic systems. At present, both the bead-based and cell-based experimental results represent significant progress toward robust microfluidic handling of suspended microparticles. Thus, the novel microfluidic particulate-based platforms in this dissertation could impact a broad range of chemical and biological fields, including quantitative cell biology, genomics, proteomics, drug discovery, and molecular diagnostics.

References

1. Di Carlo, D. & Lee, L. P. Dynamic single-cell analysis for quantitative biology. Analytical Chemistry 78, 7918-7925 (2006).
2. Gurtner, G. C., Werner, S., Barrandon, Y. & Longaker, M. T. Wound repair and regeneration. Nature 453, 314-321 (2008).
3. Petrie, R. J., Doyle, A. D. & Yamada, K. M. Random versus directionally persistent cell migration. Nature Reviews Molecular Cell Biology 10, 538-549 (2009).
4. Gray, D. S., Tien, J. & Chen, C. S. Repositioning of cells by mechanotaxis on surfaces with micropatterned Young's modulus. Journal of Biomedical Materials Research Part A 66A, 605-614 (2003).
5. Hong, J. et al. in Nano/Micro Engineered and Molecular Systems 797-800 (2007).
6. Kidoaki, A. & Matsuda, T. Microelastic gradient gelatinous gels to induce cellular mechanotaxis. Journal of Biotechnology 133, 225-230 (2008).
7. Burdick, J. A., Khademhosseini, A. & Langer, R. Fabrication of gradient hydrogels using a microfluidics/photopolymerization process. Langmuir 20, 5153-5156 (2004).
8. Hadjipanayi, E., Mudera, V. & Brown, R. A. Guiding Cell Migration in 3D: A Collagen Matrix with Graded Directional Stiffness. Cell Motility and the Cytoskeleton 66, 121-128 (2009).
9. Isenberg, B. C., DiMilla, P. A., Walker, M., Kim, S. & Wong, J. Y. Vascular Smooth Muscle Cell Durotaxis Depends on Substrate Stiffness Gradient Strength. Biophysical Journal 97, 1313-1322 (2009).
10. Wong, J. Y., Velasco, A., Rajagopalan, P. & Pham, Q. Directed movement of vascular smooth muscle cells on gradient-compliant hydrogels. Langmuir 19, 1908-1913 (2003).
11. Zaari, N., Rajagopalan, P., Kim, S. K., Engler, A. J. & Wong, J. Y. Photopolymerization in microfluidic gradient generators: Microscale control of substrate compliance to manipulate cell response. Advanced Materials 16, 2133-2137 (2004).
12. Chicurel, M. E., Chen, C. S. & Ingber, D. E. Cellular control lies in the balance of forces. Current Opinion In Cell Biology 10, 232-239 (1998).
13. Cho, M. R., Thatte, H. S., Lee, R. C. & Golan, D. E. Integrin-dependent human macrophage migration induced by oscillatory electrical stimulation. Annals Of Biomedical Engineering 28, 234-243 (2000).
14. Choquet, D., Felsenfeld, D. P. & Sheetz, M. P. Extracellular matrix rigidity causes strengthening of integrin-cytoskeleton linkages. Cell 88, 39-48 (1997).
15. Farboud, B., Nuccitelli, R., Schwab, I. R. & Isseroff, R. R. DC electric fields induce rapid directional migration in cultured human corneal epithelial cells. Experimental Eye Research 70, 667-673 (2000).
16. Jiang, X. Y., Bruzewicz, D. A., Wong, A. P., Piel, M. & Whitesides, G. M. Directing cell migration with asymmetric micropatterns. Proceedings Of The National Academy Of Sciences Of The United States Of America 102, 975-978 (2005).
17. Parker, K. K. et al. Directional control of lamellipodia extension by constraining cell shape and orienting cell tractional forces. Faseb Journal 16 (2002).
18. Pelham, R. J. & Wang, Y. L. Cell locomotion and focal adhesions are regulated by the mechanical properties of the substrate. Biological Bulletin 194, 348-349 (1998).

19. Singh, M., Berkland, C. & Detamore, M. S. Strategies and Applications for Incorporating Physical and Chemical Signal Gradients in Tissue Engineering. Tissue Engineering Part B-Reviews 14, 341-366 (2008).
20. Wang, E., Zhao, M., Forrester, J. V. & McCaig, C. D. Re-orientation and faster, directed migration of lens epithelial cells in a physiological electric field. Experimental Eye Research 71, 91-98 (2000).
21. Brahmbhatt, A. A. & Klemke, R. L. ERK and RhoA differentially regulate pseudopodia growth and retraction during chemotaxis. Journal of Biological Chemistry 278, 13016-13025 (2003).
22. Harms, B. D., Bassi, G. M., Horwitz, A. R. & Lauffenburger, D. A. Directional persistence of EGF-Induced cell migration is associated with stabilization of lamellipodial protrusions. Biophysical Journal 88, 1479-1488 (2005).
23. Zhelev, D. V., Alteraifi, A. M. & Chodniewicz, D. Controlled pseudopod extension of human neutrophils stimulated with different chemoattractants. Biophysical Journal 87, 688-695 (2004).
24. Kloxin, A. M., Kasko, A. M., Salinas, C. N. & Anseth, K. S. Photodegradable Hydrogels for Dynamic Tuning of Physical and Chemical Properties. Science 324, 59-63 (2009).
25. Brunette, D. M., Kenner, G. S. & Gould, T. R. L. Grooved Titanium Surfaces Orient Growth and Migration of Cells from Human Gingival Explants. Journal of Dental Research 62, 1045-1048 (1983).
26. Curtis, A. & Wilkinson, C. Topographical control of cells. Biomaterials 18, 1573-1583 (1997).
27. Dalton, B. A. et al. Modulation of epithelial tissue and cell migration by microgrooves. Journal of Biomedical Materials Research 56, 195-207 (2001).
28. Kaiser, J. P., Reinmann, A. & Bruinink, A. The effect of topographic characteristics on cell migration velocity. Biomaterials 27, 5230-5241 (2006).
29. Walboomers, X. F., Croes, H. J. E., Ginsel, L. A. & Jansen, J. A. Contact guidance of rat fibroblasts on various implant materials. Journal of Biomedical Materials Research 47, 204-212 (1999).
30. Park, J. Y. et al. Single cell trapping in larger microwells capable of supporting cell spreading and proliferation. Microfluidics and Nanofluidics 8, 263-268 (2010).
31. Park, M. C., Hur, J. Y., Cho, H. S., Park, S. H. & Suh, K. Y. High-throughput single-cell quantification using simple microwell-based cell docking and programmable time-course live-cell imaging. Lab on a Chip 11, 79-86 (2011).
32. Rettig, J. R. & Folch, A. Large-scale single-cell trapping and imaging using microwell arrays. Analytical Chemistry 77, 5628-5634 (2005).
33. Yamamura, S. et al. Single-cell microarray for analyzing cellular response. Analytical Chemistry 77, 8050-8056 (2005).
34. Di Carlo, D., Aghdam, N. & Lee, L. P. Single-cell enzyme concentrations, kinetics, and inhibition analysis using high-density hydrodynamic cell isolation arrays. Analytical Chemistry 78, 4925-4930 (2006).
35. Di Carlo, D., Wu, L. Y. & Lee, L. P. Dynamic single cell culture array. Lab on a Chip 6, 1445-1449 (2006).
36. Skelley, A. M., Kirak, O., Suh, H., Jaenisch, R. & Voldman, J. Microfluidic control of cell pairing and fusion. Nature Methods 6, 147-152 (2009).

37. Tan, W. H. & Takeuchi, S. Dynamic microarray system with gentle retrieval mechanism for cell-encapsulating hydrogel beads. Lab on a Chip 8, 259-266 (2008).
38. Tanyeri, M., Johnson-Chavarria, E. M. & Schroeder, C. M. Hydrodynamic trap for single particles and cells. Applied Physics Letters 96 (2010).
39. Teshima, T., Onoe, H., Kuribayashi-Shigetomi, K. & Takeuchi, S. in The 24nd IEEE International Conference on Micro Electro Mechanical Systems (MEMS 2011) 71-74 (Cancun, Mexico, 2011).
40. Faley, S. et al. Microfluidic platform for real-time signaling analysis of multiple single T cells in parallel. Lab on a Chip 8, 1700-1712 (2008).
41. Faley, S. L. et al. Microfluidic single cell arrays to interrogate signalling dynamics of individual, patient-derived hematopoietic stem cells. Lab on a Chip 9, 2659-2664 (2009).
42. Iwai, K., Tan, W.-H., Ishihara, H. & Takeuchi, S. A resettable dynamic microarray device. Biomedical Microdevices (2011).
43. Fu, Z. et al. Microfabricated Renewable Beads-Trapping/Releasing Flow Cell for Rapid Antigenâ^'Antibody Reaction in Chemiluminescent Immunoassay. Analytical Chemistry 83, 2685-2690 (2011).
44. Chan, C. E. & Odde, D. J. Traction Dynamics of Filopodia on Compliant Substrates. Science 322, 1687-1691 (2008).
45. Trepat, X. et al. Physical forces during collective cell migration. Nature Physics 5, 426-430 (2009).
46. Mahmud, G. et al. Directing cell motions on micropatterned ratchets. Nature Physics 5, 606-612 (2009).
47. Xia, N. et al. Directional control of cell motility through focal adhesion positioning and spatial control of Rac activation. Faseb Journal 22, 1649-1659 (2008).
48. Heit, B., Tavener, S., Raharjo, E. & Kubes, P. An intracellular signaling hierarchy determines direction of migration in opposing chemotactic gradients. Journal Of Cell Biology 159, 91-102 (2002).
49. Lo, C.-M., Wang, H.-B., Dembo, M. & Wang, Y.-L. Cell Movement Is Guided by the Rigidity of the Substrate. Biophysical Journal 79, 144-152 (2000).
50. Thakar, R. G. et al. Contractility-dependent modulation of cell proliferation and adhesion by microscale topographical cues. Small 4, 1416-1424 (2008).
51. Akhouayri, O. et al. Mechanical strain early increases integrin-mediated focal adhesion and tyrosine phosphorylation in osteoblast-like cells. Journal Of Bone And Mineral Research 14, S471-S471 (1999).
52. Bischofs, I. B. & Schwarz, U. S. Cell organization in soft media due to active mechanosensing. Proceedings Of The National Academy Of Sciences Of The United States Of America 100, 9274-9279 (2003).
53. Schwartz, Wang & Bruinsma. Cell locomotion and focal adhesions are regulated by the mechanical properties of the substrate - Discussion. Biological Bulletin 194, 349-350 (1998).
54. Butler, J. P., Tolic-Norrelykke, I. M., Fabry, B. & Fredberg, J. J. Traction fields, moments, and strain energy that cells exert on their surroundings. American Journal Of Physiology-Cell Physiology 282, C595-C605 (2002).
55. Kong, H. J., Polte, T. R., Alsberg, E. & Mooney, D. J. FRET measurements of cell-traction forces and nano-scale clustering of adhesion ligands varied by substrate stiffness.

Proceedings Of The National Academy Of Sciences Of The United States Of America 102, 4300-4305 (2005).
56. Schwarz, U. S. et al. Calculation of forces at focal adhesions from elastic substrate data: The effect of localized force and the need for regularization. Biophysical Journal 83, 1380-1394 (2002).
57. Gallant, N. D. & Garcia, A. J. Cell adhesion strengthening and focal adhesion assembly on micropatterned substrates. Molecular Biology Of The Cell 15, 173A-173A (2004).
58. Mack, P. J., Kaazempur-Mofrad, M. R., Karcher, H., Lee, R. T. & Kamm, R. D. Force-induced focal adhesion translocation: effects of force amplitude and frequency. American Journal Of Physiology-Cell Physiology 287, C954-C962 (2004).
59. Ando, J., Nomura, H. & Kamiya, A. The Effect of Fluid Shear-Stress on the Migration and Proliferation of Cultured Endothelial-Cells. Microvascular Research 33, 62-70 (1987).
60. Hsu, S., Thakar, R., Liepmann, D. & Li, S. Effects of shear stress on endothelial cell haptotaxis on micropatterned surfaces. Biochemical and Biophysical Research Communications 337, 401-409 (2005).
61. Soghomonians, A., Barakat, A. I., Thirkill, T. L., Blankenship, T. N. & Douglas, G. C. Effect of shear stress on migration and integrin expression in macaque trophoblast cells. Biochimica Et Biophysica Acta-Molecular Cell Research 1589, 233-246 (2002).
62. Verkhovsky, A. B., Svitkina, T. M. & Borisy, G. G. Self-polarization and directional motility of cytoplasm. Current Biology 9, 11-20 (1999).
63. Galbraith, C. G., Yamada, K. M. & Sheetz, M. P. The relationship between force and focal complex development. Journal Of Cell Biology 159, 695-705 (2002).
64. Engler, A. J., Sen, S., Sweeney, H. L. & Discher, D. E. Matrix elasticity directs stem cell lineage specification. Cell 126, 677-689 (2006).
65. Fu, J. P. et al. Mechanical regulation of cell function with geometrically modulated elastomeric substrates. Nature Methods 7, 733-795 (2010).
66. Saez, A., Ghibaudo, M., Buguin, A., Silberzan, P. & Ladoux, B. Rigidity-driven growth and migration of epithelial cells on microstructured anisotropic substrates. Proceedings of the National Academy of Sciences of the United States of America 104, 8281-8286 (2007).
67. Sniadecki, N. J. & Chen, C. S. in Methods in Cell Biology - Cell Mechanics 313-328 (2007).
68. Tan, J. L. et al. Cells lying on a bed of microneedles: An approach to isolate mechanical force. Proceedings of the National Academy of Sciences of the United States of America 100, 1484-1489 (2003).
69. Uttayarat, P. et al. Microtopography and flow modulate the direction of endothelial cell migration. American Journal of Physiology-Heart and Circulatory Physiology 294, H1027-H1035 (2008).
70. Kim, D. H. et al. Guided Cell Migration on Microtextured Substrates with Variable Local Density and Anisotropy. Advanced Functional Materials 19, 1579-1586 (2009).
71. Kim, D.-H. et al. Mechanosensitivity of fibroblast cell shape and movement to anisotropic substratum topography gradients. Biomaterials 30, 5433-5444 (2009).
72. Sniadecki, N. J. & Chen, C. S. in Cell Mechanics 313-+ (2007).

73. Li, B. et al. Development of micropost force sensor array with culture experiments for determination of cell traction forces. Cell Motility and the Cytoskeleton 64, 509-518 (2007).
74. Lin, I. K. et al. Viscoelastic mechanical behavior of soft microcantilever-based force sensors. Applied Physics Letters 93, 251907-251907-3 (2008).
75. Ghibaudo, M. et al. Traction forces and rigidity sensing regulate cell functions. Soft Matter 4, 1836-1843 (2008).
76. Carmona-Fontaine, C. et al. Contact inhibition of locomotion in vivo controls neural crest directional migration. Nature 456, 957-961 (2008).
77. Chodniewicz, D. & Klemke, R. L. Guiding cell migration through directed extension and stabilization of pseudopodia. Experimental Cell Research 301, 31-37 (2004).
78. Heath, J. & Holifield, B. Cell Locomotion - Actin Alone In Lamellipodia. Nature 352, 107-108 (1991).
79. Khoury, M. et al. A microfluidic traps system supporting prolonged culture of human embryonic stem cells aggregates. Biomedical Microdevices 12, 1001-1008 (2010).
80. Dittrich, P. S. & Manz, A. Lab-on-a-chip: microfluidics in drug discovery. Nature Reviews Drug Discovery 5, 210-218 (2006).
81. Tan, W. H. & Takeuchi, S. A trap-and-release integrated microfluidic system for dynamic microarray applications. Proceedings of the National Academy of Sciences of the United States of America 104, 1146-1151 (2007).
82. Verpoorte, E. Beads and chips: new recipes for analysis. Lab on a Chip 3, 60N-68N (2003).
83. Lim, C. T. & Zhang, Y. Bead-based microfluidic immunoassays: The next generation. Biosensors & Bioelectronics 22, 1197-1204 (2007).
84. Nilsson, J., Evander, M., Hammarstrom, B. & Laurell, T. Review of cell and particle trapping in microfluidic systems. Analytica Chimica Acta 649, 141-157 (2009).
85. Wheeler, A. R. et al. Microfluidic device for single-cell analysis. Analytical Chemistry 75, 3581-3586 (2003).
86. Du, J. Y. et al. Bead-based profiling of tyrosine kinase phosphorylation identifies SRC as a potential target for glioblastoma therapy. Nature Biotechnology 27, 77-83 (2009).
87. Horejsh, D. et al. A molecular beacon, bead-based assay for the detection of nucleic acids by flow cytometry. Nucleic Acids Research 33 (2005).
88. Ng, J. K. K. & Liu, W. T. Miniaturized platforms for the detection of single-nucleotide polymorphisms. Analytical and Bioanalytical Chemistry 386, 427-434 (2006).
89. Qiu, X. B. et al. Finger-actuated, self-contained immunoassay cassettes. Biomedical Microdevices 11, 1175-1186 (2009).
90. Thompson, J. A., Du, X. G., Grogan, J. M., Schrlau, M. G. & Bau, H. H. Polymeric microbead arrays for microfluidic applications. Journal of Micromechanics and Microengineering 20 (2010).
91. Kobel, S., Valero, A., Latt, J., Renaud, P. & Lutolf, M. Optimization of microfluidic single cell trapping for long-term on-chip culture. Lab on a Chip 10, 857-863 (2010).
92. Teshima, T., Ishihara, H., Iwai, K., Adachi, A. & Takeuchi, S. A dynamic microarray device for paired bead-based analysis. Lab on a Chip 10, 2443-2448 (2010).
93. Frimat, J. P. et al. A microfluidic array with cellular valving for single cell co-culture. Lab on a Chip 11, 231-237 (2011).

94. Dunbar, S. A. Applications of Luminex (R) xMAP (TM) technology for rapid, high-throughput multiplexed nucleic acid detection. Clinica Chimica Acta 363, 71-82 (2006).
95. Ali, M. F. et al. DNA hybridization and discrimination of single-nucleotide mismatches using chip-based microbead arrays. Analytical Chemistry 75, 4732-4739 (2003).
96. Hashmi, G. et al. A flexible array format for large-scale, rapid blood group DNA typing. Transfusion 45, 680-688 (2005).
97. Ng, J. K., Feng, H. H. & Liu, W. T. Rapid discrimination of single-nucleotide mismatches using a microfluidic device with monolayered beads. Analytica Chimica Acta 582, 295-303 (2007).
98. Steemers, F. J. & Gunderson, K. L. Whole genome genotyping technologies on the BeadArray (TM) platform. Biotechnology Journal 2, 41-49 (2007).
99. Thompson, J. A. & Bau, H. H. Microfluidic, bead-based assay: Theory and experiments. Journal of Chromatography B-Analytical Technologies in the Biomedical and Life Sciences 878, 228-236 (2010).
100. Hur, S. C., Tse, H. T. K. & Di Carlo, D. Sheathless inertial cell ordering for extreme throughput flow cytometry. Lab on a Chip 10, 274-280 (2010).
101. Kim, D. N., Lee, Y. & Koh, W. G. Fabrication of microfluidic devices incorporating bead-based reaction and microarray-based detection system for enzymatic assay. Sensors and Actuators B-Chemical 137, 305-312 (2009).
102. Iwai, K. & Takeuchi, S. in The 22nd IEEE International Conference on Micro Electro Mechanical Systems (MEMS 2009) 371-374 (Sorrento, Italy, 2009).
103. Lindstrom, S. & Andersson-Svahn, H. Overview of single-cell analyses: microdevices and applications. Lab on a Chip 10, 3363-3372 (2010).
104. Syvanen, A. C. Accessing genetic variation: Genotyping single nucleotide polymorphisms. Nature Reviews Genetics 2, 930-942 (2001).
105. Nagai, H., Narita, Y., Ohtaki, M., Saito, K. & Wakida, S. I. Single-bead analysis on a disk-shaped microfluidic device using an antigen-immobilized bead. Analytical Sciences 23, 975-979 (2007).
106. Tuleuova, N. et al. Development of an Aptamer Beacon for Detection of Interferon-Gamma. Analytical Chemistry 82, 1851-1857 (2010).
107. Hsieh, A. T. H., Pan, P. J. H. & Lee, A. P. Rapid label-free DNA analysis in picoliter microfluidic droplets using FRET probes. Microfluidics and Nanofluidics 6, 391-401 (2009).
108. Strohsahl, C. M., Miller, B. L. & Krauss, T. D. Preparation and use of metal surface-immobilized DNA hairpins for the detection of oligonucleotides. Nature Protocols 2, 2105-2110 (2007).
109. Kim, S. et al. Rapid DNA hybridization analysis using a PDMS microfluidic sensor and a molecular beacon. Analytical Sciences 23, 401-405 (2007).
110. Jung, J. et al. Fast and sensitive DNA analysis using changes in the FRET signals of molecular beacons in a PDMS microfluidic channel. Analytical and Bioanalytical Chemistry 387, 2609-2615 (2007).
111. Tan, L. et al. Molecular beacons for bioanalytical applications. Analyst 130, 1002-1005 (2005).
112. Yang, J. H. et al. Real-time RT-PCR for quantitation of hepatitis C virus RNA. Journal of Virological Methods 102, 119-128 (2002).

113. Zuo, X. B., Yang, X. H., Wang, K. M., Tan, W. H. & Wen, J. H. A novel sandwich assay with molecular beacon as report probe for nucleic acids detection on one-dimensional microfluidic beads array. Analytica Chimica Acta 587, 9-13 (2007).
114. Ng, J. K., Selamat, E. S. & Lin, W. T. A spatially addressable bead-based biosensor for simple and rapid DNA detection. Biosensors & Bioelectronics 23, 803-810 (2008).
115. Chung, S. E., Lee, S. A., Kim, J. & Kwon, S. Optofluidic encapsulation and manipulation of silicon microchips using image processing based optofluidic maskless lithography and railed microfluidics. Lab on a Chip 9, 2845-2850 (2009).
116. Park, W., Lee, H., Park, H. & Kwon, S. Sorting directionally oriented microstructures using railed microfluidics. Lab on a Chip 9, 2169-2175 (2009).
117. Lee, S. H. et al. Active Guidance of 3D Microstructures. Small 6, 2668-2672 (2010).
118. Abbyad, P., Dangla, R., Alexandrou, A. & Baroud, C. N. Rails and anchors: guiding and trapping droplet microreactors in two dimensions. Lab on a Chip 11, 813-821 (2011).
119. Kantak, C., Beyer, S., Yobas, L., Bansal, T. & Trau, D. A 'microfluidic pinball' for on-chip generation of Layer-by-Layer polyelectrolyte microcapsules. Lab on a Chip 11, 1030-1035 (2011).
120. Zhang, S., Yobas, L. & Trau, D. in The 12th International Conference on Miniaturized Systems for Chemistry and Life Sciences (MicroTAS 2008) 1402-1404 (San Diego, CA, USA, 2008).
121. Sochol, R. D. et al. in The IEEE 22nd International Conference on Micro Electro Mechanical Systems (MEMS 2009) 304-307 (Sorrento, Italy, 2009).
122. Shimozono, S. & Miyawaki, A. Engineering FRET constructs using CFP and YFP. Fluorescent Proteins, Second Edition 85, 381-+ (2008).
123. Yao, G. & Tan, W. H. Molecular-beacon-based array for sensitive DNA analysis. Analytical Biochemistry 331, 216-223 (2004).
124. Zhu, Z. R., Chao, J., Yu, H. & Waggoner, A. S. Directly labeled DNA probes using fluorescent nucleotides with different length linkers. Nucleic Acids Research 22, 3418-3422 (1994).
125. Kwon, B. H. et al. Binding Modes of New Bis-Ru(II) Complexes to DNA: Effect of the Length of the Linker. Bulletin of the Korean Chemical Society 31, 1615-1620 (2010).